National Technical University of Athens
School of Mechanical Engineering
Fluids Department
Parallel CFD & Optimization Unit

Contribution to the CFD modeling of Rotating Wheels and Treaded Tires in Passenger Cars

Diploma Thesis

Georgios Smyrlis

Industrial Supervisor:
Antoine Delacroix,
Manager TME

Supervisor:
Kyriakos C. Giannakoglou,
Professor NTUA

Athens, 2021

Acknowledgements

First and foremost, I would like to express my gratitude to my professor, Kyriakos C. Giannakoglou, for giving me the opportunity to work on such an interesting topic, in a professional and demanding environment, for the duration of my internship in Toyota Motor Europe. His continuous guidance, trust and support, have been key to the completion of this thesis.

Also, I would like to thank my manager, Antoine Delacroix, for the continuous trust and support throughout the whole duration of my internship in the premises of Toyota Motor Europe. His guidance and work ethic, have helped me expand my skills on a professional level and experience first hand the needs of working in such a demanding and high-stakes environment.

Furthermore, I would like to express my deep gratitude to my mentor and colleague, Panagiotis Koutsantonis. His constant support has provided me with the opportunity to develop my skills as an engineer, and his daily feedback has been a determining factor for the completion of my work in Toyota Motor Europe. Also I would like to thank my colleague, Pablo Fernandez, for being eager to help me when needed and sharing his knowledge with me.

I would also like to thank Dr. E. M. Papoutsis-Kiachagias, member of the Parallel CFD & Optimization Unit of NTUA, for his constant advice when needed. I acknowledge the time and effort he spent on assisting me on various occasions.

Last but not least I would like to thank my family, my mother Fotini, my father Christoforos and my sister Katerina, for their constant support throughout the duration of my internship.

National Technical University of Athens
School of Mechanical Engineering
Fluids Department
Parallel CFD & Optimization Unit

Contribution to the CFD modeling of Rotating Wheels and Treaded Tires in Passenger Cars

Diploma Thesis
Georgios Smyrlis

Industrial Supervisor: Antoine Delacroix, Manager TME

Supervisor: Kyriakos C. Giannakoglou, Professor NTUA

Athens, 2021

Abstract

This diploma thesis aims at the development of a new strategy for the mesh generation process for the Sliding Mesh technique, used in the CFD simulation of passenger cars, in order to correctly simulate the rotation of the wheels. The proposed workflow focuses on increasing the robustness of the mesh generation process, and reducing the simulation cost of the Sliding Mesh simulation method. In this kind of applications *OpenFOAM*© environment is used in order to simulate the flow around the car.

A mesh generated by the new technique is assessed by comparing the results with the Tangential Velocity approach, which is the less demanding, yet less accurate method of simulating the rotation of the wheels. The accuracy of the Sliding Mesh and Tangential Velocity methods, when it comes to predicting the aerodynamic resistance of the car, is examined by comparing the simulation results to the Wind Tunnel data acquired for the same car setup. Finally, the gains in simulation cost from the new meshing process are discussed. Furthermore, limitations towards the reduction in the simulation cost of the Sliding Mesh method, are presented.

This work also includes a preliminary investigation in the impact of the treads (the pattern responsible for the performance of tires in rainy conditions) in the aerodynamic performance of a car. For this purpose, a single wheel model is used for the CFD simulations in the *OpenFOAM*© environment. The method of including the treads in the generated mesh is developed, and the correct method for simulating the rotation of the treaded tire is presented. Finally, a treaded tire is compared to

one without the tread pattern, through the results of the simulations conducted for both. The aerodynamic performance of each tire and the simulation cost of each approach are compared.

Most of this work was conducted in the premises of Toyota Motor Europe (TME) in Zaventem, Belgium, during a six-month internship under the supervision of industrial manager Mr. Antoine Delacroix.

Acronyms

AMI	Arbitrary Mesh Interface
BC	Boundary Condition
CAD	Computer Aided Design
CAE	Computer Aided Engineering
CFD	Computational Fluid Dynamics
DDES	Delayed Detached Eddy Simulation
DES	Detatched Eddy Simulation
LES	Large Eddy Simulation
MRF	Multiple Reference Frame
N-S	Navier - Stokes
NTUA	National Technical University of Athens
OpenFOAM	Open Field Operation And Manipulation
PCOpt	Parallel CFD & Optimization Unit of NTUA
PDE	Partial Differential Equation
RANS	Reynolds-Averaged Navier Stokes
RWBC	Rotating Wall Boundary Condition
SM	Sliding Mesh
TME	Toyota Motor Europe
TV	Tangential Velocity
WLTP	Worldwide Harmonized Vehicle Test Procedure
WT	Wind Tunnel
w.r.t.	with respect to

Contents

Chapter 1

Introduction

1.1 Car Aerodynamics and CO_2 Emissions

Over the last decades, the automotive industry has been putting increasing efforts on developing new models with focus on lowering emissions and fuel consumption. Electric and Hybrid Technology vehicles increasing popularity, has proven that the market exists for zero or low-emission mobility solutions. The restrictions over fuel consumption and CO_2 emissions proposed by the EU have accelerated the process by pressuring automotive industries to lower their model's environmental impact. The new Worldwide Harmonized Vehicle Test Procedure (WLTP) [1] standard, in action since 1 September 2017, increases the complexity for car manufacturers and dealerships, since every variation in a given car model has to be verified for its CO_2 emissions. This increases the need for a robust and viable way to test every variation of a given or under-development car model.

In order to comply with the new regulations, immense work has to be put into developing designs that are not only aerodynamically efficient, but also aesthetically pleasing. During the vehicle development phase, a lot of variations in the car model have to be evaluated based on their aerodynamic performance. Therefore, reliable and low-cost CFD solutions have found their way into the vehicle-development workflow of most automotive industries, as an alternative to the accurate, but costly Wind Tunnel (WT) experiments. Although CFD solutions have been a tool for automotive industries for a long time, low-cost and higher-accuracy solutions are being continuously considered.

This work focuses on the CFD simulation of a passenger car, targeting the accurate simulation of the rotating wheels with the minimum possible CPU cost.

1.2 Aerodynamic Resistance of a Car

During the vehicle development process, one of the high-priority points taken into account is the aerodynamic drag of the vehicle. The aerodynamic drag is the force that is exerted on the sum of the surfaces of the vehicle, as it is trying to move through the air with a given speed, projected on the direction of the car's velocity. Low values of this force, result in low fuel consumption, low emissions for an internal combustion (IC) car, whereas in the case of an electric vehicle (EV) this force is responsible for the reduction of the vehicle's range. Therefore, during the development process, efforts focus on decreasing the value of the aerodynamic drag to acceptable, usually predetermined, levels. For a given geometry, the correct approximation of this force is of essential value to the engineer. CFD solutions, often backed by WT data, can not only give a correct approximation of a car's aerodynamic drag, but certain methods exist that can guide the engineer to the geometry changes that result in a drag reduction.

The aerodynamic drag is often presented in a dimensionless manner, through the drag coefficient (C_d),

$$C_d = \frac{D}{q_\infty A} \tag{1.1}$$

where D is the drag force, $q_\infty = \frac{1}{2}\rho U_\infty^2$ is the dynamic pressure, U_∞ is the freestream velocity relative to the car and A is the frontal area of the vehicle, which is equal to the projection of the car's surface on a plane that is normal to the velocity vector.

The total aerodynamic drag can be considered as the sum of two quantities. The first quantity describes the forces exerted on the surface as a result of the friction between the air molecules and the car's surface due to their relative motion. This term often referred to as friction drag, depends both on the properties of the fluid, such as the fluid viscosity, and the properties of the surface, such its roughness. This force is tangent to the given surface. The second quantity describes the forces exerted on the surface as a result of the pressure distribution around the the car's geometry. This force is normal to the given surface and is often referred to as the pressure drag. The projected sum of the two terms is the calculated drag coefficient,

$$C_d = \frac{1}{q_\infty A} \int_{S_w} \left[\underbrace{p\hat{n}}_{\text{Pressure}} + \underbrace{\tau_w \hat{t}}_{\text{Friction}} \right] \cdot \hat{i}\, dS \tag{1.2}$$

where p is the pressure, τ_w is the shear wall stress, $\hat{n}$ and $\hat{t}$ are the normal and tangent to the surface unit vectors respectively, $\hat{i}$ is the unit vector on which the force is projected, parallel to the relative velocity direction and S_w is the wall surface on which forces are calculated.

The total aerodynamic resistance of the car is the sum of the forces exerted on every wet surface of the car. Wet surface is considered every surface that comes in contact with the air. The car's wet surfaces can be divided into four main categories. The first category is the outer-body of the car, consisting of the body panels, windows, mirrors, wipers etc. The second category is the under-body, consisting of all the parts located on the bottom surface of the car, such as the exhaust system. The third category involves the engine compartment and the radiator-condenser assembly, with the fourth category being the rotating wheels. As shown in Fig. 1.1 in the form of a pie chart, the rotating wheels are responsible for roughly 20% of the car's aerodynamic drag. The engine compartment along with the under-body contributes another 30% with the remaining 50% caused by the outer-body [3].

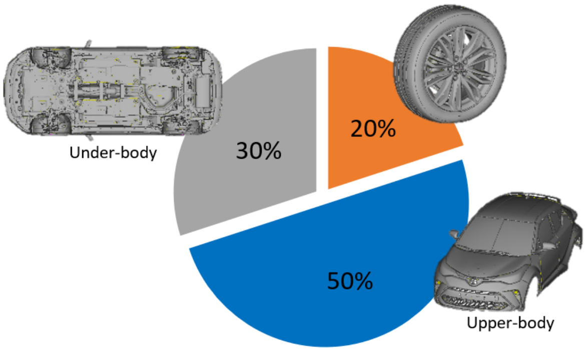

Figure 1.1: *Aerodynamic drag distribution on car's surfaces.*

Although the outer-body is the main contributor, reducing the drag by changing the design of the outer-body often conflicts the aesthetic appeal of the car. This conflict between drag reduction and aesthetics is also present in wheel designs. However, the characteristics of the flow in the proximity of the rotating wheels are harder to model correctly, due to the intense turbulence created by the rotating spokes, the complex brakes assembly, the tire's treads and the contact area between the tire and the road, often referred to as contact patch. Furthermore, the wake created by the rotating wheels, especially the front wheels, has an impact on the aerodynamics of the rest of the car, making the correct modelling of this phenomena even more important. Therefore, being able to compute the aerodynamic drag accurately using CFD simulations is of high demand in car industries.

As shown in [4], there are three main approaches to modeling the rotation of the wheels in cars. The Rotating Wall Boundary Condition (RWBC) approach, commonly referred to as Tangential Velocity (TV), is the least computationally demanding approach. It can be used both with steady or unsteady solvers. In the TV approach, the wheels remain stationary and the rotation is approximated using an appropriate velocity boundary condition over their surface. The TV approach cannot, however, model the rotation of complex geometries (eg. the spokes) correctly. For the Multiple Reference Frame (MRF) approach, a domain is selected in which the flow is solved w.r.t. a rotating frame of reference. Outside of this domain a stationary reference frame is used. Therefore the flow is solved using two reference frames. The MRF method can be used both with steady and unsteady solvers. This approach is also computationally not so expensive, however its accuracy in simulating the rotation of the spokes is poor [4]. Finally, the state-of-the-art approach, the Sliding Mesh (SM) approach, has the highest accuracy while being by far the most computationally expensive approach out of the three. In the SM approach, selected components of the wheel are physically rotated during the simulation. The SM approach requires unsteady simulations since the position of the rotating components changes on each time-step. Although this method has proven its ability to resemble the WT data, the integration of the SM method to the vehicle development workflow is still an open issue due to the high run-times that are a huge set-back in the fast paced automotive industry.

Another area of interest, included in capturing the impact of rotating wheels, is the correct simulation of the tread of the tire. The tires of commercial cars have longitudinal cut-outs, often referred to as grooves, and lateral cut-outs, often referred to as treads. These cut-outs are designed in order to make the car safe-to-drive in rainy conditions and prevent hydroplaning, but as [5] describes, they have a big aerodynamic impact. This aspect of the wheel rotation problem is still an open issue since the methods in hand and the subsequent meshing techniques have not yet been developed to the point necessary, making it hard for these methods to be included in the vehicle development workflow.

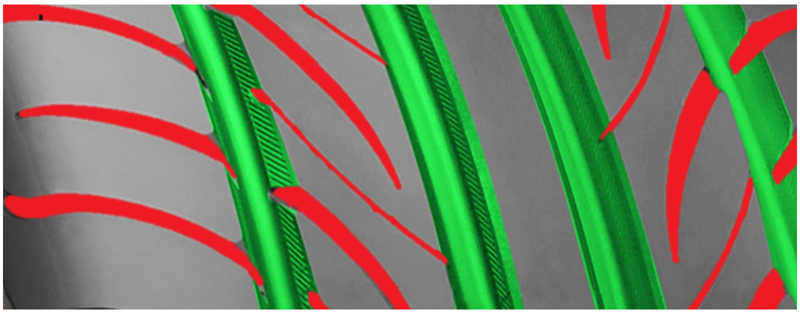

Figure 1.2: *Red Colour: Tire Tread, Green Colour: Tire Groove.*

1.3 CFD Mesh Generation

Every CFD analysis begins with the generation of the computational mesh. The generation of the mesh is a complicated procedure and still an open field of study with plenty of room for improvement. The quality of the mesh not only affects the quality of the results, but it also affects the computational cost of the simulation. As shown in [4], different handling is required for the various approaches described above, with the SM method being the most vulnerable w.r.t. the mesh quality, due to the special needs presented in physically rotating one part of the computational domain.

This vulnerability conflicts with the robustness that is necessary for a SM based workflow to fit the industrial needs. Furthermore, the simulation cost for the SM approach is directly linked to the characteristics of the interface between the rotating and the stationary domain of the mesh, referred to as Arbitrary Mesh Interface (AMI) in the *OpenFOAM*© vocabulary.

For the investigation on impact of the treaded tires, new meshing techniques need to be introduced, that can capture the detailed patterns of modern tire designs and are robust enough to meet the industry standards.

The wide variety of mesh generation software offers solutions in order to tackle the challenging meshing tasks required for each approach. Open source solutions, such as the *snappyHexMesh* mesh generator, available in the main distribution of *OpenFOAM*© have been providing acceptable quality meshes for most of the methods described above. However, as shown in [4], the special meshing needs of the SM approach, cannot keep up with the industry need from a robustness point of view. Therefore, a new two-step meshing strategy is introduced combining two different meshing methods. In the context of this work, a commercial mesh generator is also used for the SM approach, whereas for the treaded tire investigation both *snappyHexMesh* and a commercial mesh generator were used.

1.4 Thesis Outline

The scope of this thesis is to introduce a robust technique for generating meshes for the SM approach, that aims to reduce the simulation cost and increase the accuracy of the simulation. The key points that increase the simulation cost for the SM approach are identified and a new approach for the SM mesh generation is proposed. This method takes advantage of two meshing approaches. The first starts with the generation of a background mesh, which is then wrapped around the given surface (wrapping). The second starts with the generation of a surface mesh. Based on this surface mesh, the volume mesh is generated. The robustness and accuracy of the mesh generation process is tested on four different wheels for the same passenger car. Then, the accuracy of the simulation is examined in the $OpenFOAM^{©}$ environment for the simulation of the flow for one of the wheels. Starting point of this thesis is the work presented in [4].

In Chapter 2, the flow equations that are solved in the $OpenFOAM^{©}$ environment, in order to compute the flow field around the car, are presented, along with the turbulence model and the wall treatment used on the scope of this work. Furthermore, the discretization schemes and the solution strategy is presented.

In Chapter 3, the different methods that were used for the SM approach and the tire tread investigation are being presented.

In Chapter 4, the meshing approach for a SM-based CFD simulation , consisting of two steps, is explained, using two different meshing approaches. Also, the meshing approach for the treaded tire investigation is presented.

In Chapter 5, the results for the SM method are compared with the TV one. The method's accuracy is assessed, by comparing the drag coefficient to the Wind Tunnel data, and the gains in simulation cost are presented, as a result of the new meshing process. Also, the results for the treaded tire impact investigation are presented, by comparing a grooved and a treaded tire.

Chapter 2

CFD Analysis in the *OpenFOAM*© Environment

In this chapter the governing equations solved for the computation of the flow field around the car are presented. For the simulations, the open-source CFD software *OpenFOAM*© is used.

2.1 Incompressible Flow Equations

The equations solved for the computation of the flow field, are the Navier-Stokes equations for an incompressible flow. Equation (2.1) describes the conservation of mass whereas equation (2.2) describes the conservation of momentum,

$$\nabla \cdot u = 0 \tag{2.1}$$

$$\rho \frac{\partial u}{\partial t} + \rho (u \cdot \nabla) u = -\nabla p + \nabla \cdot (\mu \nabla u) \tag{2.2}$$

where $\frac{\partial u}{\partial t}$ is the time derivative, u is the velocity vector field, p is the pressure, ρ is the flow's constant density of the fluid and μ is the viscosity of the fluid. Here it is assumed that the density of the fluid ρ and its viscosity μ are constant.

2.2 Turbulent Flow Modeling

This thesis focuses on the flow around a moving passenger car, with special attention given to the effects of rotating wheels. The rotation of the wheels along with the complexity of the car's geometry result in a highly unsteady, turbulent flow. The shear stresses between the solid boundaries of the geometry and the fluid molecules, plus the stresses between the molecules themselves, result in the generation of vortexes, often referred to as eddies. The variety in the scale and intensity of these eddies, results in a chaotic highly unstable and turbulent flow, posing a challenge for the CFD solvers. The turbulent characteristics of the flow are expressed by scale fluctuations of the field variables. All the different frequencies of these fluctuations develop in parallel through time, forming a spectrum. Furthermore, all the different eddies interact with each other while moving through the flow, resulting in an increased friction drag on the solid surfaces of the domain.

The exact representation of these fluctuations without the use of a turbulence model is a very computationally costly approach, referred to as DNS (Direct Numerical Simulation) [6], where a very refined discretization through space (refined mesh) and time (small time-steps) is needed to achieve accurate results. The immense computational cost is a red flag for implementing this approach into an industrial workflow. Therefore, turbulence models are used instead.

2.2.1 Reynolds Averaged Navier-Stokes

The Reynolds-Averaged Navier-Stokes equations [8], often referred to as RANS (or Unsteady-RANS when including the unsteady term $\rho\frac{\partial u}{\partial t}$), is a result of the time averaging of the instantaneous Navier-Stokes equations described in equations (2.1), (2.2). For this approach, the instantaneous field quantities are decomposed into an average and a fluctuating value,

$$\phi = \underbrace{\bar{\phi}}_{\text{Average Value}} + \underbrace{\phi'}_{\text{Fluctuation}} \tag{2.3}$$

The visual representation of eq. (2.3) is given for the velocity value of an unsteady flow in Fig. (2.1).

Applying eq.(2.3) into the Navier-Stokes equations and, then, averaging result in the RANS equations described in eq. (2.4) & (2.5), where the Einstein notation is used,

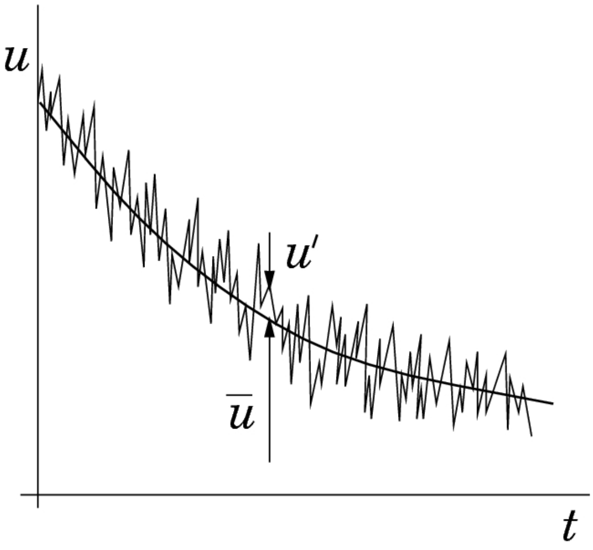

Figure 2.1: *Average value and fluctuation of the velocity field, from [7].*

$$\frac{\partial \overline{u_j}}{\partial x_j} = 0 \tag{2.4}$$

$$\rho\frac{\partial \overline{u_i}}{\partial t} + \rho\overline{u_j}\frac{\partial \overline{u_i}}{\partial x_j} = \frac{\partial}{\partial x_j}\left[-\overline{p}\delta_i^j + 2\mu\overline{S_{ij}} - \rho\overline{u_i'u_j'}\right] \tag{2.5}$$

where

$$\overline{S_{ij}} = \frac{1}{2}\left(\frac{\partial \overline{u_i}}{\partial x_j} + \frac{\partial \overline{u_j}}{\partial x_i}\right) \tag{2.6}$$

In Eq. (2.5), the term $(-\rho\overline{u_i'u_j'})$ is often referred to as Reynolds Stress term. For this term, the Boussinesq hypothesis is introduced (eq.(2.7)), adding a new variable, ν_t, referred to as the turbulent eddy viscosity,

$$(-\overline{u_i'u_j'}) = \tau_{ij}' = \nu_t\left(\frac{\partial \overline{u_i}}{\partial x_j} + \frac{\partial \overline{u_j}}{\partial x_i}\right) - \frac{2}{3}k\delta_i^j \tag{2.7}$$

where $k = \frac{1}{2}\overline{u_i'u_i'}$ is the turbulent kinetic energy, and τ_{ij}' is the Reynolds Stress term.

In order for the system of equations to close, ν_t needs to be expressed with the help of a turbulence model.

2.2.2 The Spalart-Allmaras Turbulence Model

The Spalart - Allmaras Turbulence model [9] is a one PDE model for incompressible flows. The model originated from aerospace applications but has shown to be accurate for predicting boundary layers subjected to adverse pressure gradients. For the Spalart-Allmaras model, a new variable $\tilde{\nu}$ is introduced, referred to as the Spalart-Allmaras variable, so that the value of the eddy viscosity (ν_t) can be derived using the following equations,

$$\nu_t = \tilde{\nu} f_{v1} \tag{2.8}$$

$$f_{v1} = \frac{X^3}{X^3 + C_{v1}^3} \tag{2.9}$$

$$X := \frac{\tilde{\nu}}{\nu} \tag{2.10}$$

where ν is the kinematic viscosity of the fluid,

$$\frac{\partial \tilde{\nu}}{\partial t} + u_j \frac{\partial \tilde{\nu}}{\partial x_j} = C_{b1}[1 - f_{t2}]\tilde{S}\tilde{\nu} + \frac{1}{\sigma}\{\nabla \cdot [(\nu + \tilde{\nu})\nabla \tilde{\nu}] + C_{b2}|\nabla \tilde{\nu}|^2\} - \left[C_{w1} f_w - \frac{C_{b1}}{\kappa^2} f_{t2}\right]\left(\frac{\tilde{\nu}}{d}\right)^2 + f_{t1}\Delta U^2 \tag{2.11}$$

where $\sigma = 2/3$, $C_{b1} = 0.1355$, $C_{b2} = 0.622$, $\kappa = 0.41$, $C_{w1} = 3.239$, $C_{v1} = 7.1$ are the model's constants. Variable d is the distance to the closest solid surface. $\tilde{S}, f_{t2}, f_w$ are calculated using the following equations:

$$\tilde{S} = S + \frac{\tilde{\nu}}{\kappa^2 d^2} f_{v2} \tag{2.12}$$

$$S = \sqrt{2 S_{ij} S_{ij}} \tag{2.13}$$

$$f_{v2} = 1 - \frac{X}{1 + X f_{v1}} \tag{2.14}$$

$$f_w = g\left[\frac{1 + C_{w3}^3}{g^6 + C_{w3}^3}\right]^{1/6} \tag{2.15}$$

$$g = r + C_{w2}(r^6 - 6) \tag{2.16}$$

$$r = min\left[\frac{\tilde{\nu}}{\tilde{S}\kappa^2 d^2}, 10\right] \tag{2.17}$$

$$f_{t2} = C_{t3} e^{-C_{t4} X^2} \tag{2.18}$$

where $C_{w2} = 0.3$, $C_{w3} = 2$, $C_{t3} = 1.1$, $C_{t4} = 2$ are the constants corresponding to the equations (2.12) to (2.18), S_{ij} is given by eq. (2.7).

In its original form, this model is effectively a low-Reynolds number model, requiring the viscosity affected region of the boundary layer to be properly resolved ($y^+ \sim 1$). In order for this approach to work, the mesh has to be well refined near the solid boundaries of the computational domain, therefore resulting in high computational cost, due to the increased cell counts. Therefore, a different approach for the area close to the wall is needed, that can correctly predict the steep gradients, without the need for an overly-refined mesh near the solid boundaries of the computational domain. In the context of this thesis, wall functions are used for the computation of the gradients near the solid walls. The mesh generated in this work, complies with the theoretical background of wall functions.

2.2.3 Near-Wall Treatment

The correct capturing of the velocity gradient near the wall surface, is directly linked to the correct approximation of the skin friction drag. In order to correctly predict these gradients without increasing the resolution of the mesh near these wall surfaces, the use of wall functions is introduced. The wall functions are empirical equations that are tuned to reproduce the characteristics of the flow near the wall region. This approach is referred to as High-Reynolds modeling and is used as an alternative to low-Reynolds methods, that require the first cell of the mesh to reside inside the viscous sub-layer.

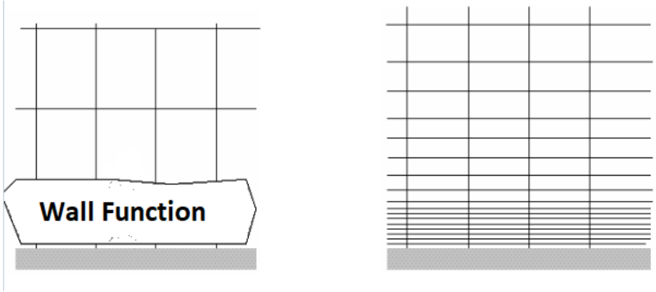

Figure 2.2: *Left: Wall Function Approach, Right: Refined Mesh Approach.*

The dimensionless wall distance y^+ and velocity u^+ are introduced:

$$y^+ = \frac{u_\tau y}{\nu} \tag{2.19}$$

$$u^+ = \frac{u_\tau}{u} \tag{2.20}$$

where u_τ is the local tangential or friction velocity, y is the distance from the surface, ν is the kinematic viscosity and u is the free-stream velocity.

The boundary layer developed close to the wall surface is explained in a dimensionless way in fig. 2.3 through the y^+ & u^+ variables. Three key areas are identified. The viscous layer ($y^+ \sim 1 - 5$) inside of which the effects of viscosity result a linear relation between u^+ & y^+, The log-law region ($y^+ \sim 30 - 100^+$) where the effects of turbulence cause a logarithmic relation between u^+ & y^+. The log-law region is presented as a straight line as a result of the log-scaled x-axis in Figure 2.3. Finally the Buffer zone ($y^+ \sim 5 - 30^+$) is a transitional area where the log-law approach and the linear approach show a poor fit to the typical velocity profile. Therefore, a continuous function has to be introduced for the entire range of y^+.

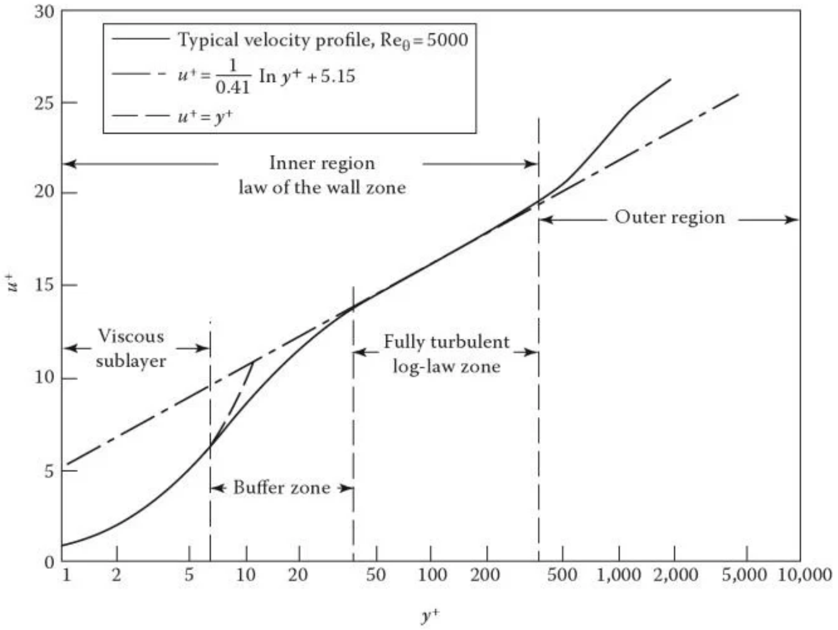

Figure 2.3: *Dimensionless velocity profile close to the wall, from [25].*

For this work, the Spalding Wall Function [11] is used ,

$$y^+ = u^+ + \frac{1}{E}\left[e^{\kappa u^+} - 1 - \kappa u^+ - 0.5(\kappa u^+)^2 - \frac{1}{6}(\kappa u^+)^3\right] \tag{2.21}$$

where $E = 9.53$ is a wall roughness parameter, and $\kappa = 0.41$ is the von-Karman constant.

The implementation of this method in *OpenFOAM*© is through the modification of the turbulent viscosity ν_t,

$$\nu_t = \frac{u_\tau^2}{\frac{\partial u}{\partial n}} - \nu \tag{2.22}$$

where u_τ is the tangential velocity, computed based on the y^+ value, n is the normal-to-surface direction and ν is the kinematic viscosity.

Implementation in the *OpenFOAM*© environment requires imposing a boundary condition for the ν_t field on the solid boundaries of the computational domain (*nutUSpaldingWallFunction* [11]).

In this work, the RANS equations are solved along with the S-A turbulence model and the use of wall functions in order to acquire an initialization of the field. This initialization will then be used for the unsteady part of the simulation.

2.2.4 Delayed Detached Eddy Simulation

For the transient simulations the Delayed Detached Eddy Simulation (DDES) model is used [12]. This model is a RANS-LES hybrid model, combining the speed of RANS and the accuracy of LES. Based on the Spalart-Allmaras model, the DDES model is a modification of the Detached Eddy Simulation (DES) model [13]. For the DDES approach, the d variable of equation (2.11) is modified accordingly:

$$\overline{d} = max\left[d - f_d, max(d - C\Delta, 0)\right] \tag{2.23}$$

$$f_d = 1 - \tanh\left[(8r_d)^3\right] \tag{2.24}$$

$$r_d = min\left(\frac{\nu_{eff}}{|\nabla u|\kappa^2 d^2}, 10\right) \tag{2.25}$$

where $\overline{d}$ is the DDES model length scale, d is the distance to the wall, C is a calibration constant equal to 0.65, Δ is the characteristic cell size. Finally, κ is the von-Karman constant and ν_{eff} is the effective viscosity equal to the sum of the kinematic and turbulent viscosity $(\nu + \nu_t)$.

By the calculation of f_d the model switches from RANS (for $f_d = 0$) in the attached boundary layers, to LES ($f_d = 1$) in the detached flow regions where $r_d << 1$. Equations (2.25) & (2.24) indicate that the switch to LES depends not only on the grid scale, but also on the time-dependent eddy viscosity field ν_{eff}. The modification of the DDES length scale $\overline{d}$ prevents the immature switch to LES within boundary layers and delays the switch until outside of it.

In this work, the SA-DDES model with the use of the above-mentioned wall-functions is used for the unsteady part of the simulation, implemented in the environment of *OpenFOAM*$^{©}$ v2106 [26].

2.3 Discretization of the N-S equations

In order for the N-S equations to be solved, the domain should be discretized into small sections called cells. This is the result of the mesh generation process presented in Chapter 4. The above-mentioned equations are solved in the *OpenFOAM*$^{©}$ environment using the cell-centered Finite Volume method [27].

For both full-car and treaded tire simulations, the field is first initialized using a steady state solver (simpleFOAM [21]) for 7000 iterations, so that a converged field is acquired.

Then, an incompressible unsteady CFD solver is used (pimpleFOAM [28]). The transient part of the simulation lasts for three seconds. The time-step is set at $\Delta t = 1.4 * 10^{-4}[sec]$ for the transient part of the simulation. The DDES Spalart-Allmaras model is used with wall functions (Section 2.2). For each time-step of the unsteady simulation, a pressure corrector field is computed (*pcorr*) in order to correct the velocity field for the continuity equation to be satisfied.

For the time derivative discretization, a second order backward scheme was applied. The convection term was discretized using a second order linear upwind scheme. For the interpolation of the quantities a linear scheme was used whereas for the Laplacian Term a linear limited scheme was selected.

After the first second of the transient simulation has elapsed, the average values of the flow variables ($\overline{p}$ and $\overline{U}$) are computed ($1[sec] \rightarrow 3[sec]$) for a total of 2 sec. Based on these values, the averaged coefficient of drag (C_D) is calculated.

2.4 Boundary Conditions

In order for the PDEs to be solved, Boundary Conditions (BC) must be imposed on the boundaries of the computational domain.

2.4.1 Full-car Simulations

Boundary conditions for the full-car simulations are presented in this section. The computational domain, is presented along with the car and the key surfaces on which different BC will be imposed, in Fig. 2.4.

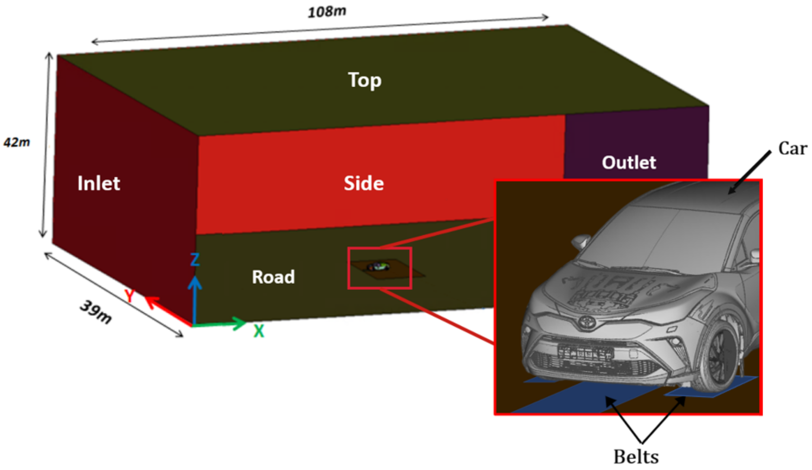

Figure 2.4: *Computational domain dimensions.*

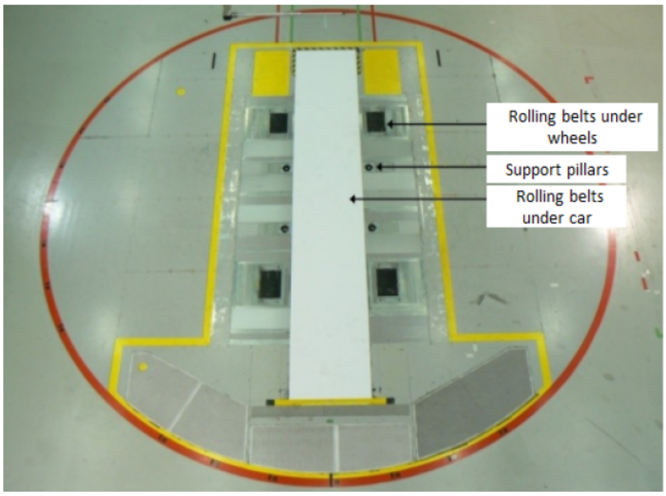

Figure 2.5: *S2A GIE wind tunnel in France, Versailles. From [21].*

The belts highlighted in Fig. 2.4 are separated parts of the Road surface, so that a different BC can be used. This is done in order to mimic the Wind Tunnel setup, where five moving belts (one for each wheel and one under the car's under-body) are simulating the movement of the road and cause the wheels to rotate. The floor of the Wind Tunnel setup is presented in Fig. 2.5.

The correct representation of the Wind Tunnel setup is essential to the simulation since the resulting drag coefficient will be compared to the value measured during a test for the same car setup. This way the accuracy of the simulations can be compared with real world data.

An overview of the boundary conditions imposed on the boundary surfaces of the domain are presented in Table 2.1.

Boundary Conditions		
Variable:	Velocity	Pressure
Top / Side	Symmetry	Symmetry
Inlet	Dirichlet (27.78[m/s])	Zero Neumann
Outlet	Inlet-Outlet	Zero Dirichlet
Road	Slip	Zero Neumann
Belts	Dirichlet (27.78 0 0)	Zero Neumann
Car	No Slip*	Zero Neumann

Table 2.1: *Boundary conditions used for the full-car simulations.*

(*) In the majority of the car's surfaces the *NoSlip* (zero Dirichlet) boundary condition is imposed. However, depending on the simulation type, different BCs are imposed on different surfaces of the wheels assembly. The detailed overview of the BC for the surfaces of the wheel assembly is presented in Section 4.2.3.

2.4.2 Single Wheel Simulation

For the impact of the treaded tire investigation, a single-wheel model is used, where the MRF method is used in order to capture the rotation of the treaded tire. The computational domain is presented in Fig. 13.

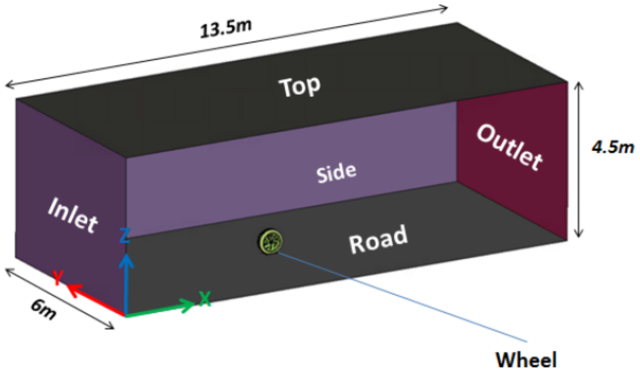

Figure 2.6: *Computational Domain of the single wheel simulation, for the tread impact investigation, from [4].*

Boundary Conditions		
Variable:	Velocity	Pressure
Top / Side	Symmetry	Symmetry
Inlet	Dirichlet (27.78[m/s])	Zero Neumann
Outlet	Inlet-Outlet	Zero Dirichlet
Road	Dirichlet (27.78[m/s])	Zero Neumann
Wheel	No Slip*	Zero Neumann

Table 2.2: *Boundary conditions used for the Tire Tread Investigation simulations.*

Table 2.2 gives an overview the BC imposed on the domain's boundaries. Here, the belts are not used, and the whole road surface is moving. The BC imposed on the surfaces of the tire are presented in detail in Section 4.3.3.

Chapter 3

Modeling the Rotation of the Wheel

As explained in Chapter 2, the wheels of the car contribute to the total aerodynamic drag of a vehicle, in a noticeable percentage. Furthermore, the wake created by the front wheels affects the aerodynamics of the rest of the car. It is clear that the correct capturing of the flow field around rotating wheels and, also, along their wake is essential for the aerodynamic evaluation of a given vehicle.

Simulating the rotation of each component in the CFD environment correctly, is a very demanding problem. As presented in [4], three main approaches exist. The computational cost of each of these approaches is directly related to their accuracy, when compared with wind-tunnel data.

In this chapter, the modeling approaches used for this work are introduced, focusing on the advantages and disadvantages of each one of them. Equations describing each modeling method are presented. Finally, the use of each approach on the different parts of the geometry is explained.

3.1 Wheels Assembly

A car composes of many stationary and rotating parts. Not every rotating part is influential to the flow characteristics. As the aerodynamic influence of the rotation of each of the parts varies, so does the need for accurate simulations that can capture the effects of the rotation. Complex rotating, geometries like the driveshafts and the fans in the cooling assembly, do not have the same influence as the rotation of the spokes in the wheels assembly. Therefore, although computationally inexpensive approaches exist for mimicking the rotation, they can't all be applied in the same way for every part of the rotating geometry, without a drop in the accuracy of results.

The application of each method for a certain part of the rotating assembly depends on its geometrical characteristics. The rotating geometry of the wheels complex, composed of various parts. This poses a challenge in developing robust and accurate CFD methods for capturing the details of the flow in the proximity of these parts.

Focusing on the rotating wheels assembly, the main parts are presented in Fig. 3.1.

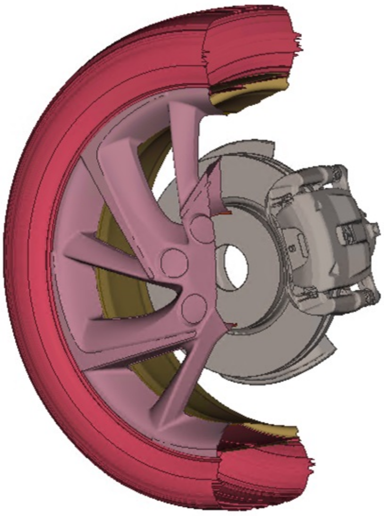

Figure 3.1: *Wheels Assembly of a passenger car*

The assembly presented in Fig. 3.1 can be broken into four parts. The spokes, the tire, the inner rim, and the brakes assembly. Those parts are represented in Fig. 3.2 in an exploded view.

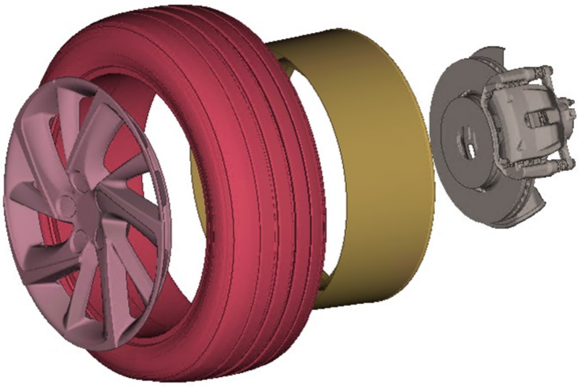

Figure 3.2: *Left to Right: Spokes, Tire, Rim, Brakes Assembly*

- **Brakes Assembly**
  The Brakes Assembly composes of both stationary and rotating parts. In detail, the brake disc is rotating inside the brakes caliper. The interaction between the rotating brake disc and the stationary brake caliper is not something that this work is focusing on. However, one of the key points of interest for this work is the geometrical proximity of the stationary brake caliper with the rotating spokes. This proximity causes certain limitations in the mesh generation process. These limitations are explained in detail in Chapter 4.

- **Inner Rim**
  The Inner Rim is physically connected with the spokes. However, for the purposes of this work, the rim and the spokes are separated due to the different geometrical complexity each of them presents. The Inner Rim is solely a rotating part. Furthermore, the rim's surface can be considered as a revolved surface around the axis of the wheel's rotation. Therefore, simplistic models in the form of RWBC can be used , and no challenge is opposed in the accurate representation of the rotation of this part.

- **Spokes**
  The spokes of the wheel is the most complicated rotating geometry on the car. The spokes of the car moving through the air while also rotating around the wheel axis, result in a chaotic flow field, that affects the aerodynamic resistance of the whole car. The geometrical complexity of the spokes, and their proximity to the stationary brakes caliper makes the simulation of this part's rotation very difficult. Different approaches exist when it comes to modeling the spokes rotation correctly, with the Sliding Mesh method having the highest accuracy [4], compared to the TV and MRF approaches.

  The impact of the spokes is not confined to the aerodynamics of the car, but also drastically affects the car's aesthetic design. Taking into consideration that the same model can be available in various set-ups (each set-up being a different spokes design), the need for a robust and accurate simulation method for the rotation of the spokes is clear. This work focuses on the implementation of the SM technique in a robust and efficient manner, focusing on the reduction of the simulation cost of the method.

- **Tire**

  The tire, in its un-deformed and slick approach, could be described as a revolved surface around the axis of the wheel's rotation. This would make the simulation of the tire's rotation as simple as imposing a boundary condition for the velocity component. However, in reality the tire is neither un-deformed nor slick [29], the latter being a very big obstacle to overcome. Figure 3.3 depicts a slick, a grooved and a fully treaded tire (left to right). A slick tire is similar to the ones used in race cars, in order to maximize the contact surface area between the tire and the road. The treaded tire is widely used on passenger cars. The tread pattern's purpose is to displace the water present on the road in rainy conditions. A grooved tire, not common in the real world, is used by the majority of CFD simulations [4] as a simplified version of the real-world fully treaded tire. The impact of the treads is often disregarded. Including the lateral treads in the geometry of the tire cancels its axi-symmetric shape, resulting in the need for different methods to be used. This work includes an investigation on the method used for capturing the tread impact.

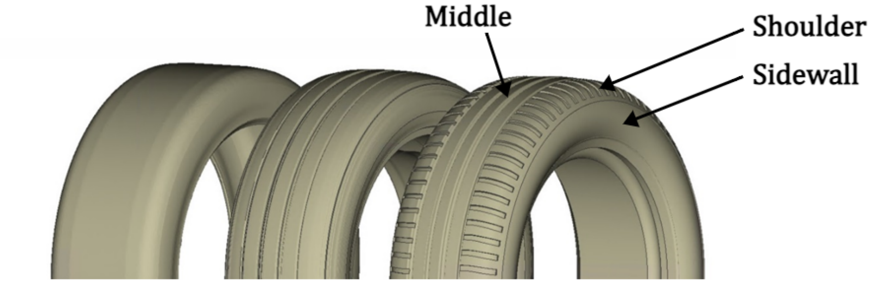

Figure 3.3: *Left to Right: Slick, Grooved, Treaded Tire and corresponding zones.*

The tire's surface can be split into three main zones. The area that is in contact with the road is often referred to as "Treaded Area" or "Middle Area". Continuing outwards, there is the Shoulder area. This area is not completely in contact with the road, unless the vehicle is in a turn. Finally, there is the Sidewall area where no treaded patterns exist. In this area, it is common for the tire's characteristics to be printed (eg. radius and width of the tire). These zones are presented in Fig. 3.3.

Another factor adding to the tire's geometry complexity is the deformation caused by the tire's rotation and its contact with the road surface, referred to as contact-patch. The deformation of the tire surface can be considered as the sum of the dynamic deformation and the static deformation. The dynamic deformation is caused by the centrifugal forces exerted on the elastic surface of the tire caused by the tire's rotation, and affects both the width and the outer-radius of the tire. Added to the dynamic deformation is the static deformation caused by the contact forces between the elastic surface of the tire and the rigid surface of the road. The accurate geometry representation for the contact patch, and for the whole of the tire's surface is highly influential to the accuracy of the results. For this work, a fully-deformed grooved tire is used for the full-car simulations, whereas for the treaded tire investigation, an undeformed tire is assumed.

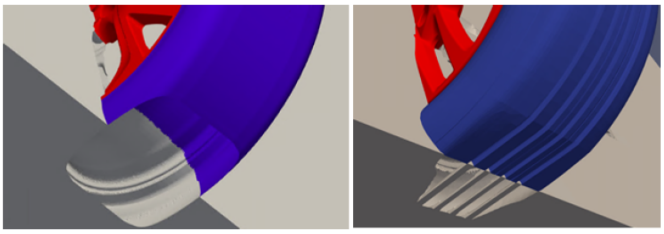

Figure 3.4: *Deformation of the tire due to the contact patch. Left: Slick Tire, Right: Grooved Tire. From [4].*

3.2 Treaded Tire Impact

The impact of the treaded tire, and the differences in the flow field when compared to the grooved approach, is a part of this thesis.

The tread is a unique geometrical characteristic of each tire. However, the dimensions of the tread pattern, are often very small (a couple of millimeters), hence making the mesh generation process complicated.

In this work, the geometry of the tread pattern is captured on the generated mesh. This requires detailed handling of the mesh generation process in that area. Furthermore, a detailed geometry should exist, accurate enough for the meshing software to step on. This approach is used in this diploma thesis in order to examine the impact of the treaded tire, compared to the currently used grooved tire approach.

3.3 Wheel Rotation Modeling Methods in CFD

In this section the equations that describe each of the used methods are presented. Each method varies on its ability to model the rotation correctly and its computational cost. Each method is applied in order to mimic the rotation of the component they are applied to. The accuracy in the use of each method highly depends on the component's geometrical characteristics.

3.3.1 Rotating Wall Boundary Condition

The Rotating Wall Boundary Condition (RWBC), often referred to as Tangential Velocity (TV), is the simplest way of modeling rotating components in CFD, both from meshing requirements and computational complexity perspective. However, method introduces a lot of errors when applied to non axi-symmetric geometries, such as the spokes or the treaded tires. However, when applied to axi-symmetric (relative to the axis of revolution) surfaces, the errors are reduced and the physical phenomena of the rotation is simulated adequately well. Therefore, this method can be used alongside the other methods for certain parts of the geometry.

The method is applied as a boundary condition for the velocity field on the given component's surface. In detail, a velocity vector is imposed on the centre of each face-centroid. The magnitude of the imposed velocity is given by,

$$|\vec{\Omega} \times \vec{r}| \tag{3.1}$$

where $\vec{\Omega}$ is the angular velocity vector and $\vec{r}$ is the position vector of the face centroid relative to the rotational axis, the visual representation of which is given in Figure 3.5.

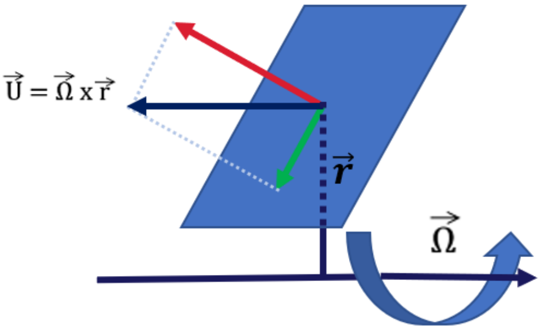

Figure 3.5: *Imposed velocity from the RWBC on a face centroid*

The $\vec{U}$ vector can be broken into a tangent (green) and a normal (red) component relative to the cell's surface. However, the conservation of mass prohibits the existence of the normal component of the velocity, as in that case, flow would be introduced from the surface of the solid boundary, thus violating the continuity principal. Therefore, when this method is applied on non-axi-symmetric surfaces, the representation of the velocity distribution for the rotating part is wrong, as shown in Figures 3.6 and 3.7.

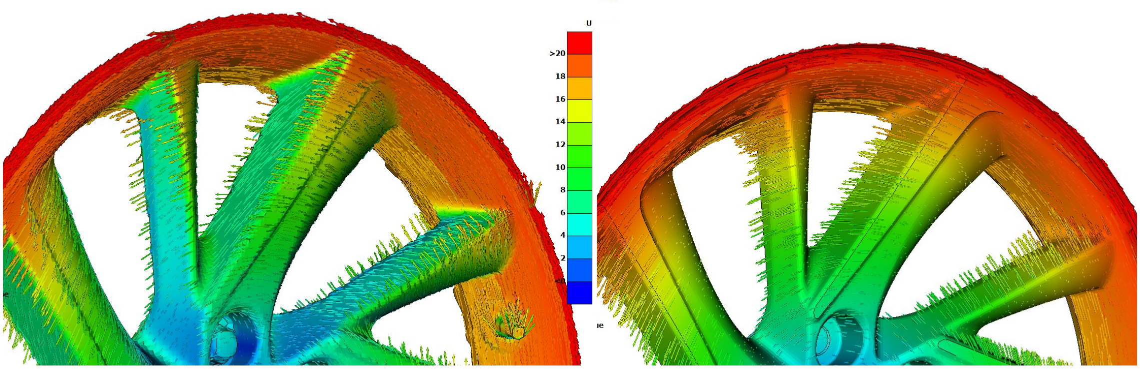

Figure 3.6: *Imposed velocity from the RWBC (left) and SM (right) on the surface of the rotating Spokes of a car*

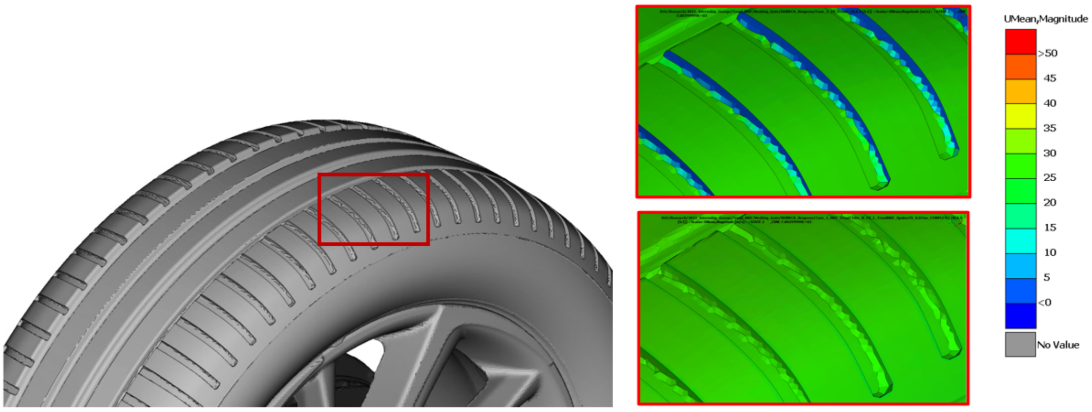

Figure 3.7: *Imposed velocity from the RWBC (Top) and the MRF condition (Bottom) on the surface of the rotating treaded tire of a car.*

Figures 3.6 & 3.7 accurately describe the vulnerability of the RWBC method when it comes to handling non axi-symmetric geometries. However, for the rest of the rotating surfaces, that is the grooved (non-treaded) tire and the rim, the geometrical simplicity allows the RWBC condition to be used without introducing errors in the simulation.

In general, the RWBC approach has no special meshing needs, and offers a computationally inexpensive solution since the mesh composes of a single domain which remains stationary throughout the simulation. However as figure 5.12 and the work in [4] suggests, its accuracy compared to WT data, is by far inferior.

3.3.2 Multiple Reference Frame

As the name suggests, the flow is solved using two reference frames, one of which is rotating, simulating the rotation of the surface. The MRF method requires a pre-defined ”Rotating” domain, in which the N-S equations are solved w.r.t. the rotating frame of reference. This domain is not actually rotating, therefore minimizing the need for accurate meshing of the domain’s boundaries. In Figure 3.8, the rotating velocity component imposed to the cells included in the ”Rotating” domain, is visualized.

The velocity from an observer on the stationary frame of reference, for a cell inside of the ”rotating” domain is:

$$\vec{V} = \vec{W} + \vec{\Omega} \times \vec{r} \tag{3.2}$$

where, $\vec{W}$ is the velocity w.r.t. the rotating frame of reference, $\vec{V}$ is the velocity w.r.t. the inertial or stationary frame of reference, $\vec{\Omega}$ is the rotational velocity vector and $\vec{r}$ is the location vector from the rotating axis to the cell centroid (Figure 3.8).

The N-S equations for w.r.t. the rotating frame of reference are expressed as:

$$\begin{cases} \frac{\partial \vec{W}}{\partial t} + \frac{d\vec{\Omega}}{dt} \times \vec{r} + \vec{W} \cdot \nabla \vec{W} + \underbrace{2\vec{\Omega} \times \vec{W}}_{\text{Coriolis Term}} + \underbrace{\vec{\Omega} \times \vec{\Omega} \times \vec{r}}_{\text{Centrifugal Term}} = -\nabla(p/\rho) + \nu_{eff} \nabla \cdot \nabla(\vec{W}) \\ \nabla \cdot \vec{W} = 0 \end{cases} \tag{3.3}$$

In eq. (3.3) two additional source terms appear as a result of substituting eq. (3.2) to the N-S equations. Through eq. (3.3) the W field can be derived and then through eq. (3.2) the inertial frame velocity V can be obtained.

Finally, the N-S equations w.r.t. the inertial frame of reference:

$$\begin{cases} \frac{\partial \vec{W}}{\partial t} + \frac{d\vec{\Omega}}{dt} \times \vec{r} + \vec{W} \cdot \nabla \vec{V} + \underbrace{\vec{\Omega} \times \vec{V}}_{\text{Source Term}} = -\nabla(p/\rho) + \nu_{eff} \nabla \cdot \nabla(\vec{V}) \\ \nabla \cdot \vec{V} = 0 \end{cases} \tag{3.4}$$

In eq. (3.4) the source term underlined is an extra term that results from the rearrangement of the variables. This term is included in the cells inside the ”rotating” domain and disregarded in the cells inside the stationary domain. In order to solve eq. (3.4) the term $\vec{W}$ needs to be expressed w.r.t. the inertial velocity which is done using eq. (3.2).

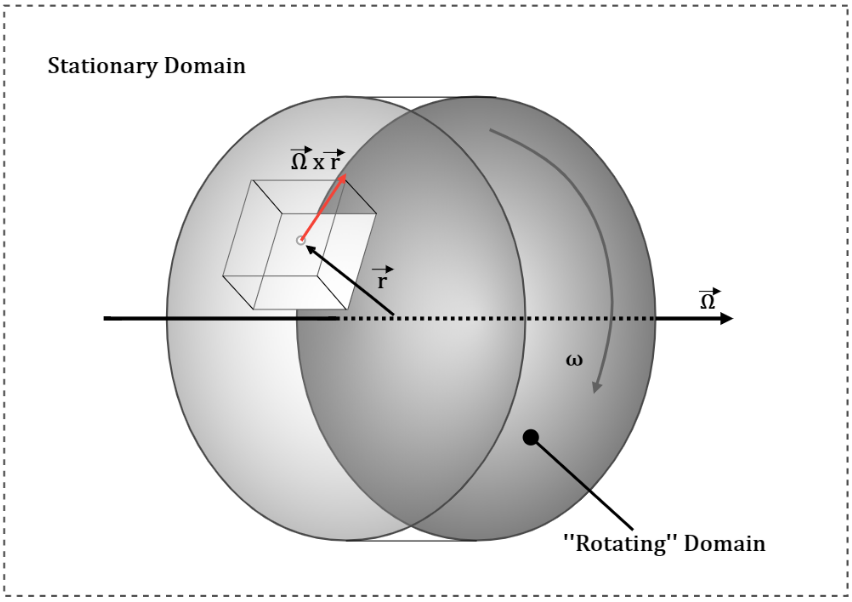

Figure 3.8: *Rotational Velocity component on the cell centroids located inside the domain on which the MRF approach is applied.*

The MRF approach is capable of modeling the rotation of the surfaces inside the rotating domain. The rotating domain should be separated from the rest of the domain in the mesh generation process. The domain does not need to be axi-symmetric, and also the use of multiple domains with different axis of rotation is possible. The interface between the stationary and the ”rotating” domain can either be fully conformal (node-to-node) correspondence or not. In the case of fully conformal interface, no special treatment in the interpolation of the field values between the interface is necessary. On the contrary, when using non-conformal interface, some sort of interpolation needs to take place. This interpolation needs to take place only once, since the ”rotating” domain is not actually rotating. This method’s advantage is the fact that it can model the rotation without the need of unsteady solvers. However, as described in the equations, the MRF approach is applicable in steady and unsteady simulations.

In this work, the MRF approach is used in two separate occasions. First, the MRF method is used with a steady solver in order to initialize the field for the unsteady portion of the simulation. Second, the MRF method is applied for the treaded tire impact investigation, used in both the steady and the unsteady part of the simulation.

3.3.3 Sliding Mesh

The Sliding Mesh approach is the most accurate in terms of representing correctly the effects of the rotating components. The components are rotating for every time-step of the unsteady simulation. In [4], the SM approach was the most accurate in determining both the aerodynamic resistance of the car, and the flow field in the proximity of the rotating wheels, when compared to wind-tunnel data. However, the approach was tested in only one setup, leaving room for further validation of the SM method for accurately predicting the flow field around a passenger car.

The SM method is used only with an unsteady flow solver. Like the MRF method, SM uses a pre-defined domain, in which the rotating components are located. This domain is generated in the mesh generation process (Section 4.2). Unlike the MRF approach, the boundaries of the rotating domain should be axi-symmetric. The reason is that unlike the MRF approach, SM uses a dynamic mesh motion solver [14] in order to physically rotate the domain. As shown in Fig. 3.9, during the unsteady simulation, the cells residing inside of the rotating domain are re-located in each time-step in order to account for the rotation. The parts that reside inside the rotating domain (e.g. the spokes in Fig. 3.9) will rotate. Therefore, the geometry changes in each time step, capturing the rotation of the wheels in the most accurate way possible.

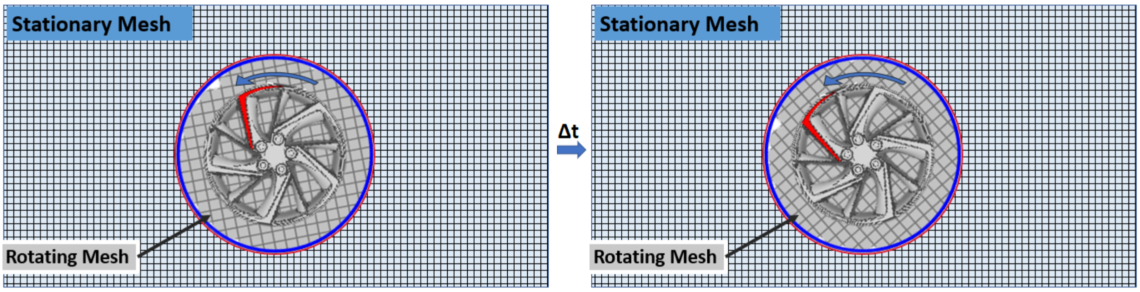

Figure 3.9: *Spokes are physically rotated for every time-step of the simulation*

Physically, rotating the domain introduces the need for some sort of interpolation between the boundaries of the stationary and the rotating domain, since the mesh in this region is no longer fully-conformal. A visual representation of the non-conformal area of the mesh is presented in Fig. 3.10, where the non-conformality is a direct consequence of the rotation of the inner, rotating (blue) part of the domain inside the outer, stationary (red) part of the domain. In order to interpolate the field values through the non-conformal faces, a weighed face area approach is used, explained in detail in section 3.3.3.2. This interpolation needs to be repeated for every time-step of the unsteady simulation, since the cells consisting the rotating domain are re-located with each time-step. As a result, the SM method suffers from increased simulation costs, when it comes to modeling the rotation of the wheels on a moving vehicle [4].

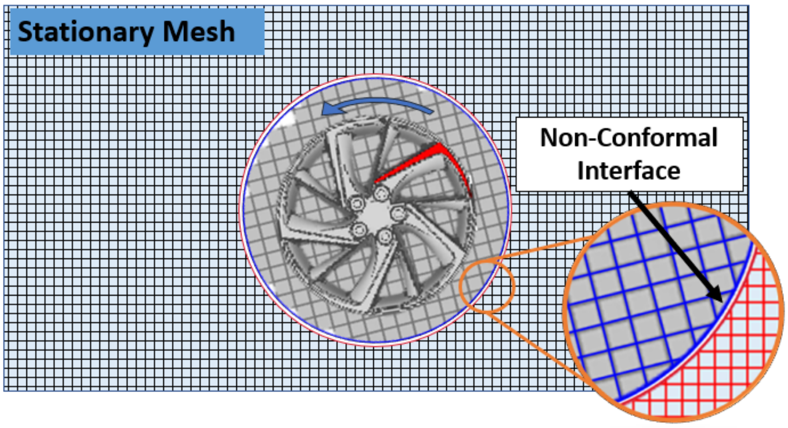

Figure 3.10: *Visual Representation of the non-conformal Interface in the SM method*

Furthermore, the quality of the mesh on the rotating and stationary domain interface directly affects the quality of the results. Ideally, no conservation errors should be introduced from the interpolation between the rotating and stationary interface. Conservatory interpolation methods exist, such as the General Grid Interface (GGI) [15] and the Arbitrary Mesh Interface (AMI) [16]. For this work, the AMI method is used for interpolating the fluxes between the stationary and rotating boundary faces, implemented on the distribution of *OpenFOAM*© v2106.

3.3.3.1 Arbitrary Mesh Interface (AMI)

For this work, the cell-centered approach for the Finite Volume Method (FVM) is used, implemented in the *OpenFOAM*© v2106 distribution, in order to compute the flow field around the given geometry. The FVM computes the flow field values at the center of each cell, but also requires the computation of values on the cell faces.

For a fully conformal mesh, such as the one presented on the left-hand-side of fig. 3.11, this is a simple task as several interpolation schemes can be selected [17] in order to interpolate the values of the cell centers P & N on the cells' common face and compute the value on the face Φ_f. However, for the SM approach, the interface between the rotating and stationary domain is composed of non-conformal cells as presented in fig. 3.10.

Focusing on the non-conformal interface, the right side of fig. 3.11 gives a visual representation of the problem. For the SM approach, this non-conformality is a direct result of the rotation of the cells inside the rotating domain, that causes the *Target* and *Source* interfaces to move w.r.t. each other. Since the neighbouring

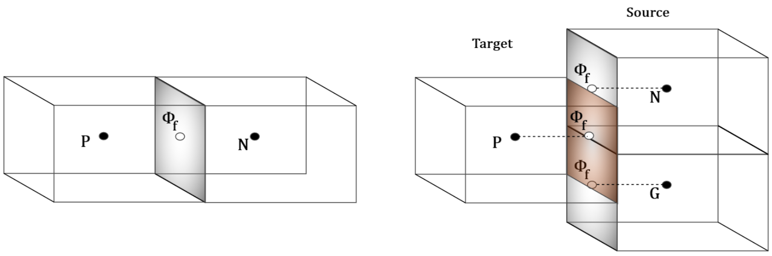

Figure 3.11: *Left: Fully-Conformal Mesh, Right: Non-Conformal Interface*

faces of the P & N - G cells are not shared, an interpolation should take place in order to compute the field values Φ_f for each face of the $Target$ and $Source$ interfaces.

3.3.3.2 AMI Weights' Calculation

The AMI interpolation uses face-area computed weights in order to interpolate the values of the non-conformal faces on the $Target - Source$ interface. These weights are computed for every face of both the $Target$ and $Source$ interface at each time-step of the unsteady part of the simulation.

Figure 3.12 shows one $Target$ face with a face area of A_{t1} and four $Source$ faces with a face are of A_{si} for each i face of the $Source$ interface that overlaps with the $Target$ face (for this example let $i = 4$). The projection of the $Target$ face area A_{t1} on the four $Source$ faces, results in the face area A_{si,t_1} which is the area of the i^{th} $Source$ face covered by the projection of the $Target$ face. With the above-mentioned areas, the AMI weights for every j^{th} face of the $Target$ patch are calculated as

$$w_{si,t_j} = \frac{A_{si,t_j}}{A_{tj}} \tag{3.5}$$

where w_{si,t_j} is the weight of the i^{th} face of the $Source$ patch to be used to interpolate the values on the j^{th} face of the $Target$ patch.

Note that in eq. (3.5), the i scale resets for every j $Target$ face for which the weights are computed, since only the overlapping faces between the given $Target$ face and $Source$ faces are used for the weights computation.

Using the weights computed through eq. (3.5), the flow field values Φ_{si} are interpolated to the flow field values Φ_{tj} on the faces of the target patch as

$$\Phi_{tj} = \sum_i w_{si,t_j} \Phi_{si} \tag{3.6}$$

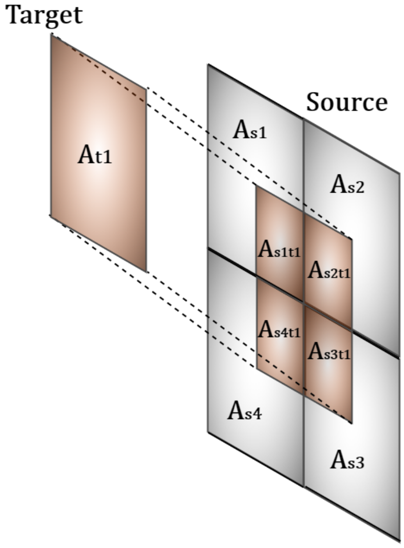

Figure 3.12: *Visual Representation of one Target face overlapping four Source faces*

The conservativeness is automatically assured as long as the sum of the weights is equal to 1,

$$\sum_i w_{si,t_j} = 1 \tag{3.7}$$

This is not always the case when handling complex geometries like the ones on the rotating wheels of a car. The quality of the mesh on these $Target$ and $Source$ patches is of very high priority in order for the SM approach to work properly. In [4], the correlation between the interface mesh quality and the interpolating weights is examined. Therefore, the meshing process must ensure that the quality of the interface is adequate.

The method described above is repeated for the computation of the $Target$ faces' weights in order to interpolate the values on the *Source* faces. A problem arising from this process is the immense computational cost required for the calculation of the areas used to compute weights [eq. (3.5)]. First, for each $Target$ face, the overlapping faces of the *Source* element should be identified. This process is conducted using an advancing front technique [18] described visually in fig. 3.13. After this step, the *Source* faces overlapping each $Target$ face have been identified.

After the overlapping faces have been identified, the areas described in eq. (3.5) are computed by identifying the intersections between the face boundaries as shown in fig. 3.14. Therefore, the intersection area can be evaluated and be used in eq. (3.5).

By completing this step, for each $Target$ face, the weights are calculated and, using

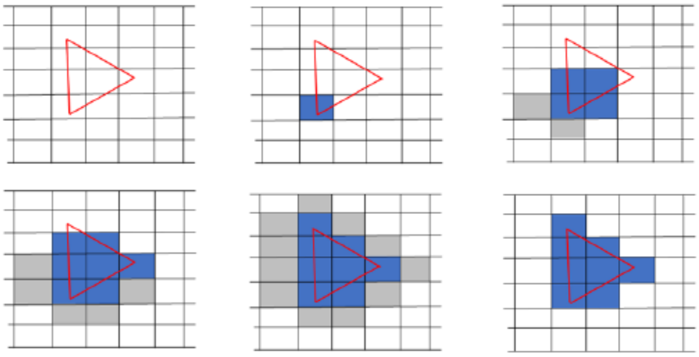

Figure 3.13: *Visual Representation of the intersecting elements identification, from [17].*

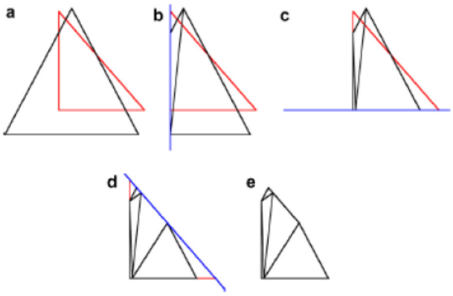

Figure 3.14: *Intersections identification for overlapping area evaluation, from [17].*

eq. (3.6), the flow field values are interpolated on the non-conformal interface.

Chapter 4

Computational Mesh Generation

In order for the Navier-Stokes equations to be solved, the domain should be split into discrete geometrical entities, known as cells. This is the result of the Mesh Generation Process, which stands as a research topic on its own among the CFD world. The process of generating a mesh for the needs of the SM method and also for the investigation of the treaded tire impact, is a vital part of this work.

4.1 Two Mesh Generation Methods

A large variety of Mesh Generation software are available. These can be distinguished based on the method each uses in order go generate the mesh. The first method (Method A) starts with a background mesh, which is then fitted (wrapped) on the surfaces of the domain. This is the method used by *SnappyHexMesh*, available in the main *OpenFOAM*© distribution. This meshing method along with the above mentioned meshing software was used in [4] resulting in robustness concerns for SM compatible meshes. The second method (Method B) starts with the generation of a surface mesh, which is, then, used to fill the volume with 3D cells. However, as shown in section 4.2.1, this method requires increased surface preparation effort.

4.1.1 Mesh Generation Method A

The meshing procedure starts with a volume mesh, referred to as Background Mesh, which then, through a series of steps, is modified in order to respect the given geometry. In Fig. 4.1 the process of generating the mesh through this series of steps is described, for a given surface of a car (in .STL format). The result of these steps is the creation of the volume mesh around the car where the liquid (air) resides.

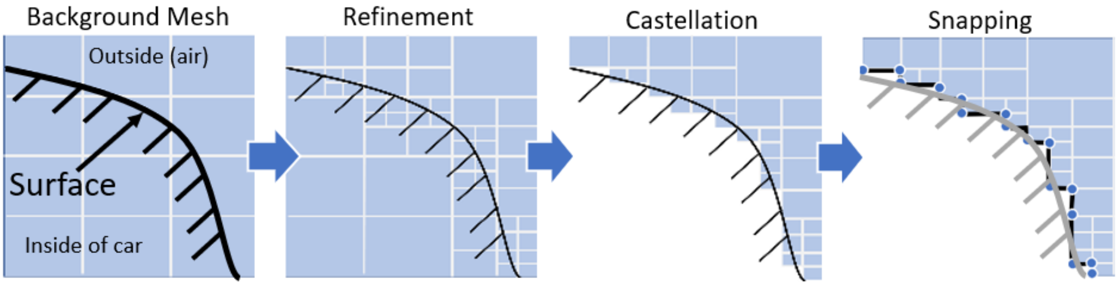

Figure 4.1: *Visual Representation of the mesh generation process (Method A).*

The first step is the generation of a background mesh which does not respect the geometry of the surface, meaning that the surface itself intersects with the cells of the background mesh. The size of the cells for the background mesh, referred to as $Base$, is selected in this step and plays a vital part in the dimensions of the faces on the given surface.

For the second step, the cells that intersect the given geometry are split into equal parts, increasing the resolution of the mesh in the proximity of the surface. The result of this process, referred to as refinement, will be the size of the faces on the given surface. The user can control the resolution of the surface, by adjusting the number of times the background cells will be split, referred to as $Refinement\ Level$,

$$Size = \frac{Base}{2^n} \tag{4.1}$$

where $Size$ is the resulting size of the faces on the surface, $Base$ is the size of the cells of the background mesh and n is the $Refinement\ Level$ that corresponds to the number of times the background cells will be split.

The third step of the process is the removal of the cells that reside in the part of the domain where the liquid (air) does not exist. In the case of a car, that can be the inside of the car's passenger cabin. The distinction between the part of the domain to be kept and the part to be deleted is achieved through the selection of the seed point that resides in the liquid part of the domain. This process is referred as $Castellation$ in the $SnappyHexMesh$ vocabulary [19].

The fourth step is the placement of the nodes of the mesh on the given surface, so that this surface be accurately represented in the mesh. This process is referred to as *Snapping*. After the snapping process finishes, layers can be added next to the surface.

This approach is commonly used for big assemblies (such as the surfaces of the car) since it does not require any special treatment of the surface which is imported to the Meshing Software. Therefore, the generation of the mesh will be successful even if there are flaws present on the surfaces (gaps, self intersections etc.), keeping the preparation of the surfaces at low cost (expressed in man-hours).

However this method cannot always achieve accurate results as was observed in [4]. The reason is that the placement of the nodes is the end result of the snapping process which is not always successful on placing the nodes on the surface accurately. Therefore, in order to achieve accurate representation of a surface, depending on the complexity of the geometry, an increase in refinement is necessary, so that the resolution of the mesh becomes adequate (4.1). This increase, in refinement, however, causes an increase in the cost of the simulation [4].

4.1.2 Mesh Generation Method B

The second method prioritizes the quality of the surface mesh, by starting with the generation of a surface mesh which is then extruded towards the rest of the domain to create the volume mesh. This method requires an increased surface preparation effort and therefore is not commonly used in big assemblies (eg. a car). However, this method can ensure the correct representation of the surface and give the user control over the size of the faces on the surface. A visual representation of the method is given in Fig. 4.2.

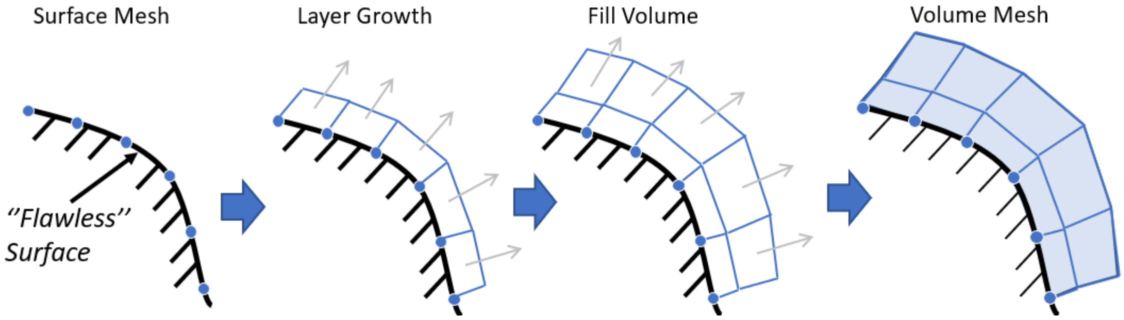

Figure 4.2: *Visual Representation of the mesh generation process (Method B).*

The first step of this method is to create a surface mesh by placing the nodes directly on the surface. This is a key advantage of the method since it guarantees that the resulting mesh will be correctly fitted on the given surface, and also the resolution of the mesh on the surface can be controlled accurately. However, as it is stated in Fig. 4.2, the surface that is imported to the meshing software (in the form of an .STL surface), has to be "flawless", meaning that no gaps or self intersections are allowed. The domain to be meshed has to be completely watertight in order for the mesh generation to succeed. This increases the modelling effort to prepare the surfaces accordingly.

The second step is the growing of layers starting from the surface mesh and towards the liquid part of the domain (in the direction of the arrows in Fig. 4.2) which is again designated using a seed point.

After the layers have been added, the meshing software then extrudes the cells outwards w.r.t. the surface in order to fill the rest of the domain with cells. The end result is a volume mesh, that has been generated based on the surface mesh created in the first step of the process. This way, the placement of the nodes is prioritized and the nodes are accurately placed on the surface, without the need to increase the resolution of the mesh in this area.

This process can achieve accurate results. However, it comes with an increase in the modelling effort. The full surface of the car, is described by hundreds of smaller surfaces, one for each part. The effort required to fill all the small gaps and delete all self-intersecting elements between these surfaces, so that the "Flawless" surface can be produced, is immense (4-5 weeks), compared to the modeling effort for method A (4-5 days), where self-intersections and small gaps are allowed.

On the other hand, the gains in mesh quality are important. In areas where the correct representation of the surface is important, method B can overcome the difficulties opposed by the challenging geometries (like the ones in Fig. 3.2) and produce meshes that describe in full detail the geometry, without increasing the resolution of the mesh.

In Section 4.2, the complete approach for generating the mesh for the Sliding Mesh method (Section 3.3.3) is presented, where both A and B mesh generation methods are used, focusing on the advantages of each one.

4.2 Mesh Generation for SM Simulations

In this section, the process of generating the mesh for the Sliding Mesh simulation is explained, using both A and B mesh generation methods. The technique focuses on overcoming the difficulties that were raised from the work in [4], where method A was solely used. The main problem being the robustness of the mesh generation process, meaning that the current method used could not guarantee the successful generation of the mesh for every given geometry.

4.2.1 Geometry Preparation

The first step for the mesh generation process is the preparation of the surfaces that are then used by the meshing software. In this work, the ANSA [31] pre-processor is used, in order to prepare the surfaces for the meshing process. The license for the use of this software was provided by TME. When the Sliding Mesh method is used for the simulation of the rotation of the wheels, the Geometry Preparation should include the creation of the surface that separates the rotating from the stationary domain. This surface, referred to as $AMI\ Surface$, is presented in a two-dimensional (2D) manner in Fig. 4.3.

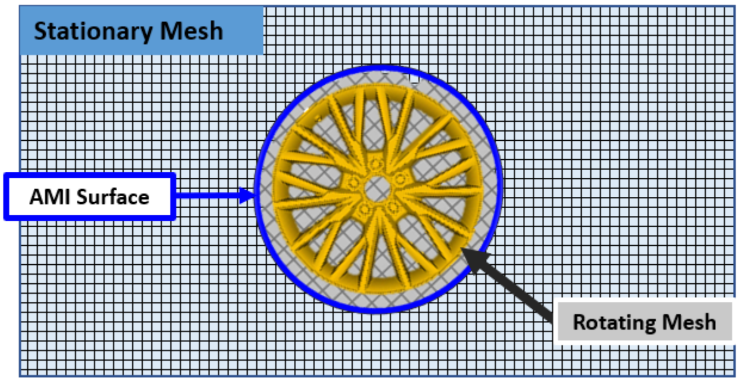

Figure 4.3: *Two Dimensional representation of the AMI surface.*

The surface represented in Fig. 4.3 with blue colour, is responsible for separating the Stationary from the Rotating domain of the mesh. Since the AMI Surface acts as the boundary of the rotating domain, its shape should be strictly axi-symmetric, and the symmetry axis should coincide with the axis of rotation for each wheel. The placement of the AMI Surface should be such, so that the components that will be rotating during the simulation are placed inside of the rotating domain, indicated by the surface. In this work, the AMI Surface is such so that the spokes are encased inside the rotating domain, whereas the rest of the rotating parts (tire and rim) will be simulated using properly imposed boundary conditions (Section 3.3).

Figure 4.3 gives a 2D representation of the surface, therefore the surface is represented by a circle. In the 3D space, the AMI surface, is an axi-symmetric 3D surface. The geometry of this surface is complicated since it should include the rotating components (the spokes) and not include the stationary components (the brake caliper). These two components are presented in Fig. 4.4, along with the generated AMI Surface shown in blue colour. The two components shown are the two most influential components when it comes to the geometry of the generated AMI Surface (Appendix 7).

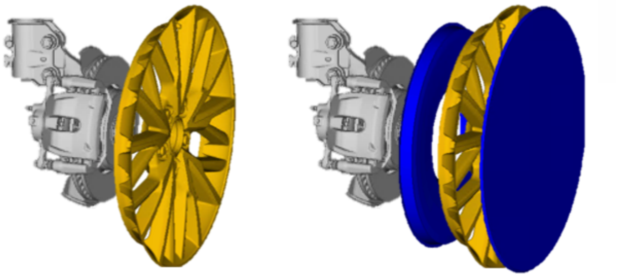

Figure 4.4: *Three-dimensional representation of the AMI surface (blue) around the spokes (yellow).*

In order for the Rotating Domain to be separated, the AMI Surface should be the boundary of a sealed, watertight volume which includes the spokes. By adding the rest of the Wheel Assembly components (presented in Fig. 3.2) the Rotating Domain is sealed from the Stationary. A section view of the Wheel Assembly including the generated AMI Surface is presented in Fig. 4.5.

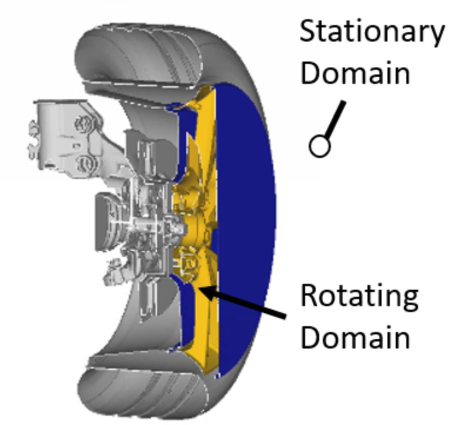

Figure 4.5: *Complete Wheel Assembly, distinction of the Stationary from the Rotating Domain (Blue: AMI surface, Yellow: Wheel spokes).*

Although the surface can be created manually, for this work, a Python-Script is used in order to create the Surface automatically in the ANSA environment. The automation of the AMI Surface generation process is a vital step that not only increases the durability and robustness of the process, but it also reduces the modelling effort for the surface preparation. However, the meshing process should confirm that the automatically generated surface does not undermine the mesh quality.

After the AMI Surface has been generated, the domain has been successfully split into two. The first one being the Stationary domain, including the majority of the surfaces of the car. The second is the Rotating domain, which (as shown in Fig. 4.5) includes the Spokes of the vehicle. As already stated, in this work a new technique is applied that combines both A and B mesh generation Methods.

In detail, **Method A** is used in order to generate the mesh for the Stationary Domain, whereas **Method B** is used in order to mesh the rotating part of the domain. This two-step mesh generation requires different handling of the surfaces since the geometry should be prepared once for the meshing of the stationary domain, and four times (one for each wheel) for the meshing of the Rotating domain.

For the Stationary part of the domain, the surface preparation process is limited to filling the gaps that are larger than the minimum cell size, designated by (4.1) for a given Refinement Level. Apart from this, the surface is allowed to have small gaps and/or self intersecting elements. Therefore, the modelling effort remains low, since Method A is applied for the majority of the car's surfaces, as shown in fig. 4.6.

On the other hand, Method B is used in order to generate the rotating part of the mesh. As already explained in section 4.1.2, the surfaces used to generate the mesh

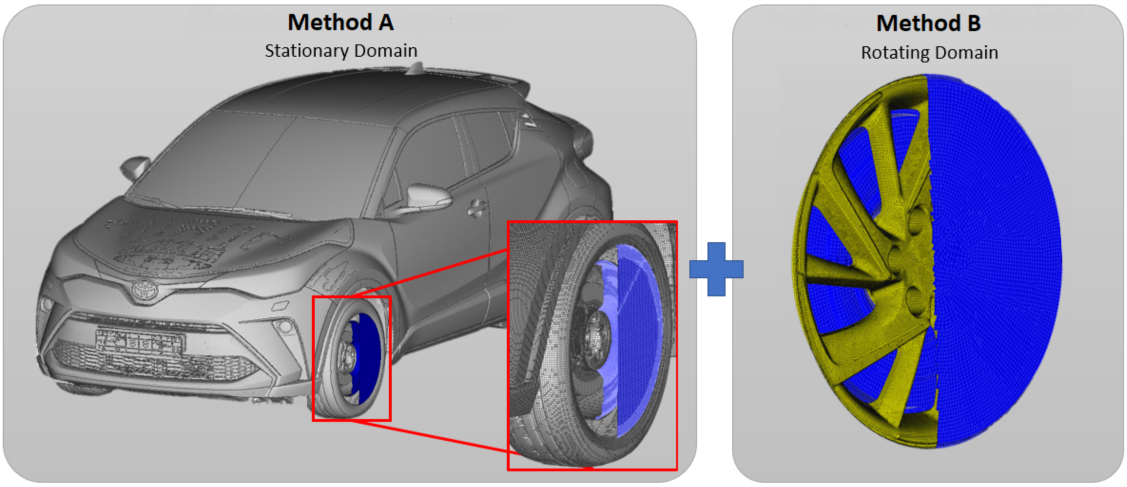

Figure 4.6: *Stationary Domain: Method A — Rotating Domain: Method B.*

with this method should be "flawless", meaning no gaps or self-intersecting elements are allowed. Therefore, an increased modelling effort arises for the preparation of the surfaces for the Rotating domain mesh generation. However, because it is only used locally for the domain specified by the AMI surface and the spokes (right side of Fig. 4.6), the total cost of the workflow remains low (expressed in man-hours).

4.2.2 Mesh Generation

In order to account for both methods, the use of one mesh generation software is not enough. In [4], *SnappyHexMesh*, a mesh generation software which can support only Method A, is used for the mesh generation. However, the success of the mesh generation process was shown to be highly dependent not only on the Spokes Design, but also on the geometry of the AMI surface. Therefore, the robustness of this process did not comply with the needs of the fast paced industry.

In order to account for the new meshing technique, tools that comply with method B must be used. Although there is a wide variety of meshing software for both A and B methods, in this work, *Hexpress/Hybrid* is used for the generation of the stationary domain, using Method A. For the generation of the Rotating domain, $OMNIS^{TM}$ is used, which can use method B. Both *Hexpress/Hybrid* and $OMNIS^{TM}$ [32] are distributed by *NUMECA*©. The licenses for the use of these software was provided by TME, during the six-month internship.

The new two-step meshing strategy was proposed as an alternative to the previous single-step approach used in [4], so that the robustness of the meshing process would increase. In detail, the meshing process would suffer (Fig. 4.8) in the handling of the triple intersection, that is the intersection of the AMI surface, the tire and the spokes, presented in Fig. 4.7. Therefore, the meshing process proposed in this work should validate its ability to handle the triple intersection area.

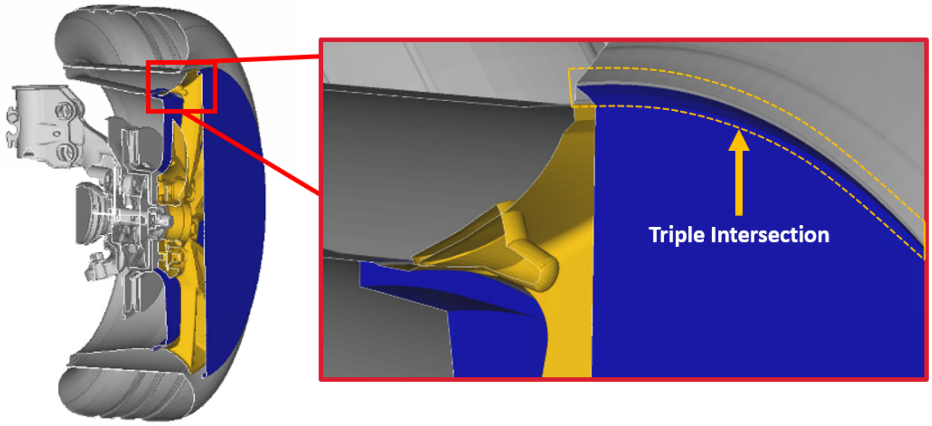

Figure 4.7: *Triple Intersection involving the AMI surface, the tire and the spokes.*

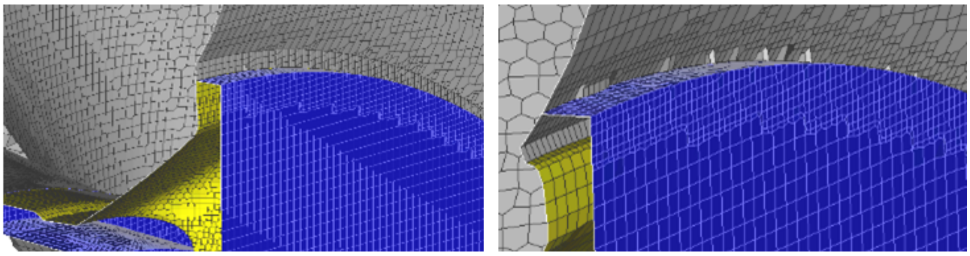

Figure 4.8: *Correct (left) and incorrect (right) representation of the triple intersection on the mesh [from [4]].*

The correct representation of the triple intersection is vital for the accuracy of the simulation results. In cases where the triple intersection is not displayed properly (eg. the right side of Fig. 4.8), the simulation will crash. The reason is that the triple intersection involves the AMI surface, which if depicted poorly on the mesh, will affect the weights of the AMI interpolation (AMI weights) explained in section 3.3.3.2, affecting the communication of the rotating and stationary domains.

The two step meshing technique proposed in this work, is visually presented in Fig. 4.9, where a section view of a wheel assembly is presented.

On the left side of Fig. 4.9, the stationary domain to be meshed is represented by the crosshatched area. The key point of this technique is that the spokes are not included in the meshing of the stationary domain, since the AMI surface is used as a boundary for the mesh generation process. Therefore, from the mesh generation software point of view, the spokes do not exist, when it comes to meshing the designated area. This way, the triple intersection area is no longer the intersection of three surfaces, but now consists of the intersection between the AMI surface and the outer part of the tire. As a result, the meshing software is not forced to place

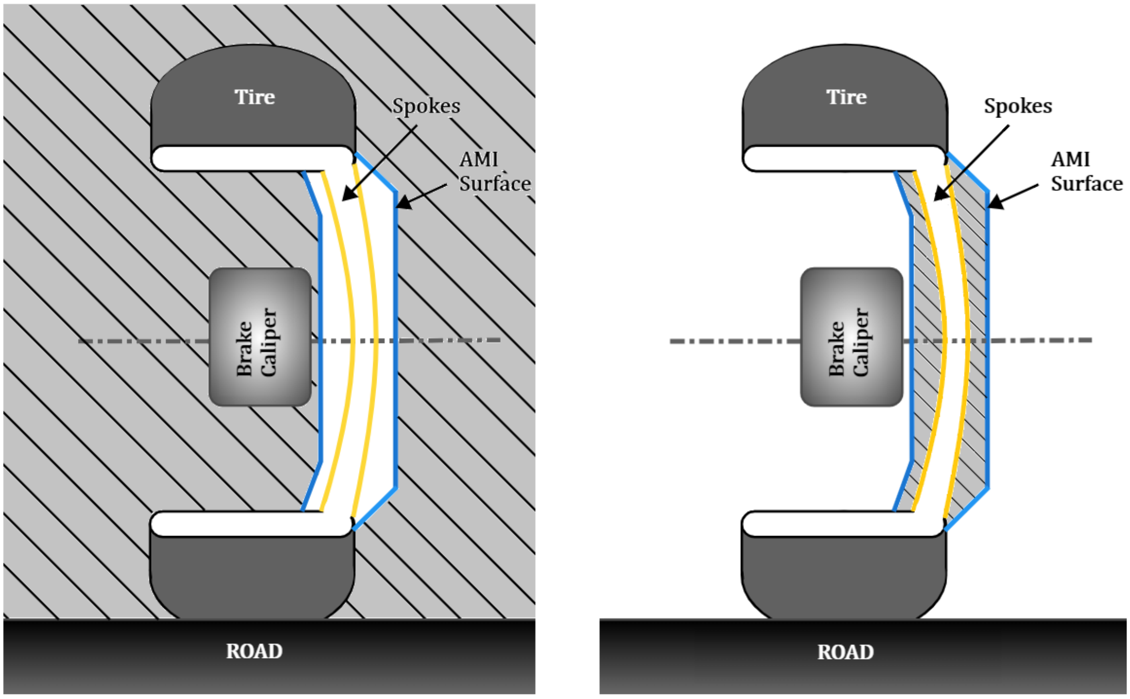

Figure 4.9: *Cross-Section of the wheel assembly for the Stationary domain mesh (left) and the Rotating domain mesh (right).*

cells on both sides of the AMI surface, since the domain inside the surface is not meshed. This way the triple intersection area is easier for the meshing software to handle, even when method A is used.

On the right side of Fig. 4.9, the rotating domain to be meshed is presented by the crosshatched area. This area is meshed using Method B. Therefore, because of the method's ability to accurately place the nodes of the generated cells on the surface, the mesh quality is ensured, and the characteristic sizes of the mesh can be controlled, without a drop in mesh quality.

A visual representation of the complete method, in the form of a flow chart, is presented in Fig. 4.10.

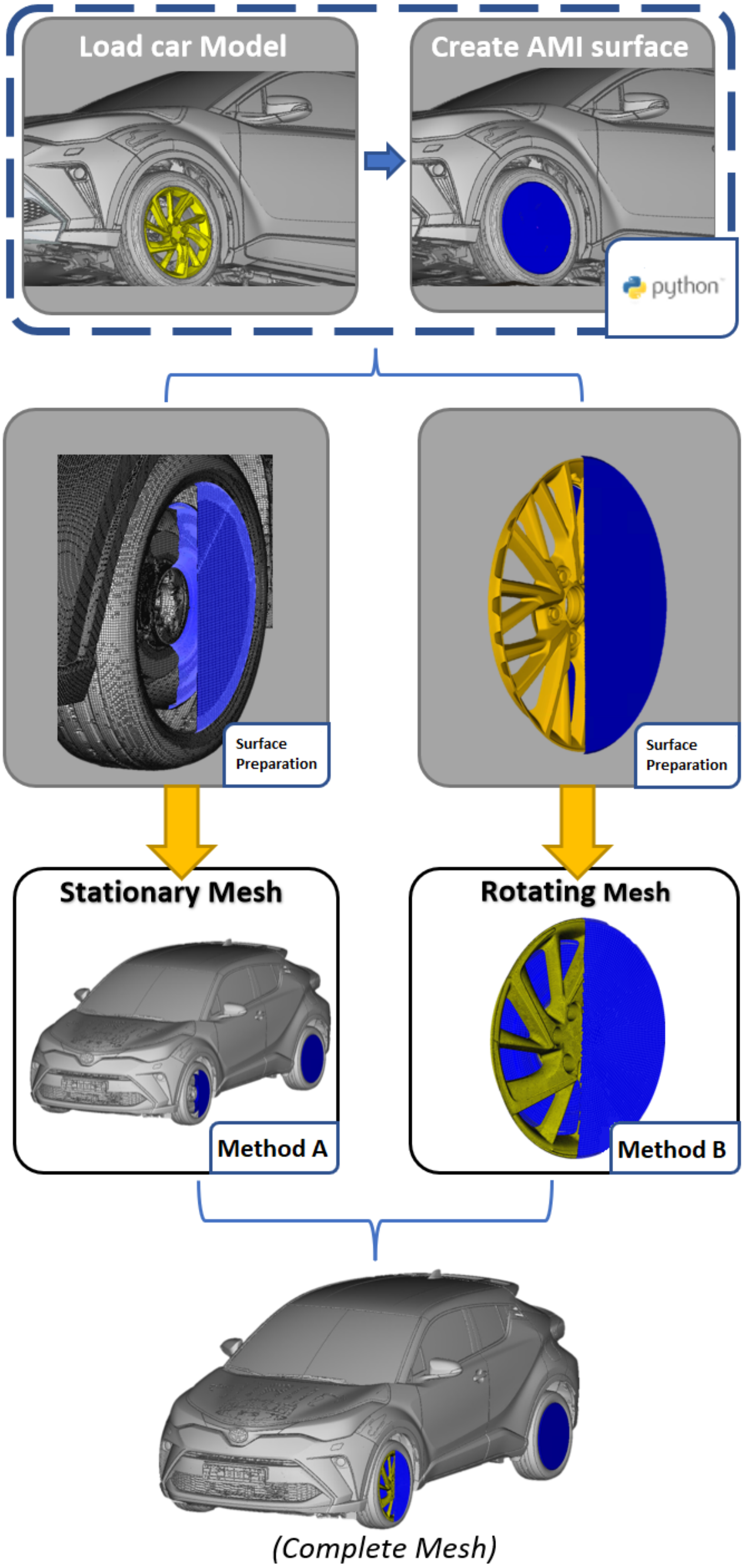

Figure 4.10: *Flow chart of the Mesh Generation Process (Method A: Wrapping , Method B: Surface mesh first).*

Fig. 4.10 shows the complete workflow for the mesh generation process, starting from the import of the raw CAD surfaces and ending with the complete mesh describing both the Stationary and Rotating domains. The total cost of the process is 5 hours per wheel setup (expressed in man-hours). One the keys in the cost (expressed in man-hours) reduction is the automation of the AMI surface, using a python-script. Furthermore, the new two step meshing technique can provide the necessary robustness so that the mesh generation process is successful even when using the automatically generated AMI surface.

The new technique was tested in four different wheel set-ups presented in Fig. 4.11.

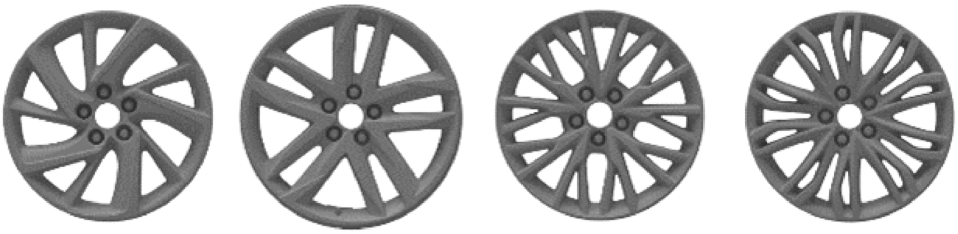

Figure 4.11: *Four different Spokes Designs successfully meshed.*

The result is a correct representation of the triple intersection in four out of four wheels the technique was tested on. Figure 4.12 shows the mesh generated at the most challenging triple intersection area for one of the setups. As shown on the figure, the technique provides a good representation of the triple intersection area, since the meshing software can accurately align the nodes. Therefore, the robustness of the meshing process is validated.

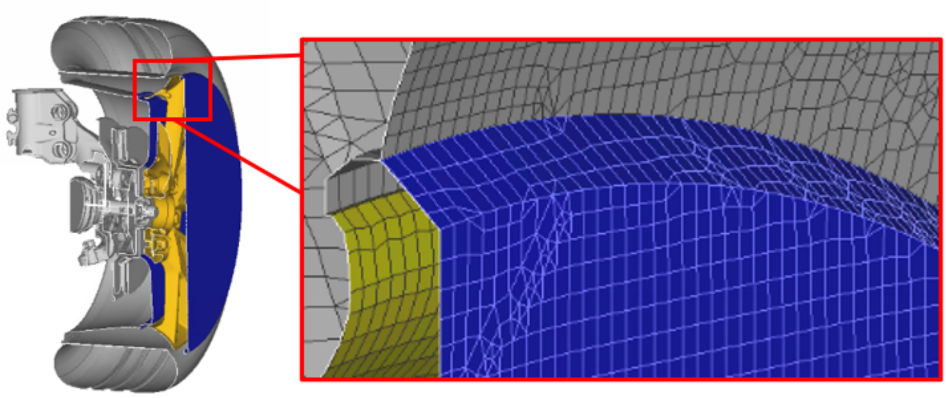

Figure 4.12: *Correct representation of the triple intersection area.*

The mesh is generated for the domain shown in Fig. 2.4. The goal is to imitate the WT Setup. The domain's dimensions can be seen in Fig. 2.4 along with the relative position of the car, giving a sense of the area the mesh generation software has to fill with cells. In Table 4.1 the characteristic values of the mesh are presented. The complete mesh generation process (for both stationary and rotating domains using *Hexpress/Hybrid* and $OMNIS^{TM}$ respectively) takes roughly 3 hours running in parallel in 8 cores. This is a computational cost that has to be taken into consideration from an industrial point of view.

Mesh Stats	
Total Cells	100M
Stationary Dom. Cells	96M
Rotating Dom. Cells	1M (x4 wheels)
Dominant Cell Shape	Hexahedron
AMI Faces/Wheel	110K
Number of Layers	3
Computational Cost	24 CPUh (3 hr in 8 CPUs)

Table 4.1: *Generated Mesh Stats for full car mesh.*

4.2.3 Boundary Conditions on the wheel

In Fig. 4.13, the surfaces of the car are presented in order to highlight the ones where extra BCs, than the ones presented in Table 2.1, are used.

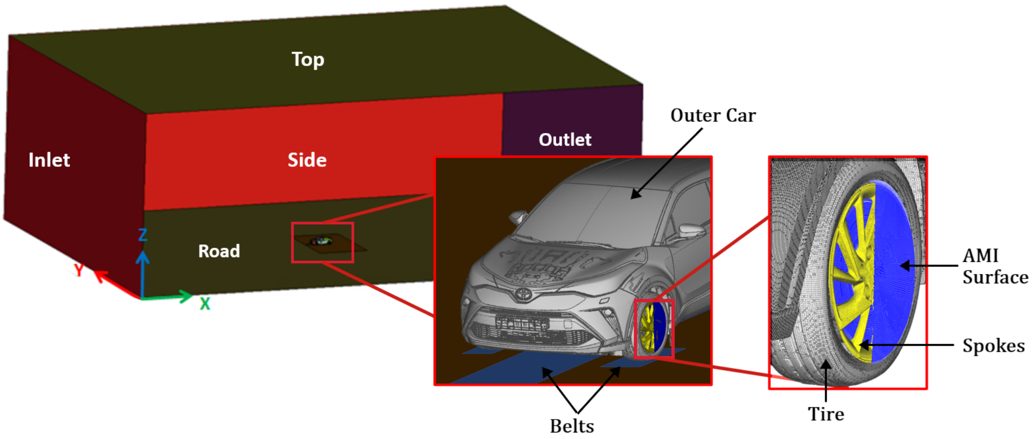

Figure 4.13: *Distinction of the surfaces of the wheel assembly.*

The BC for the two full-car simulations are presented, using the SM and the RWBC for modeling the rotation of the spokes. The latter is referred to as TV simulation. The MRF approach for the simulation of the spokes rotation is not tested since the work in [4] proved that the method suffers greatly in terms of accuracy. For the TV simulation, the AMI surface is not included and the RWBC is used in order to simulate the rotation of the spokes.

For the Sliding Mesh simulation, the *cyclicAMI* BC is used on the AMI surfaces so that the communication of the Stationary and Rotating domains can take place (Sections 3.3.3.1 & 3.3.3.2). Since the tire used for this simulation is Grooved, the RWBC can be used without any errors.

Boundary Conditions		
Variable:	Velocity	Pressure
Outer Car	No Slip	Zero Neumann
Tire	RWBC	Zero Neumann
Spokes (SM)	*movingWallVelocity*	Zero Neumann
Spokes (TV)	RWBC	Zero Neumann
AMI Surface	*cyclicAMI*	*cyclicAMI*

Table 4.2: *Boundary conditions used for the SM and TV simulations.*

4.2.4 Number of AMI faces

Highlighted in light gray in Table 4.1, the AMI Faces per wheel is a very important statistic for the SM simulation, since it directly affects the simulation cost of the process.

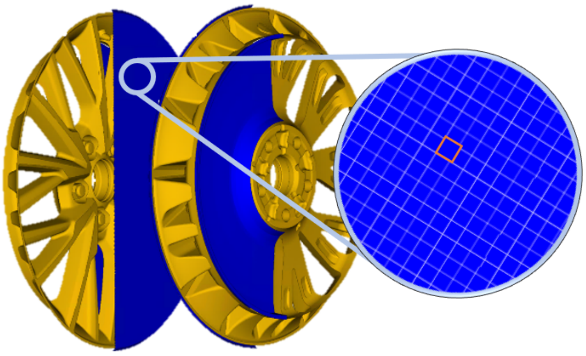

Figure 4.14: *The faces composing the AMI Surface on the mesh (AMI faces).*

AMI faces, refers to the number of faces that the AMI surface mesh is composed of, after the mesh generation process has been completed (Fig. 4.14).

Using the new technique that combines both the A and B mesh generation methods, the representation of the triple intersection is correct. At the same time the sizes of the faces used on the AMI surface is increased (w.r.t. the work presented in [4]), therefore making the surface mesh coarser and leading to a lower number of faces on the AMI surface 4.15.

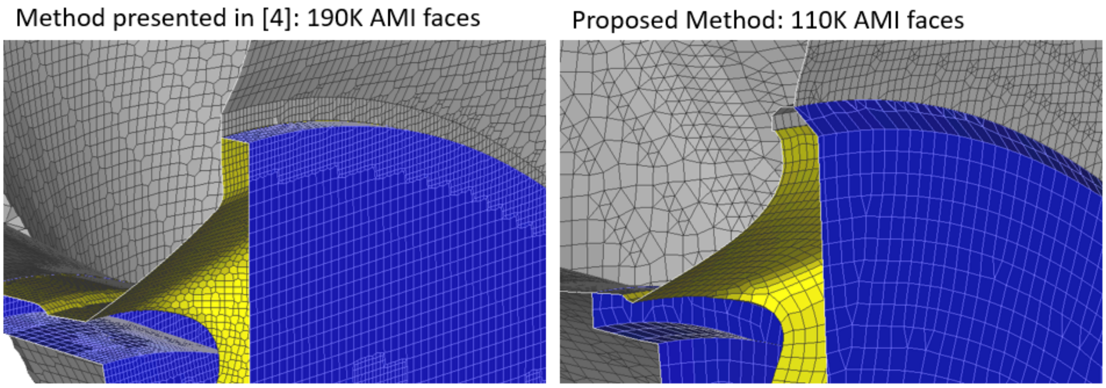

Figure 4.15: *The faces composing the AMI Surface on the mesh (AMI faces).*

The relation of the SM simulation cost with the number of AMI faces, has already been stated in [4] and is again validated in the scope of this work (Section 5.1.3). In general, a decrease in the number of faces results in a decrease in simulation cost.

The limitations of reducing the number of AMI faces even more, along with the development of a new approach for overcoming these limitations, is presented in Appendix (7). This approach, referred to as Hybrid Approach 7.3, uses two different treatments for the surfaces used in the meshing process.

4.3 Mesh Generation for Treaded Tire

In this section the process of creating the mesh for the treaded tire investigation is presented. The goal is to generate a mesh that includes the treads of the tire. After the mesh is generated, the goal is to investigate the differences in the flow characteristics and drag force between a grooved and a fully treaded tire shown in Fig. 4.16.

Figure 4.16: *Grooved Tire geometry (left) and fully treaded tire geometry (right).*

The task of generating the mesh for the fully treaded tire is a challenging one, since the dimensions of the treads are very close to the dimensions of the cells used on the tire. Furthermore, the domain residing inside of the treads needs to be separated from the rest of the domain, since the MRF condition (Section 3.3.2) will be used for the inside volume of the treads in order to capture the effects of the rotating tire.

The cross-section of each thread (shown in fig. 4.17) can be simplified into a rectangle with a characteristic width and depth. These values differ depending on the tire's type and manufacturer. For the tire under investigation the depth is equal to $6[mm]$ whereas the width is equal to $5[mm]$. These values were measured based on the 3D scan of the tire presented in Fig. 4.19. These dimensions, however, are different when it comes to the tread pattern on the middle area of the tire. In detail, the depth is limited to $1[mm]$ whereas the the width is measured at $1[mm]$. Therefore, generating the mesh for this complex geometry is challenging.

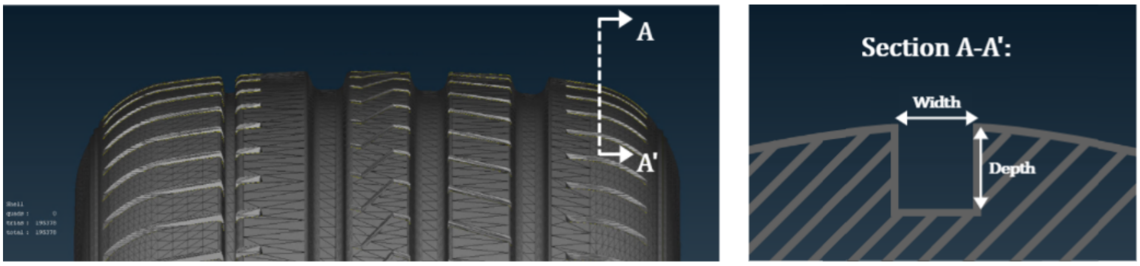

Figure 4.17: *Dimensions of a section of a tread.*

The second step is to separate the domain residing inside each tread so that the MRF condition can be imposed locally to account for the tire's rotation. A cross-section of the domain to be separated is highlighted in red colour in Fig. 4.18. The separation of the domain is succeeded in the mesh generation process.

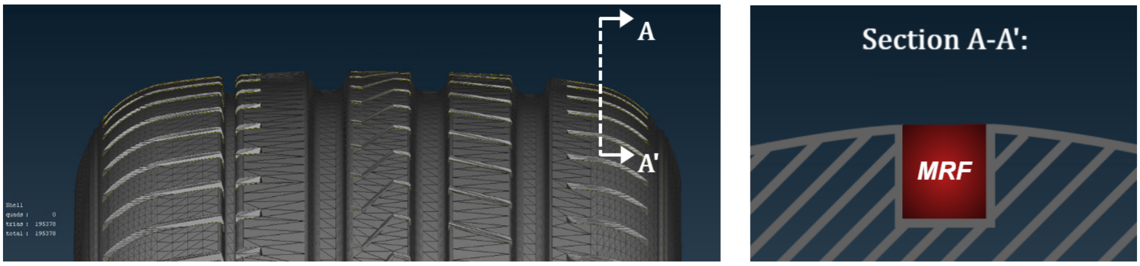

Figure 4.18: *Separation of the domain for the MRF condition.*

The proposed method should be applicable in a wide variety of tires, so that the robustness of the process can be ensured. Furthermore, it should use the same tools as the ones used in the whole car assembly meshing, so that the two could potentially be integrated into one simulation. In this work, the mesh generation process is tested on a commercially available tire.

4.3.1 Geometry Preparation

As is the case for any mesh generation process, the first step is the preparation of the surfaces for the meshing software. Since Method A (section 4.1.2) will be used for the mesh generation, the surfaces do not need to be manually fixed from any flaws, since self intersecting elements and small gaps (smaller than the minimum cell size) are allowed. However, the first challenge for the surface preparation is the generation of the treaded surface itself. Since no CAD data is available from the tire suppliers, the surface has to be generated using other methods.

In order to acquire the geometry of the fully treaded tire, a physical tire is scanned using a 3D scanner. The end result of this process is a point-could, consisting of thousands of points which describe a part of the tire (Fig. 4.19).

Figure 4.19: *Point-Cloud of the 3D-Scanned tire.*

The second step is the creation of a CAD-quality tire surface so that it can be used by the meshing software. For this work the creation of this surface is conducted in the *CATIA* environment [33]. The end result is a CAD-quality surface, that does not include the imperfections of a scan-generated surface while simultaneously achieving high accuracy in the dimensions of the CAD surface (Fig. 4.20).

Figure 4.20: *Surface generated using CAD software.*

Comparing Figures 4.19 and 4.20 the high dimensional accuracy can be noted. Furthermore, the newly generated CAD surface is up to the standards of the mesh generation software, consisting of smooth and continuous surfaces, unlike the point-cloud which consists of discrete points.

The next step is to create the surfaces which are necessary for distinguishing the domain residing inside the treads, as shown in Fig. 4.18. For that purpose, the surfaces shown on the left of Figure 4.21 are generated. These surfaces define a closed volume that describes the inside of the treads, where the MRF condition will be imposed. If the two surfaces presented were overlapped, the result would be a "slick" tire, where only the longitudinal grooves would be depicted, since the treads would have been "filled" with the purple surfaces.

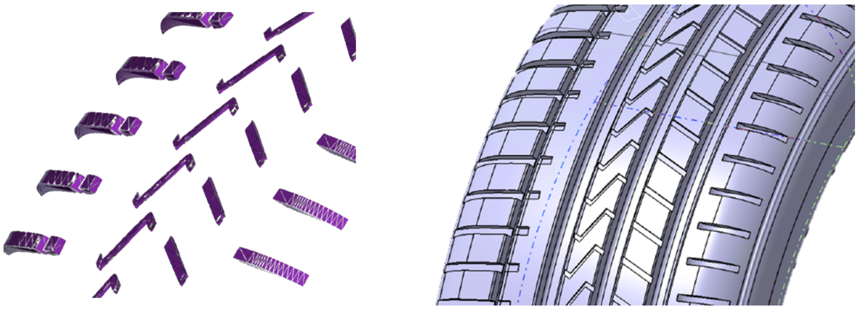

Figure 4.21: *Surface generation for inner tread domain separation (left) , Treaded tire surface (right)*

These surfaces are necessary for the separation of the cells residing inside the treads by the meshing software.

4.3.2 Mesh Generation

Using the surfaces generated in section 4.3.1, the mesh is generated for a single wheel assembly, composed of the tire, the rim, the spokes, the brakes assembly and the driveshaft. The domain for which the mesh is generated along with the position of the wheel is presented in Fig. 13.

The quality of the mesh is highly dependent on the Refinement Level [Eq.(4.1)] selected for the domain inside of the treads (Fig. 4.22). This is expected, since the meshing software can only handle features that are larger than the minimum cell size. Using a Refinement Level of 10, the minimum cell size, calculated using (4.1), is $1.46[mm]$, which is larger than the dimensions of the thin treads located in the middle part of the tire, yet smaller than the treads located on the shoulder area of the tire. Therefore, the representation of the thinner threads is poor whereas the shoulder treads are accurately depicted.

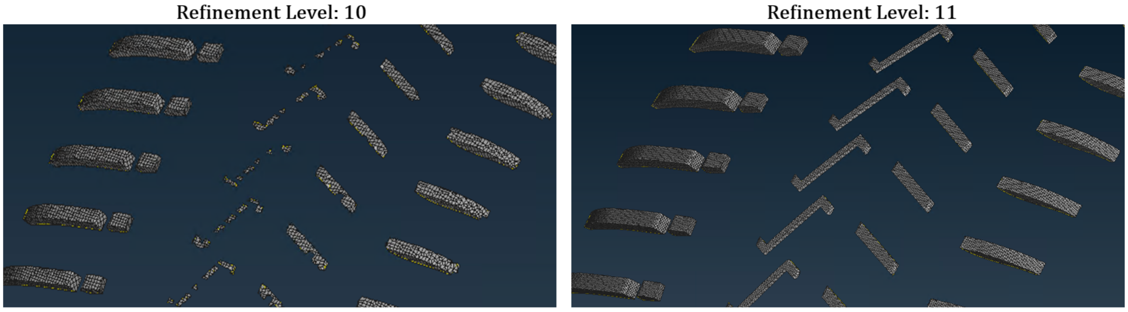

Figure 4.22: *Representation of the tread inner domain relative to the Refinement Level.*

In order to achieve a correct representation of the middle treads the Refinement Level has to be increased to 11, resulting in a minimum cell size of $0.7[mm]$ (right side of Fig. 4.22). However, such a decrease in cell size highly affects the simulation cost of the process, in order for the Courant Number [Equation (4.2)] to remain at acceptable levels. For this work, a Refinement Level of 10 is selected, and the investigation is limited to the impact of the shoulder treads that can be depicted without such a decrease on the cell size. The mesh generated with this technique is compared an identical one that does not include the treads (Grooved Tire of Fig. 4.16) in Fig. 4.23. For both meshes, *Hexpress/Hybrid* is used. The mesh statistics for both the treaded and grooved tires are shown in Table 4.3.

One of the differences between the meshes of Fig. 4.23 is the minimum cell size (directly linked to the maximum Refinement Level). This reduction in cell size is necessary in order to depict the narrow channels on the treaded tire, which are not present on the grooved tire. However, this drop in cell size directly affects the Courant number (4.2) that will be computed during the simulation.

Meshing Approach:	Grooved Tire	Treaded Tire
Total Cells	7.6M	9M
Max. Refinement Level	9	10
Min. Cell Size	3[mm]	1.5[mm]
Number of Faces on Tire	76K	350K

Table 4.3: *Mesh Stats comparison between Grooved Tire and Treaded Tire.*

Grooved Tire Approach (No Treads)

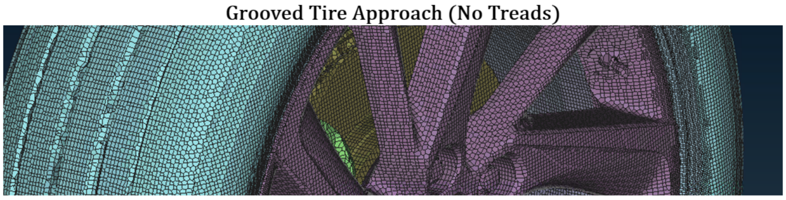

Treaded Tire Approach (only Shoulder Treads)

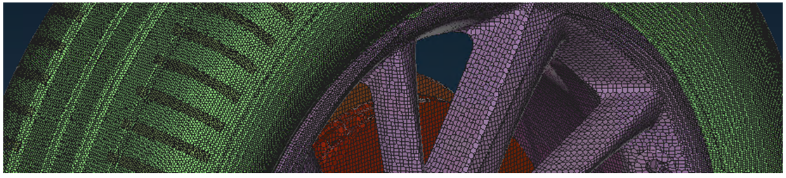

Figure 4.23: *Visual representation of the surface mesh for a grooved (top) and a treaded tire (bottom).*

The Courant Number (Co) is the fraction of the distance the flow travels w.r.t. the cell size,

$$Co = \frac{u\Delta t}{\Delta x} \tag{4.2}$$

where u is the velocity magnitude, Δt is the time-step of the simulation, and Δx is the characteristic length, equal to the cell size (Table 4.3).

Therefore, reducing the cell size by half, has an impact on the Courant Number values. In cases in which Co is high, the simulation will crash. In this work, the time-step is adjusted for the treaded tire mesh in order to account for the increase in Co.

The second main difference is the increase of the faces on the surface of the tire, which is a direct result of the increased refinement level. Together with the increase in total cell count and the reduction in the simulation's time-step, the simulation cost for the treaded tire is expected to increase w.r.t. the grooved tire approach (Chapter 5).

4.3.3 Boundary Conditions on the tire

The boundary conditions for the three simulations are presented in this section. In Fig. 4.24 the surfaces are presented in order for the BC to be correctly imposed.

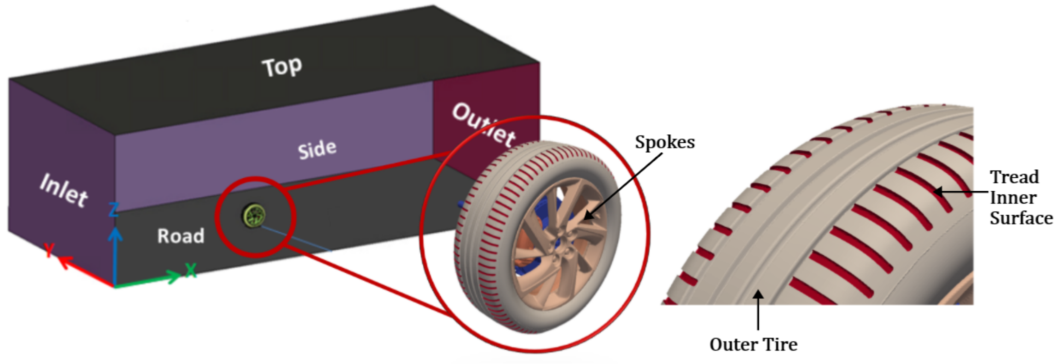

Figure 4.24: *Domain and key surfaces for the Tire Tread Investigation boundary conditions.*

The boundary conditions for the surfaces highlighted in Fig. 4.24 are presented in Table 4.4. The three columns A, B and C correspond to the three different simulations, where the main difference is the BC for the velocity component inside on the Tread Inner Surface (shown in red color in 4.24).

Boundary Conditions				
Variable:	Velocity			Pressure
Simulation	A	B	C	A / B / C
Outer Tire	RWBC			Zero Neumann
Tread Inner Surfaces	-	RWBC	$movingWall$ $Velocity$	Zero Neumann
Spokes	RWBC			Zero Neumann

Table 4.4: *Boundary conditions used for the Tire Tread Investigation simulations.*

For Simulation A, a grooved tire is used where the RWBC is imposed on its surface, since the treads are not present in the mesh. This simulation will serve as a baseline since this is the most common approach for modelling tires.

For Simulation B, a treaded tire is used where the RWBC is imposed on the surface of the tire and on the inner surface of the treads. This approach will be used to investigate the effects of the treads with the RWBC which is known to suffer depending on the surface orientation.

For Simulation C, a treaded tire is used where the RWBC is imposed on the outer part of the tire, and the MRF method is used for the domain inside the treads. When the MRF condition is used, the surfaces residing inside of the domain are "rotating" by default with it. There is no actual movement of the domain, and the rotation effect is succeeded by the introduction of a source term (section 3.3.2). The velocity of the tread surfaces is zero w.r.t. the rotating frame of reference. The implementation in the $OpenFOAM^{©}$ v2106 environment of this BC is the $movingWallVelocity$ BC.

Chapter 5

Simulation Results

In this chapter, the simulation setup and the corresponding results are presented. The chapter is divided into the simulation for the Sliding Mesh and the simulations for the investigation of the impact of the treaded tire. For each simulation, the boundary conditions imposed are explained and the results are, then, commented on.

5.1 Sliding Mesh Simulation Results

This work mainly focuses on the introduction of a more robust method that can accurately generate a mesh for the Sliding Mesh simulation of a moving vehicle. The proposed meshing method (presented in Section 4.2) validated its robustness by meshing accurately four out of four wheels that this method was tested upon (Figure 4.11). However, this work also focuses on the reduction of the simulation cost of the SM method for the rotation of the spokes. In this chapter, the cost and accuracy of the SM method are compared to those of the TV approach.

Focusing on one of the wheel designs of Fig. 4.11, two simulations are presented. The first one is a full-car simulation where the Sliding Mesh (SM) method (Section 3.3.3) is used for the rotation of the spokes, with the mesh generated by the proposed method. The second, is a full-car simulation where the Rotating Wall Boundary Condition (Section 3.3.1) is used for the rotation of the spokes, referred to as Tangential Velocity (TV) approach. These two simulations describe the same car, with the same set of wheels and the Computational Mesh is generated by the same software. The goal is to compare the gains in accuracy of the simulation results and the increase in simulation cost of the process.

5.1.1 TV and SM Results Comparison

In Figures 5.1 and 5.2, the residuals of the governing equations for the unsteady simulation are presented for the Tangential Velocity and Sliding Mesh approaches respectively. In detail, the residuals for the velocity components, the pressure, and the Spalart-Allmaras $\tilde{\nu}$ variable are presented in a logarithmic scaled Y axis.

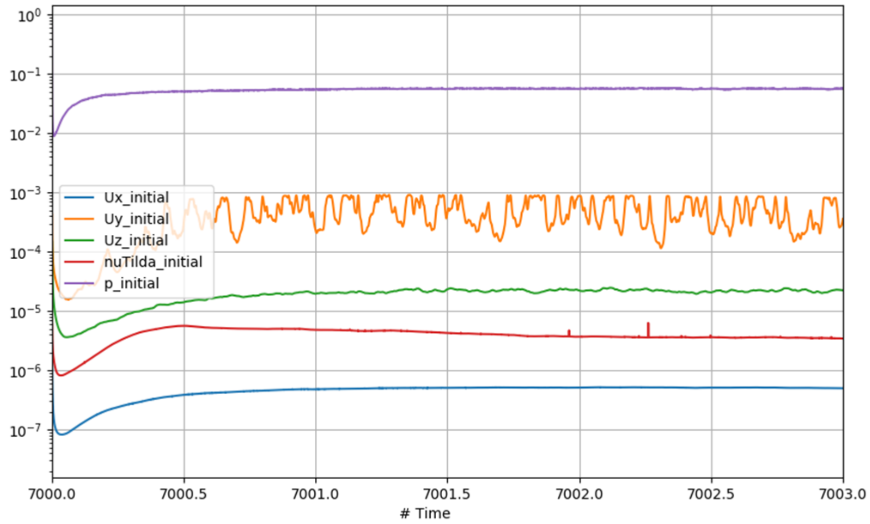

Figure 5.1: *Residuals of the governing equations over simulation time of the transient simulation for the TV method.*

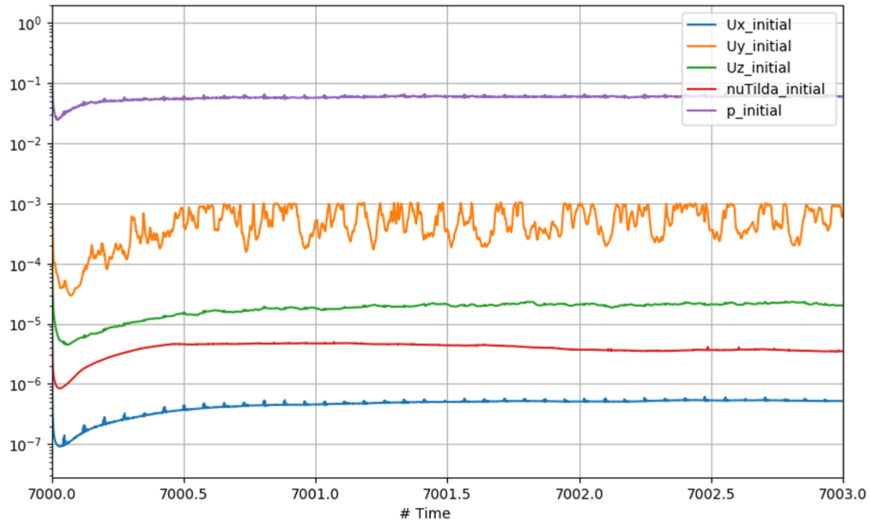

Figure 5.2: *Residuals of the governing equations over simulation time of the transient simulation for the SM method.*

For the visualization of the results, two planes are used, on which the flow field variables are plotted. The first one focuses on the front right wheel. The front wheels have a huge aerodynamic impact since the flow behind the front wheels affects the rest of the car. In Fig. 5.3, the position of the Z-normal plane is presented relative to the car.

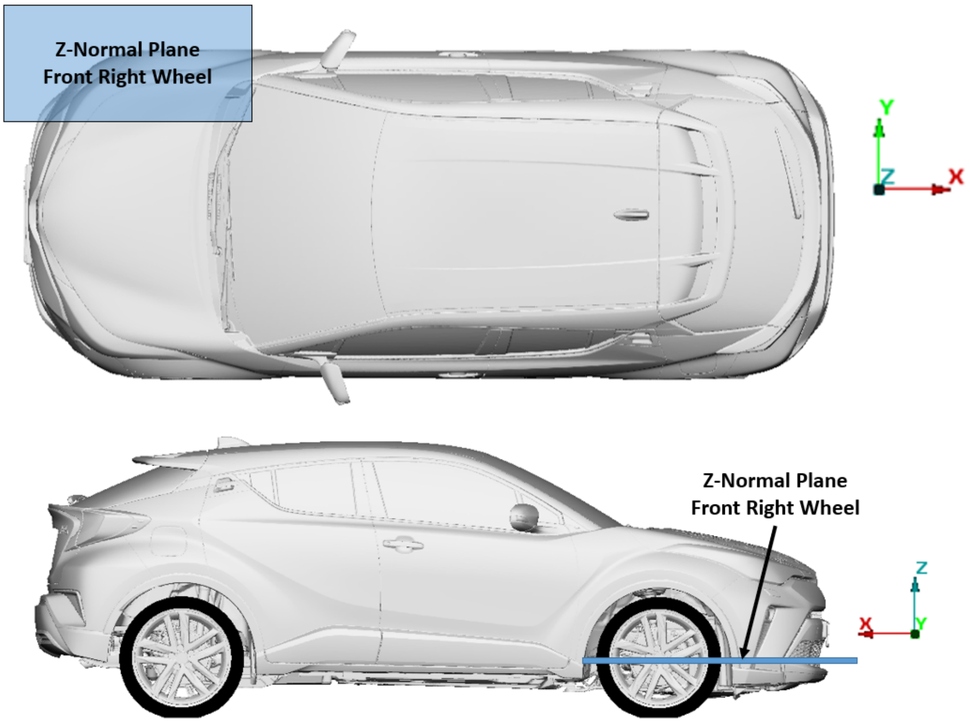

Figure 5.3: *Position of the Z-normal plane relative to the car.*

For the plane in Fig. 5.3, two figures are presented.

In 5.4, the LIC visualisation of the flow field is presented, where the colour indicates the velocity magnitude. The top graph corresponds to the Sliding Mesh simulation, where the spokes are rotating for each time-step. The AMI interface is visible, as the border of the rotating and stationary domains. The bottom part of the graph corresponds to the Tangential Velocity simulation, where the wheels are not rotated. The main difference between these two graphs is noted in the domain close to the spokes, where in general, lower velocities are observed for the SM case. This has also an impact on the wake of the front wheels where it is visible that for the Tangential Velocity the wake is more pronounced further from the car.

In 5.5 the normalized (w.r.t. the far-field velocity) x-velocity is presented where the differences between the two simulations are more pronounced, especially in the area around the spokes. Again, a lower velocity is noted in the proximity of the spokes for the SM case.

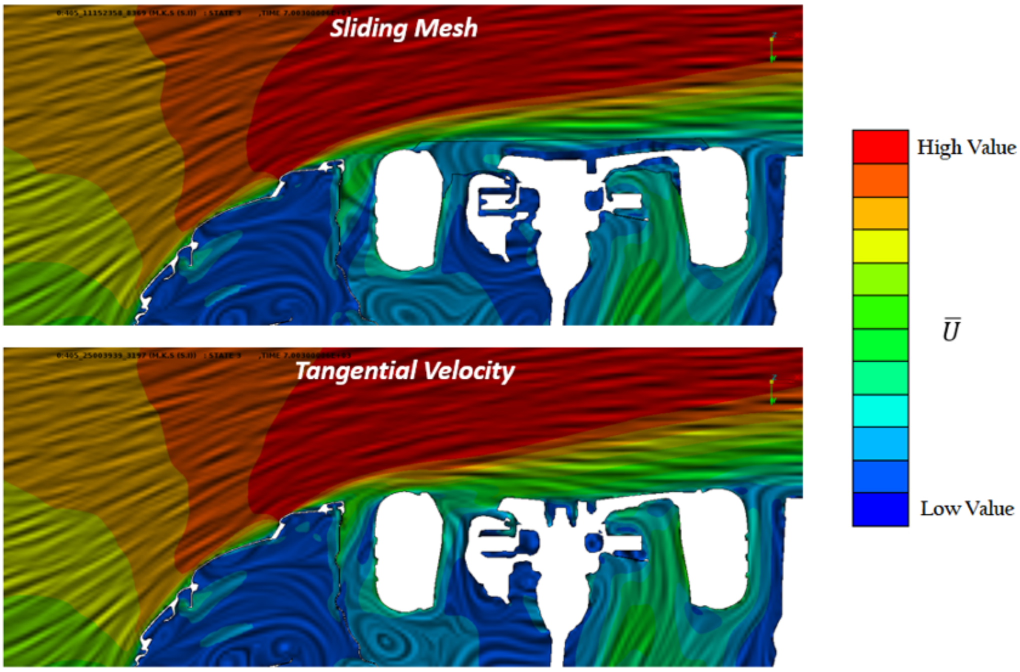

Figure 5.4: *LIC visualization of the flow field with colour indicating the mean velocity magnitude on the Z-normal plane.*

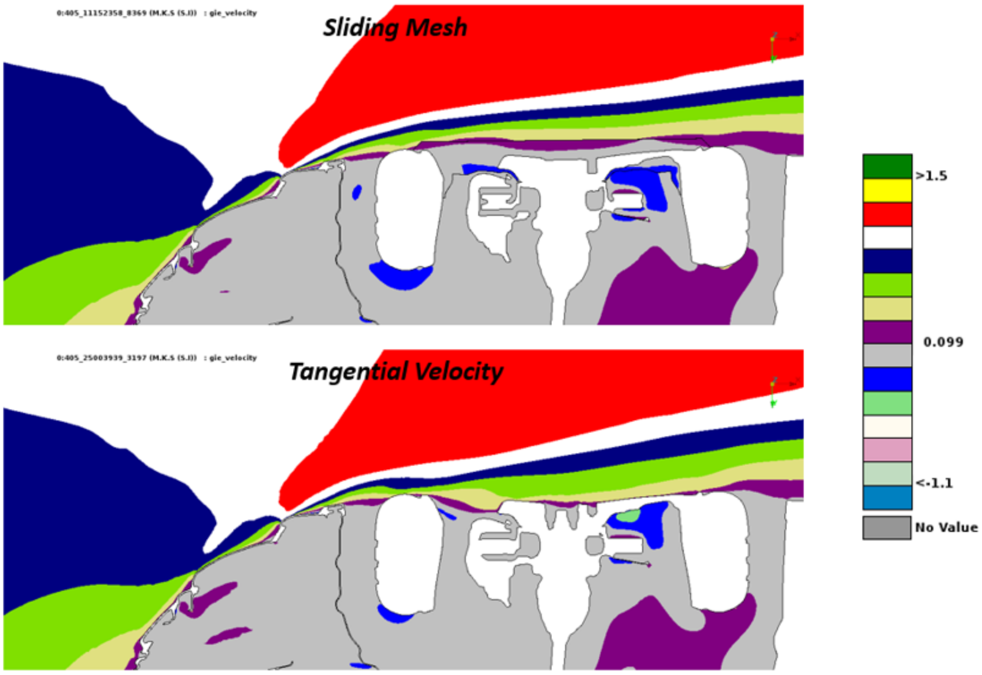

Figure 5.5: *Normalized x-velocity component magnitude contour on the Z-normal plane.*

The second plane also focuses on the front wheels, however this time the orientation of the plane is different, in order to capture the variation of the field values along the X-normal plane. The position of the plane relative to the car is presented in Fig. 5.6.

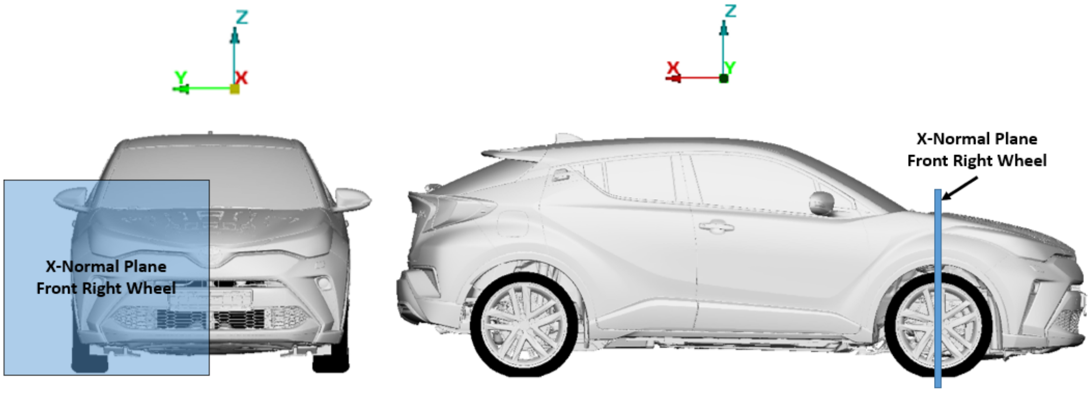

Figure 5.6: *Position of the X-normal plane relative to the car.*

For this plane, two figures are presented, focusing on the area around the wheel, and especially around the spokes, which is the most aerodynamically influential part of the assembly.

In Fig. 5.7, the LIC visualization of the flow field is presented where the colour represents the mean velocity magnitude. Here the difference in the velocity field is more pronounced. The left part of the figure corresponds to the Sliding Mesh simulation. The AMI surface is also visible. The right part of the figure corresponds to the Tangential Velocity simulation where the spokes remain stationary. The first point of interest is the wake generated by the spokes, which has a different shape for the SM and TV simulations. Secondly, the velocities in the proximity of the spokes for the SM simulation (inside of the AMI surface) are lower (colder colour) when compared to the ones on the TV simulation.

In Fig. 5.8 the contour plot of the total pressure coefficient, computed using the mean flow values $\overline{U}, \overline{p}$, is presented. In this contour plot, the characteristics of the flow in the proximity of the wheels is not visible. However this figure focuses on the shape of the wake generated by the front wheels on the left hand side of the spokes for each side. On the SM simulation (left hand side), the wake has a more straight line shape, when compared to the two-lobes shaped wake for the TV simulation. This difference is also visible in Fig. 17.

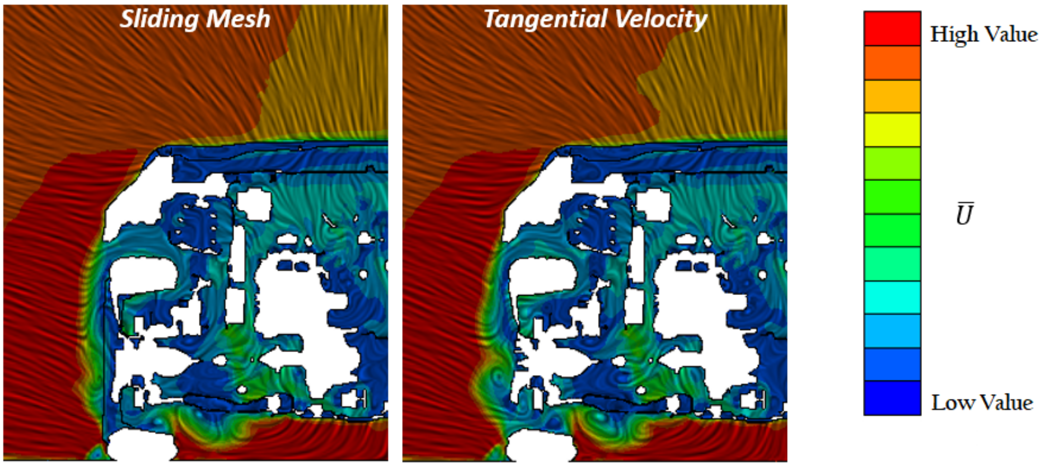

Figure 5.7: *LIC visualization of the flow field with colour indicating the mean velocity magnitude on the X-normal plane.*

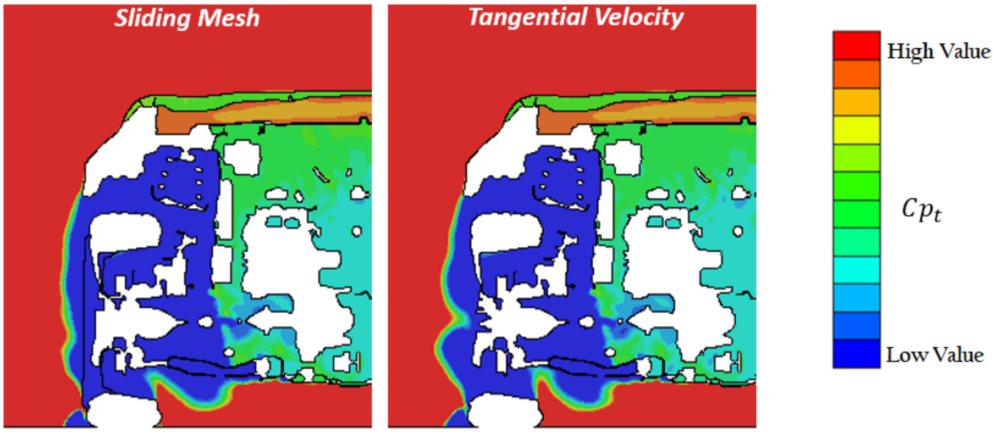

Figure 5.8: *Contour plot of the total pressure coefficient* Cp_t *on the X-plane.*

In Fig. 17 the iso-surface of the total pressure coefficient equal to zero, calculated using the mean flow values $\overline{U}, \overline{p}$, is presented. The top part of the figure corresponds to the Sliding Mesh simulation whereas the bottom part of the figure corresponds to the TV simulation, where the wheels are stationary. The iso-surface is presented as a visualisation tool of the wake generated by the car, and especially the impact of the wheels (and the corresponding simulation option) on this wake's shape.

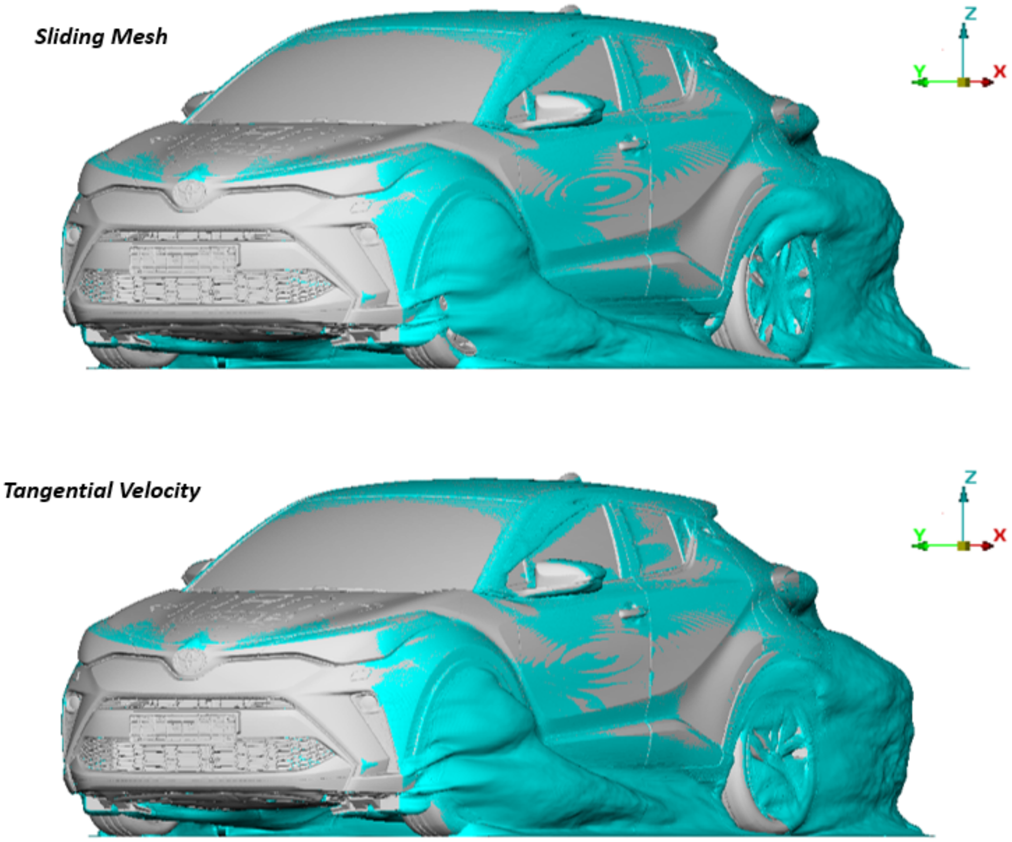

Figure 5.9: *Iso-Surface of the total pressure coefficient Cp_t.*

Starting from the front wheels and towards the tail of the car, the difference in the wake shape and size is noticeable between the two simulations. Around the front wheels, the two-lobes shaped wake is visible for the TV simulation whereas for the SM, a smoother shape is observed. At the middle of the car, the differences are exaggerated, since for the SM method, the surface has the tendency to stick to the floor, whereas for the TV simulation the wake is less spread out towards the floor. Lastly, towards the back of the car, around the rear wheels and through the rear bumper, the difference is also noticeable in the shape of the wake. These differences, spread out around the whole of the car, indicate the deviation between the two simulations on the calculated aerodynamic performance of the vehicle, measured in the form of the drag coefficient (C_D).

In Fig. 5.10 and 5.11, the time history of the normalized instantaneous calculated drag coefficient (C_D) is plotted for the duration of the transient simulation. The values of the two graphs are oscillating between the same values, however for the SM method, the oscillations are pronounced.

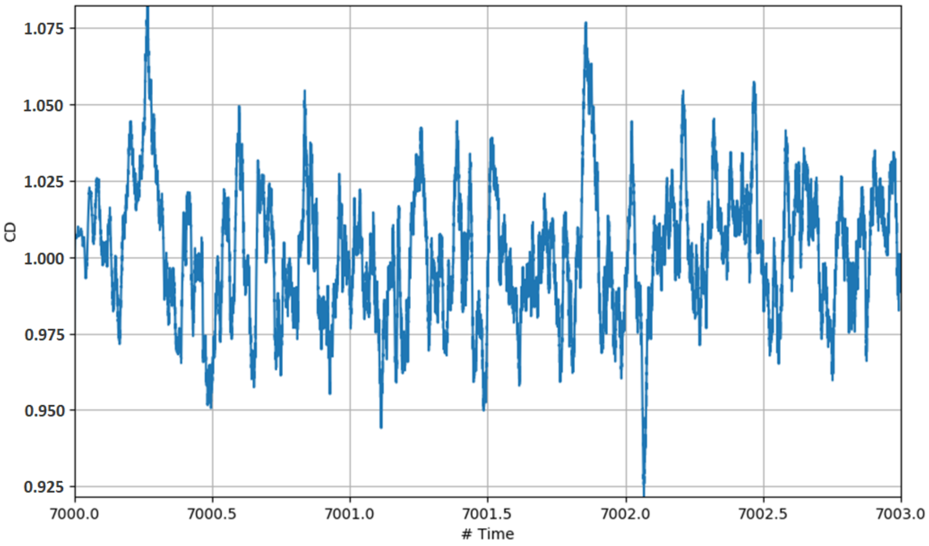

Figure 5.10: *Instantaneous value of the normalized Drag Coefficient for the TV simulation.*

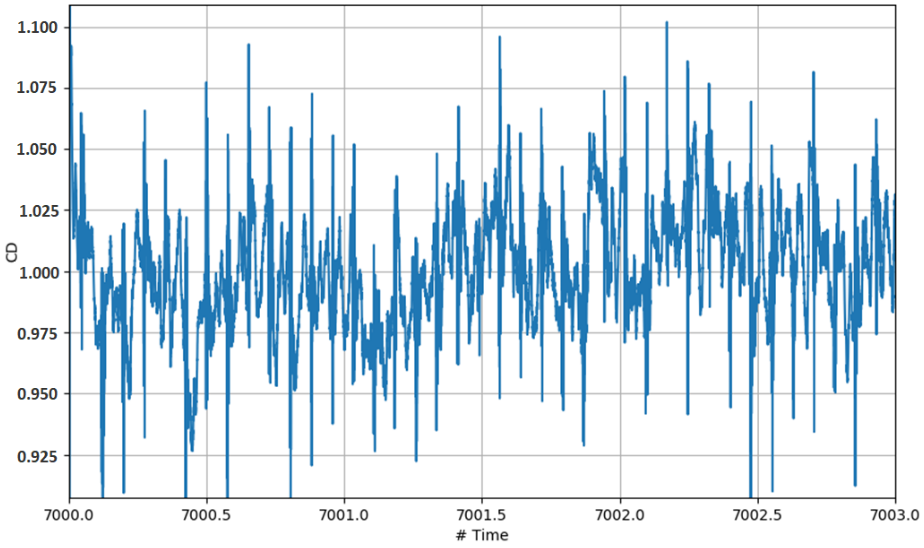

Figure 5.11: *Instantaneous value of the normalized Drag Coefficient for the SM simulation.*

The final value of the normalized drag coefficient, based on which the vehicle will be evaluated, will be the average of the final two seconds of the simulations. These values will be compared with the Wind Tunnel Data, in order to compare the accuracy of the two simulations.

5.1.2 Accuracy comparison

In this section, the accuracy of the results is examined. The accuracy is determined with the comparison of the average normalized Drag Coefficient (C_D) to the value measured at the Wind Tunnel experiment where the same car setup was evaluated. Figure 5.12 shows the absolute value of the deviation from the Wind Tunnel measured C_D value, for the two simulation methods.

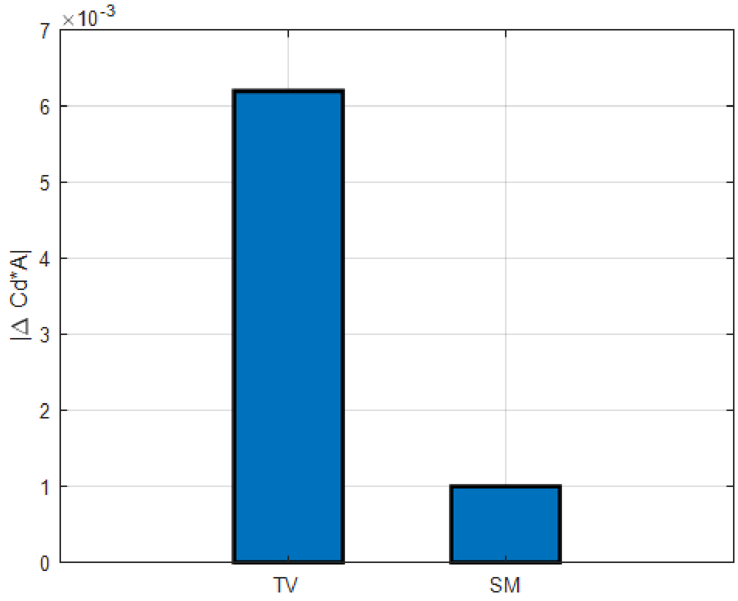

Figure 5.12: *Absolute Deviation from Wind Tunnel value of the normalized Drag Coefficient (TV: Tangential Velocity, SM: Sliding Mesh).*

From Fig. 5.12 the conclusion can be drawn that the Sliding Mesh does a better job at predicting the drag coefficient of the vehicle. This is compliant with the work presented in [4], suggesting that the Sliding Mesh simulation is more accurate in predicting the flow field around the car.

The reason can be traced back to Sections 3.3.1 and 3.3.3. There, the inability of the RWBC to correctly capture the velocity profile of the spokes is showcased. On the other hand, physically rotating the spokes, closely imitates the setup of the WT experiment, where the data for the drag coefficient were acquired.

Figure 5.12 also points out the differences the shape and size of the wake makes on the calculated drag coefficient. Figure 17 does a great job at showcasing the difference of the wheel generated wake, and the wake of the whole car, especially downstream of the rear bumper, which is a highly influential area of the car when it comes to the car's aerodynamic drag (due to the drop in pressure).

However, the two approaches should also be compared w.r.t. their simulation cost, in order for a conclusion to be drawn.

5.1.3 Computational Cost comparison

One of the key points of this work is the reduction of the simulation cost of the Sliding Mesh method. In Fig. 5.13 the simulation cost (calculated in days) of the TV and SM approaches are presented in blue color. The simulation cost of the SM approach, where the mesh was generated with the method presented in [4] is also presented (indicated by the asterisk *).

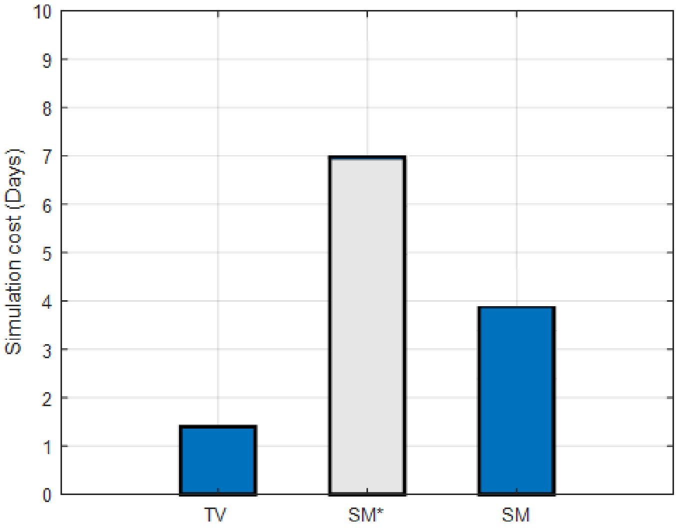

Figure 5.13: *Comparison of the simulation cost (TV: Tangential Velocity, SM: Sliding Mesh using both A & B mesh generation methods for the mesh generation process, SM*:[4], where method A was solely used for the mesh generation process.*

Figure 5.13 indicates that the gains in accuracy (5.12) come with an increase in simulation cost. This increase in simulation cost for the SM approach, when compared to the TV approach, can be appointed to the calculations required in order to rotate the mesh and re-calculate the face-area weights of each face on the AMI Interface (Section 3.3.3.2).

For the two SM simulations, it is clear that the simulation cost of the process has been reduced almost by half (43%), when compared with the SM simulation using the mesh generation process presented in [4] (*). This can be expected, since with the new meshing method, utilizing both A and B mesh generation methods (Section 4.2), the triple intersection (Fig. 4.8) can be correctly represented without an increase in the Refinement Level [eq.(4.1)], therefore using less faces on the AMI Interface. This reduction in AMI faces, translates to a reduction in simulation cost of the process.

This cost reduction is essential from an industrial point of view, since several more simulations, more accurate than the TV approach can take place during one car developing project. Using the Hybrid Approach (Section 7.3) the simulation cost is expected to reduce even more, due to the further reduction in AMI face count.

5.2 Treaded Tire Investigation Results

In this section the simulation setup and the corresponding results of the tread impact investigation are presented. This investigation is the second part of this work and is composed of three simulations.

The first simulation (Simulation A) corresponds to a grooved tire (Fig. 4.23, top figure) where the RWBC will be imposed without the introduction of errors (due to the surface orientation w.r.t. the rotational vector $\vec{\Omega}$).

The second simulation (Simulation B) corresponds to a treaded tire (Fig. 4.23, bottom figure) where the RWBC will be imposed, introducing an erroneous BC for the velocity on the cells that are oriented accordingly (Fig. 3.5).

The third simulation (Simulation C) corresponds to a treaded tire where the MRF (Section 3.3.2) condition will be imposed on the cells residing inside of the treads 4.18. For the rest of the tire, the RWBC will be imposed without any introduction of errors.

5.2.1 Grooved and Treaded Tire Comparison

In Fig. 5.14, the position of the Y-plane relative to the wheel is presented. The position is such, so that the treaded part of the tire intersects the plane, so that an accurate representation of the tread's impact in the flow field is visualized.

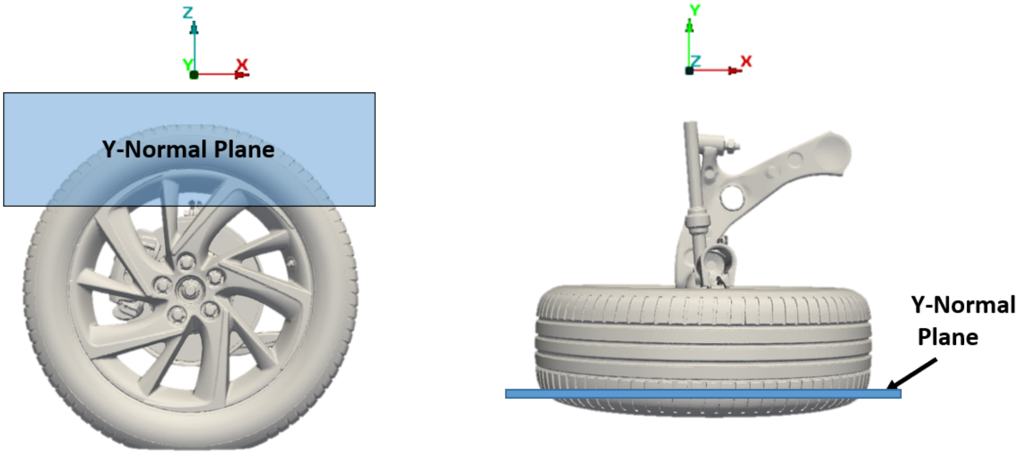

Figure 5.14: *Position of the Y-normal plane relative to the wheel.*

Figure 5.15 shows the contour of the velocity magnitude for a grooved tire (Simulation A), a treaded tire where the RWBC is imposed on the inner tread surfaces (Simulation B), and a treaded tire where the MRF condition is imposed on the inner tread surfaces (Simulation C).

Firstly, a difference in the generated wake is presented. For simulation A, the separation of the flow seems to begin earlier, following a similar behaviour to simulation C. However, simulation B shows a big difference in the generated wake when compared to the other two, and the separation of the flow seems to take place further back along the tire's surface.

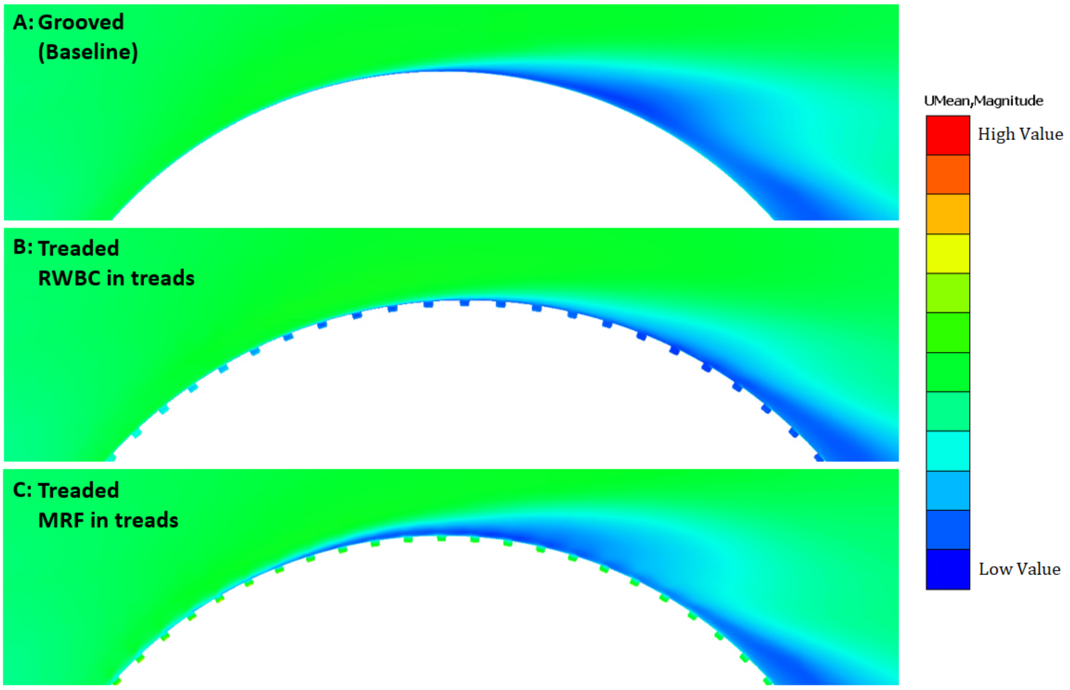

Figure 5.15: *Velocity magnitude contour for A, B and C simulations on the Y-normal plane.*

The biggest difference lies in velocity field inside the tread area. For simulation B, the velocity in the domain inside the treads is almost zero (dark blue color), indicating that the flow there is mostly stationary. On the contrary, in simulation C the MRF condition introduces a circumferential component in the velocity field inside of the treads, including the surrounding surfaces. Therefore, the velocity inside the treads is closer to the velocity of the rotating tire surface underneath (light green color).

These differences in the flow field can be traced back to the imposed velocity on the inner tread surfaces (fig. 3.7) and the vulnerability of the RWBC to correctly represent the velocity in non-axi-symmetric geometries.

In Fig. 5.16, the three simulations are compared in terms of the calculated normalized drag and the simulation cost.

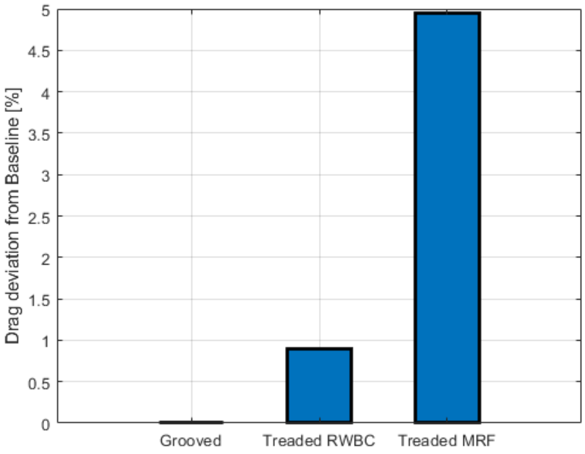

(a) *Normalized Drag (Cd*A) deviation from baseline (Grooved).*

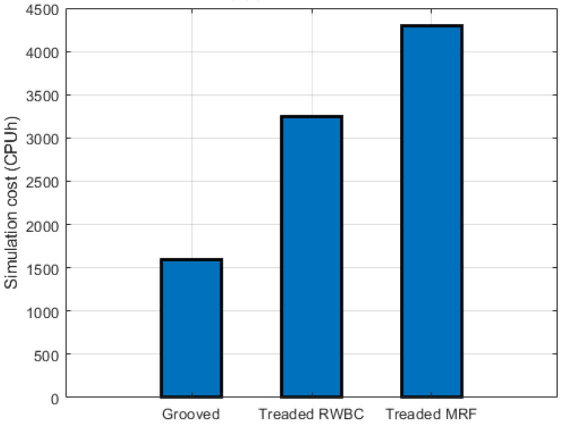

(b) *Simulation cost comparison*

Figure 5.16: *Calculated Drag and Simulation cost comparison*

Figure 5.16 (a) shows the deviation of the calculated normalized drag coefficient (Cd*A), from the baseline case, which is the grooved tire case. The grooved tire approach is the one commonly used. The value of the calculated drag increases with the inclusion of the treads in the mesh, even when the RWBC is used on the inner tread surfaces. The increase is even more pronounced when using the more accurate MRF condition in the domain inside the treads. The difference is not negligible, since for the Treaded MRF case (Simulation C) the increase is more than six counts, which is roughly 5% of the baseline's normalized drag coefficient value. However, this increase is limited to a single wheel simulation, where the tire is exposed to the stream of air. In a full car simulation the tire would be placed behind the front bumper, therefore causing the flow characteristics to change, and therefore the drag value to behave differently.

Figure 5.16 (b) shows the simulation cost of each simulation, expressed in CPU-hours. The inclusion of the treads in the mesh increases the simulation cost to twice the baseline value. This is partly due to the reduction in the time-step by half, which is however necessary for the correct convergence of the simulation. When using the more accurate, yet more demanding MRF approach for the treaded tire, the simulation cost increases to almost three times the one of the baseline case.

For the three simulations the rotation of the spokes was represented by the RWBC. A combined approach, where the SM condition is used for the spokes and the treads are included in the tires would cause the simulation cost of the process to increase to unbearable levels, and is not a part of this work.

Chapter 6

Summary and Conclusions

6.1 Summary

In this work, a new method was developed and tested for the generation of computational meshes, compatible with the SM technique for capturing the rotation of the spokes of a passenger car. For this, both A and B methods were used in order to generate the mesh for the rotating and the stationary domains respectively. Using this technique, the mesh was generated for four out of four wheels on which the method was tested on. The result is an accurate representation of the surfaces even in the most challenging areas. Furthermore, the new method allows the reduction of the number of AMI faces on the AMI surface, which are responsible for the increased simulation cost of the SM process when compared to the more simplistic TV approach.

Using a mesh generated with the new technique, a simulation was conducted and compared to the TV approach w.r.t. the flow field characteristics and simulation cost. In order to validate the new method's accuracy, the drag coefficient was compared to the value acquired during a wind tunnel experiment for the same setup as the one used in the simulations.

As a second part of this work, a preliminary investigation on the impact of the treads on a tire was conducted using a single wheel setup. First, the method of capturing the treads in the mesh was developed, and then three simulations were conducted in order to compare a treaded tire with the currently used approach, which is a grooved tire.

6.2 Conclusions

The new meshing method shows great handling of the mesh in the challenging areas and allows the reduction on the number of AMI faces. Furthermore it proves its robustness since four out of four wheels were meshed correctly.

The reduction of the AMI faces results in a decrease in simulation cost as expected. Furthermore, the simulation's accuracy has not suffered since it still manages to predict the aerodynamic resistance of the car with a very small deviation from the Wind Tunnel data.

From an industrial point of view, the increase in robustness and the reduction in simulation, without a decrease in accuracy, is of great value.

The investigation of the treaded tire showed that the difference in the calculated drag, when including the tire's treads in the mesh, is not negligible. Therefore, taking into account the fact that real-wold tires are fully-treaded, an increase in simulation accuracy might be achieved by including the treads in the simulation. However, the increase in simulation cost, compared to the currently used grooved tire, is a difficult challenge to overcome.

6.3 Proposal for Future Work

Through this work, areas of interest to be investigated can be highlighted as follows:

Sliding Mesh:

- Test the simulation cost impact of the *HybridApproach* in the mesh generation process, presented in the Appendix (7).
- Using the new robust method of generating meshes compatible with the SM approach, test the method's accuracy by simulating a wide variety of wheel set-ups backed by Wind Tunnel data.
- Investigate options of speeding up the SM simulation by improving / optimizing the AMI weights calculation code.

Treaded Tire Investigation:

- Using the method developed for generating the mesh for treaded tires, simulate a full-car where the treads are included and compare with Wind Tunnel data, where a treaded tire is used.
- Using both methods presented in this work, simulate the impact of the treaded tires while including the Sliding Mesh method for the rotation of the spokes.

Chapter 7

AMI faces reduction

In this Appendix the challenge of reducing the AMI face count even more is presented. Furthermore, a new method is explained that has proved to tackle the problem effectively.

For this purpose, two surface handling options are used in the mesh generation process. One is the handling of the surface as a **boundary** for the mesh and the other is the handling of the surface as an **internal** surface [24].

7.1 Limitations

The reduction in AMI faces is directly linked to the reduction of the simulation cost of the Sliding Mesh approach. Using a combination of Methods A and B, the total number of faces is reduced without a drop in mesh quality. However, in order to accurately capture some areas, a refinement is still necessary, resulting in a local increase in AMI faces. One of the key areas and the most influential one is located at the proximity between the brake caliper and the AMI surface, presented in Fig. 7.1.

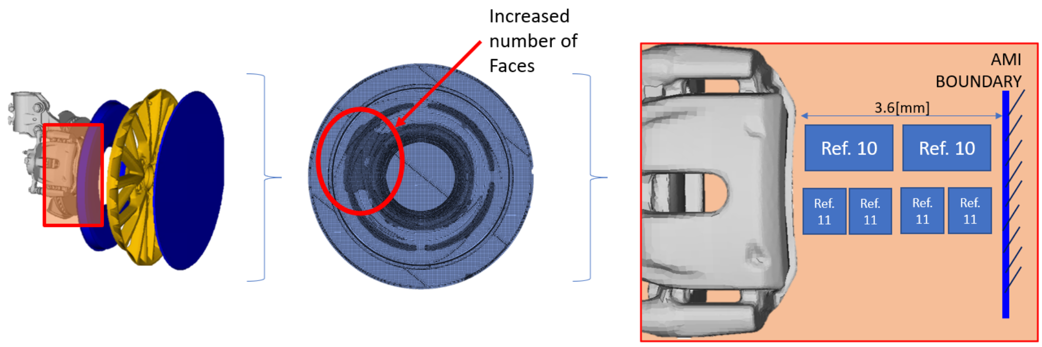

Figure 7.1: *Proximity of the Brake Caliper and AMI surface results in increased refinement.*

Fig. 7.1 shows that in order to capture the geometry correctly, an increase in refinement level has to be used locally. This is done so that the meshing software can place the cells correctly in this narrow area between the caliper and the AMI surface. If a local refinement is not used (eg. using Refinement Level of 9), the result is a deformed mesh, where the AMI surface and the brake caliper have essentially merged (Fig. 7.2).

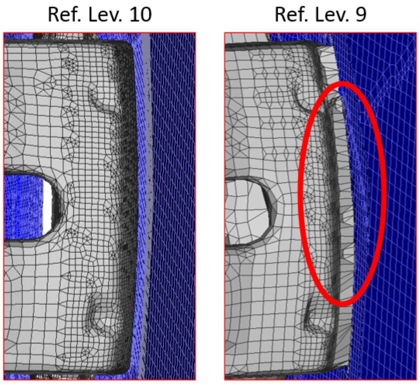

Figure 7.2: *Merging of AMI surface with Brake Caliper if no increased refinement is applied.*

The reason is that in this work the AMI surface is used as a boundary, therefore forcing the meshing software to fit small cells in between the tight space highlighted in Fig. 7.1. However, this approach has proved to be accurate and robust in the handling of the triple intersection area, that is the area where the AMI surface meets the rest of the wheel components 7.3.

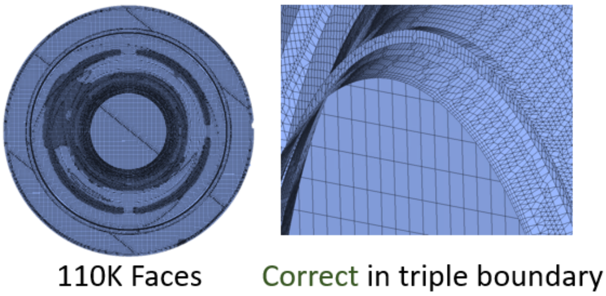

Figure 7.3: *Merging of AMI surface with Brake Caliper if no increased refinement is applied.*

In conclusion, using the AMI Surface as a boundary, has the advantage of correctly representing the AMI Surface in the triple intersection, but comes with an increase in the AMI face count, due to the refinement used to tackle the proximity between the AMI surface and the Brake Caliper.

7.2 Internal Surface ”solution”

As stated before, in this work the AMI surface is used as a boundary. This is not the case in [4] where the AMI surface was used as an internal surface. This is achieved since the meshing software is no longer forced to squeeze cells between the AMI and the Caliper, but has the freedom to place cells even after the AMI surface, as presented in Fig. 7.4.

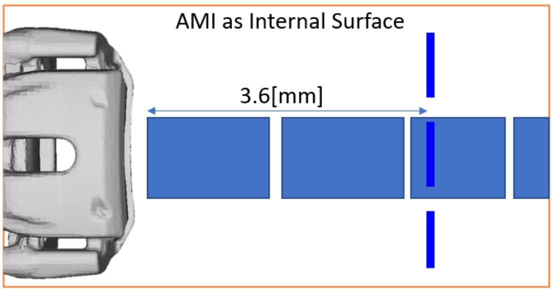

Figure 7.4: *Cells Placement using AMI as Internal Surface.*

Using the AMI as an internal surface has the immediate advantage of reducing the AMI face count, by overcoming the proximity problem on the brake caliper area, as seen on Fig. 7.4.

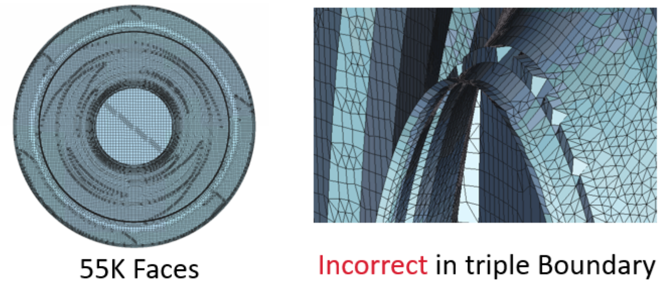

Figure 7.5: *Brake Caliper impact problem solved (Left). Incorrect representation of the triple connection (right).*

However, because of the way the meshing software deals with the internal surface, in the challenging area, the cells are not placed correctly and the surface is not correctly represented.

In conclusion, using the AMI surface as an internal surfaces, reduces the number of AMI faces (by overcoming the AMI - Caliper proximity limitation) but gives a poor representation in the triple intersections.

7.3 Hybrid Approach

Taking into consideration the conclusions from the previous sections, the hybrid approach is presented as a way of including the best out of the two approaches (AMI as boundary and AMI as internal).

The AMI surface is split into two. In the area where the triple intersections lie, the AMI surface is used as a boundary. On the rest of the surface, in order to overcome the proximity limitations, the AMI surface is used as an internal surface. Fig. 7.6 shows the areas where the AMI Surface is used as a boundary and as an Internal Surface.

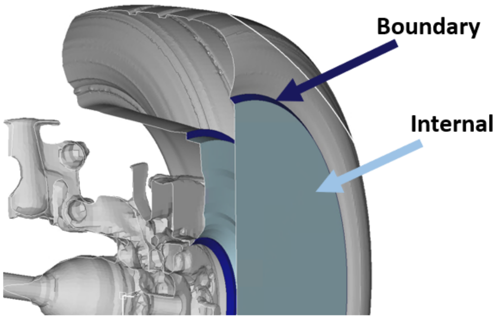

Figure 7.6: *Differentiation of the AMI Surface to be handled both as an Internal Surface and as a Boundary.*

This differentiation begins in the surface preparation process (by splitting the two) and is then stated in the mesh generation code (by the handling of each surface accordingly). The result is a correct representation of the triple intersection area, while the brake caliper proximity impact is no longer an issue, lowering the AMI face count even more (Fig. 7.7).

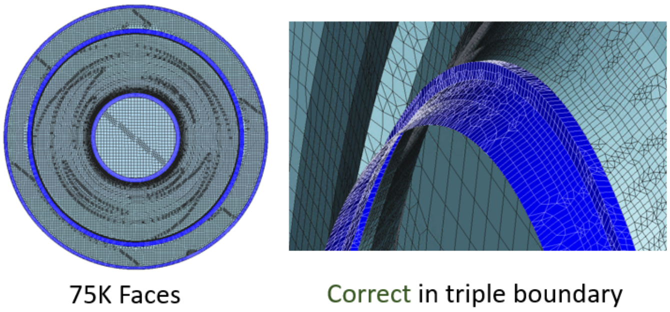

Figure 7.7: *Differentiation of the AMI Surface to be handled both as an Internal Surface and as a Boundary.*

This method was not tested in order to assess its accuracy. However, a reduction in simulation cost is expected due to the reduction in AMI faces.

Εκτενής Περίληψη Διπλωματικής Εργασίας

Εθνικό Μετσόβιο Πολυτεχνείο
Σχολή Μηχανολόγων Μηχανικών
Τομέας Ρευστών
Μονάδα Παράλληλης Υπολογιστικής Ρευστοδυναμικής
& Βελτιστοποίησης

Συμβολή στη *CFD* Μοντελοποίηση Περιστρεφόμενων Τροχών και Ανάγλυφων Ελαστικών σε Επιβατικά Αυτοκίνητα

Διπλωματική Εργασία

Γεώργιος Σμυρλής

Βιομηχανικός Διευθυντής:
Antoine Delacroix, Manager TME

Επιβλέπων:
Κυριάκος Χ. Γιαννάκογλου, Καθηγητής ΕΜΠ

Αθήνα, 2021

Εισαγωγή

Τις τελευταίες δεκαετίες η αυτοκινητοβιομηχανία έχει εντείνει τις προσπάθειες ανάπτυξης μοντέλων πρόλεξης των αεροδυναμικών χαρακτηριστικών των αυτοκινήτων, σε μία προσπάθεια μείωσης του περιβαλλοντικού αποτυπώματος που επιφέρει η χρήση αυτών. Οι ευρωπαϊκοί κανονισμοί που τέθηκαν σε ισχύ από τον Σεπτέμβριο του 2017 αυξάνουν την ανάγκη για ακριβή μοντέλα πρόλεξης των αεροδυναμικών επιδόσεων των αυτοκινήτων, καθώς κάθε παραλλαγή ενός μοντέλου πρέπει να πιστοποιείται για το περιβαλλοντικό της αποτύπωμα (εκπομπές CO_2). Οι εκπομπές αυτές συνδέονται άρρηκτα με τον συντελεστή αεροδυναμικής αντίστασης του αυτοκινήτου.

Οι περιστρεφόμενοι τροχοί των αυτοκινήτων είναι υπεύθυνοι για το 20% της αεροδυναμικής τους αντίστασης. Το 50% της αντίστασης οφείλεται στις εξωτερικές επιφάνειες του αυτοκινήτου ενώ, το υπόλοιπο 30% οφείλεται στο σύστημα ψύξης-εξαερισμού και στις διαμορφώσεις του κάτω μέρους του αυτοκινήτου. Επομένως, η σωστή μοντελοποίηση των περιστρεφόμενων τροχών είναι βασική για τη σωστή πρόβλεψη των αεροδυναμικών χαρακτηριστικών του αυτοκινήτου.

Σκοπός της εργασίας είναι η ανάπτυξη μεθόδου πλεγματοποίησης που αποσκοπεί στη μείωση του υπολογιστικού κόστους της πρόλεξης των αεροδυναμικών χαρακτηριστικών του αυτοκινήτου. Χρησιμοποιείται η Μέθοδος Ολισθαίνοντος Πλέγματος για τη μοντελοποίηση της περιστροφής των τροχών. Επιπλέον, διερευνάται η επίδραση των ανάγλυφων ελαστικών στην αεροδυναμική του τροχού.

Μοντελοποίηση της ροής

Για την ανάλυση της τυρβώδους ροής γύρω από το αυτοκίνητο εφαρμόζονται δύο προσεγγίσεις. Η πρώτη προσέγγιση είναι αυτή των $RANS$ εξισώσεων με το μοντέλο των $Spalart - Allmaras$, η οποία χρησιμοποιείται για την αρχικοποίηση του πεδίου. Στη συνέχεια, το τυρβώδες μη-μόνιμο πεδίο ροής μοντελοποιείται με χρήση του μοντέλου $DDES$, σύμφωνα με το οποίο επιλύονται οι εξισώσεις $RANS$ κοντά στα στερεά τοιχώματα και οι εξισώσεις LES μακριά από αυτά. Η περιοχή κοντά στα στερεά τοιχώματα μοντελοποιείται με τη βοήθεια συναρτήσεων τοίχου ώστε να υπολογιστούν οι τυρβώδεις μεταβλητές, αποφεύγωντας τη χρήση πολύ πυκνού πλέγματος στην περιοχή αυτή. Για την επίλυση του πεδίου χρησιμοποιείται το ανοιχτό λογισμικό $OpenFOAM^{©}$ που χρησιμοποιεί τη μέδοθο πεπερασμένων όγκων για τη διακριτοποίηση των εξισώσεων.

Μέθοδοι Μοντελοποίησης Περιστροφής

- **Μέθοδος Εφαπτομενικής Ταχύτητας:** Η μέθοδος αυτή μοντελοποιεί την περιστροφή της εκάστοτε επιφάνειας μέσω της επιβολής κατάλληλου εφαπτομενικού διανύσματος ταχύτητας στην επιφάνεια αυτή. Η ταχύτητα που επιβάλλεται στην επιφάνεια είναι αυστηρά εφαπτομενική, καθώς το κάθετο στην επιφάνεια διάνυσμα μηδενίζεται, ώστε να μην εισέρχεται ροή στο πεδίο μέσω της επιφάνειας αυτής. Επομένως, επιφάνειες κάθετες στη διεύθυνση περιστροφής μοντελοποιούνται με εισαγωγή σφαλμάτων.

- **Μέθοδος Πολλαπλών Συστημάτων Αναφοράς:** Οι εξισώσεις επιλύονται σε σχετικό σύστημα αναφοράς ως προς το ολικό (στατικό) σύστημα αναφοράς. Με τον τρόπο αυτό, προκύπτουν πρόσθετοι όροι πηγής στις εξισώσεις διατήρησης ορμής, προσεγγίζοντας έτσι την περιστροφική κίνηση με την χρήση στατικού πλέγματος. Η τεχνική αυτή χρησιμοποιείται για τη μοντελοποίηση της περιστροφής των ανάγλυφων ελαστικών.
- **Μέθοδος Ολισθαίνοντος Πλέγματος:** Το πλέγμα χωρίζεται σε στατικό και περιστρεφόμενο. Το τελευταίο, περιστρέφεται σε κάθε χρονικό βήμα της μη-μόνιμης μοντελοποίησης, με αποτέλεσμα την περιστροφή του χωρίου στο οποίο περιέχονται οι περιστρεφόμενες επιφάνειες. Για την επικοινωνία του περιστρεφόμενου και του στατικού χωρίου χρησιμοποιείται η τεχνική Διεπαφής Αυθαίρετων Πλεγμάτων (*AMI*) ώστε να επιτευχθεί η επικοινωνία ανάμεσα στα μη-σύμμορφα όρια των δύο χωρίων.

Γένεση Υπολογιστικού Πλέγματος

Η τεχνική που αναπτύχθηκε στο πλαίσιο της ΔΕ, αξιοποιεί δύο διαφορετικές μεδόδους (A & B) για την γένεση πλέγματος συμβατού με την μέθοδο ολισθαίνοντος πλέγματος για τη μοντελοποίηση της περιστροφής των τροχών του αυτοκινήτου.

- **Μέθοδος A:** Η πρώτη μέθοδος γένεσης υπολογιστικού πλέγματος ξεκινά με τη δημιουργία ενός απλού πλέγματος-βάσης, το οποίο, στη συνέχεια, μορφοποιείται ώστε οι κόμβοι του να συμπίπτουν με την επιφάνεια της γεωμετρίας προς πλεγματοποίηση. Η μέθοδος αυτή δεν απαιτεί ιδιαίτερη προετοιμασία των επιφανειών, αλλά η ακρίβεια του πλέγματος εξαρτάται από την ανάλυση του πλέγματος στην εκάστοτε επιφάνεια.
- **Μέθοδος B:** Η πλεγματοποίηση ξεκινά με την τοποθέτηση των κόμβων στην επιφάνεια της γεωμετρίας προς πλεγματοποίηση και την δημιουργία ενός επιφανειακού πλέγματος. Στη συνέχεια, ο όγκος πλεγματοποιείται με βάση το επιφανειακό πλέγμα με αποτέλεσμα το ογκικό πλέγμα. Η μέθοδος αυτή απαιτεί ιδιαίτερη προετοιμασία των επιφανειών της γεωμετρίας καθώς οι επιφάνειες πρέπει να είναι αυστηρά πλήρως σύμμορφες.

Η μέθοδος A χρησιμοποιείται για την πλειονότητα του υπολογιστικού χωρίου, ενώ η μέθοδος B χρησιμοποιείται τοπικά για το περιστρεφόμενο χωρίο. Με τον τρόπο αυτό, το κόστος (σε εργατοώρες) για την προετοιμασία των επιφανειών παραμένει χαμηλό, ενώ η αποτύπωση των επιφανειών στο πλέγμα βελτιώνεται με τη χρήση της πιο ακριβούς μεθόδου B.

Το Σχήμα 3 αποτυπώνει τα δύο χωρία. Στα αριστερά, το στάσιμο χωρίο πλεγματο-

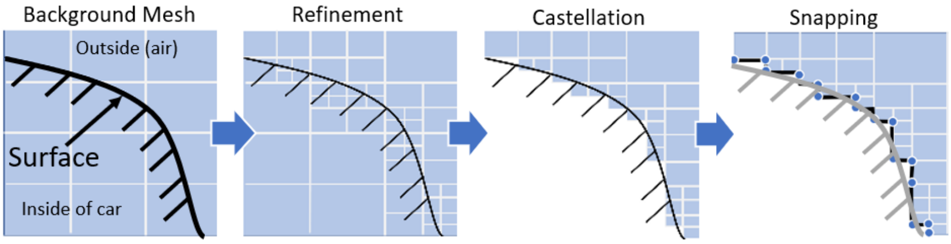

Σχήμα 1: *Οπτικοποίηση της μεθόδου Α για την γένεση πλέγματος.*

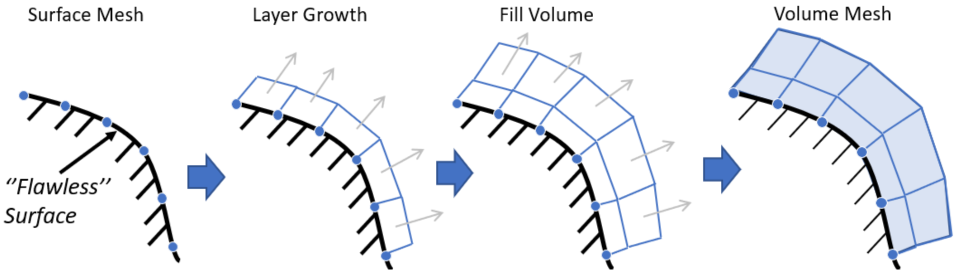

Σχήμα 2: *Οπτικοποίηση της μεθόδου Β για την γένεση πλέγματος.*

ποιείται με τη μέθοδο Α, ενώ στα δεξιά, το περιστρεφόμενο χωρίο πλεγματοποιείται με τη μέθοδο Β. Το όριο που διαχωρίζει τα δύο χωρία είναι η AMI επιφάνεια που αποτυπώνεται με μπλέ χρώμα.

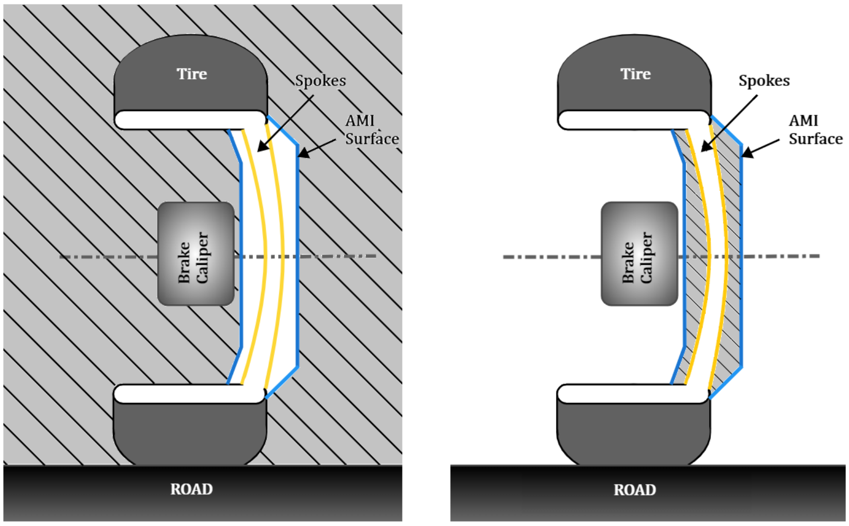

Σχήμα 3: *Τομή του τροχού για το στάσιμο χωρίο (αριστερά) και το περιστρεφόμενο χωρίο (δεξιά).*

Η ολοκληρωμένη τεχνική για τη γένεση πλέγματος συμβατού με την τεχνική ολισθαίνοντος πλέγματος (Sliding Mesh) για την περιστροφή των τροχών αποτυπώνεται στο Σχήμα 4 σε μορφή διαγράμματος ροής.

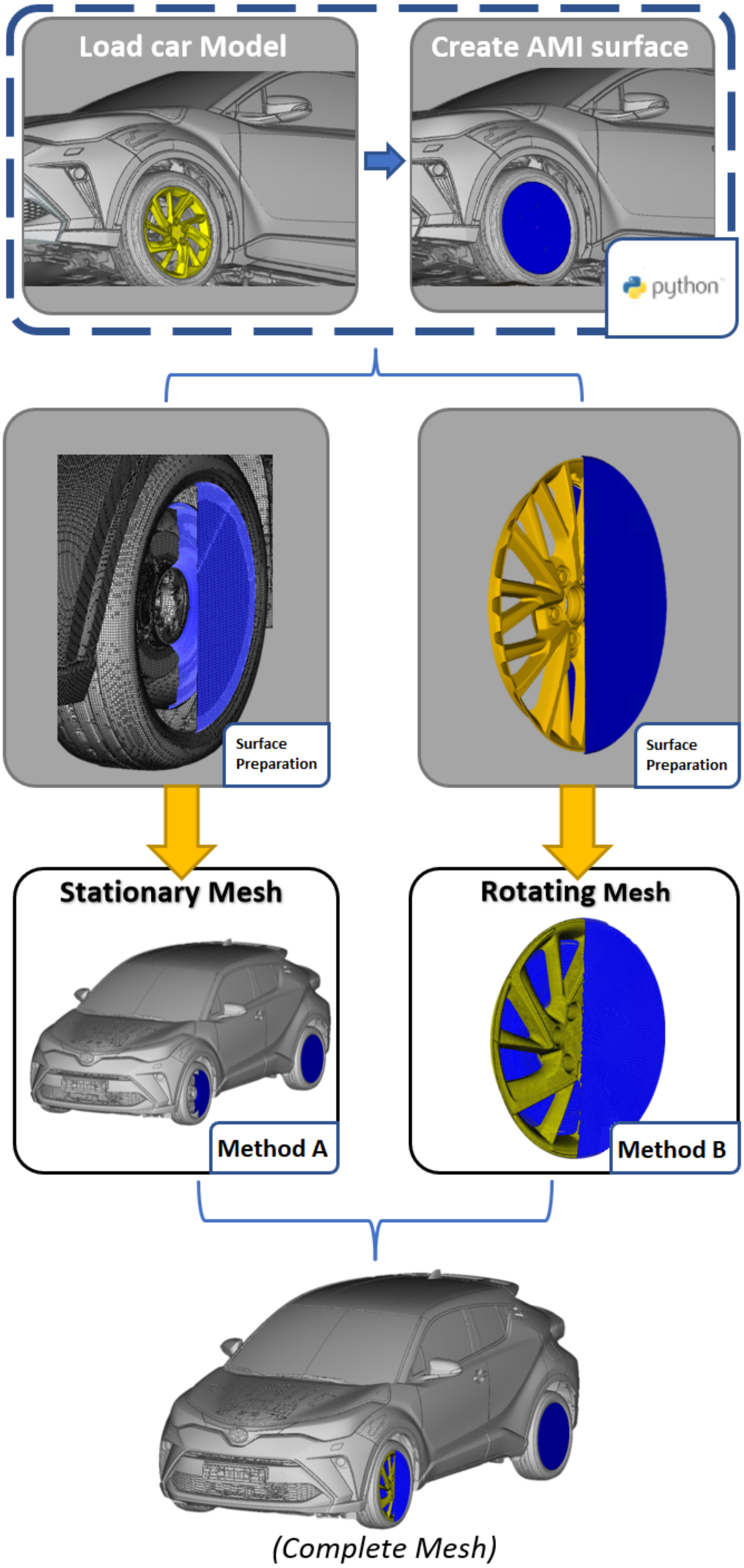

Σχήμα 4: *Διάγραμμα ροής της τεχνικής πλεγματοποίησης (Μέθοδος Α: Ογκικό πλέγμα σε επιφανειακό, Μέθοδος Β: Πρώτα επιφανειακό πλέγμα).*

Με τη χρήση της παραπάνω διαδικασίας, πλεγματοποιείται το χωρίο του σχήματος 5 που αντιστοιχεί στην πειραματική διάταξη της αεροσήραγγας.

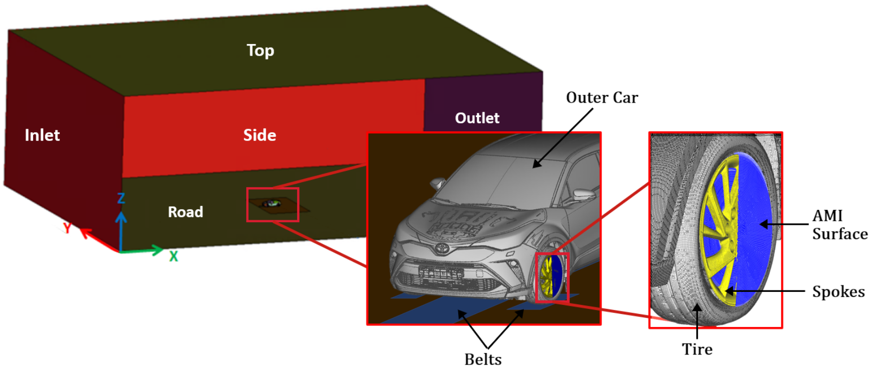

Σχήμα 5: *Χωρίο προς πλεγματοποίηση για την μέθοδο ολισθένοντος πλέγματος (Sliding Mesh).*

Στην συνέχεια, η μέθοδος ολισθαίνοντος πλέγματος (SM) (όπου η γένεση του πλέγματος έγινε με τη νέα τεχνική) αξιολογείται μέσω της σύγκρισης των χαρακτηριστικών της ροής με την μοντελοποίηση που αντιστοιχεί στην ίδια γεωμετρία, όπου η περιστροφή των τροχών μοντελοποιείται με την μέθοδο εφαπτομενικής ταχύτητας (TV). Η ακρίβεια των δύο μεθόδων, αξιολογείται μέσω της σύγκρισης του συντελεστή αντίστασης (C_d) των μοντελοποιήσεων με την αντίστοιχη τιμή του πειράματος της αεροσήραγγας για την ίδια γεωμετρία.

Με τη χρήση της προτεινόμενης τεχνικής πλεγματοποίησης, είναι δυνατή η μείωση του αριθμού των επιφανειακών κελιών ($faces$) που αποτελούν την επιφάνεια AMI στο πλέγμα. Στο Σχήμα 6 φαίνονται τα $faces$ που συντελούν την επιφάνεια αυτή, ενώ στο Σχήμα 7 φαίνεται η απεικόνιση του πλέγματος στο σημείο τομής της AMI επιφάνειας με τις ζάντες του αυτοκινήτου. Αριστερά φαίνεται το αποτέλεσμα της μεθόδου που χρησιμοποιήθηκε στο [4], που αντιστοιχεί στην **Μέθοδο A**. Δεξιά, το αποτέλεσμα της μεθόδου που προτάθηκε, αξιοποιώντας τις **Μεθόδους A** και **B**, μειώνοντας τον αριθμό των $faces$ στην AMI επιφάνεια. Επομένως, το υπολογιστικό κόστος της μεθόδου SM μειώνεται (βλ. Κεφάλαιο 7.3).

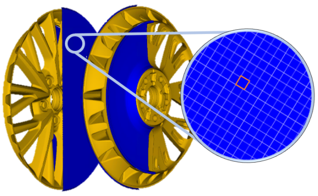

Σχήμα 6: *AMI faces.*

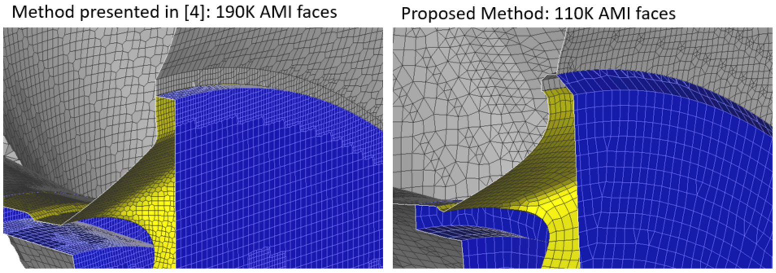

Σχήμα 7: *Σύγκριση επιφάνειας AMI στο πλέγμα.*

Γένεση πλέγματος για ανάγλυφα ελαστικά.

Η εργασία αυτή περιλαμβάνει και τη διερεύνηση στην επίδραση του αναγλύφου των ελαστικών στην αεροδυναμική ενός τροχού. Συγκεκριμένα συγκρίνονται δύο διαφορετικά πλέγματα· ένα στο οποίο δεν αποτυπώνεται το ανάγλυφο του ελαστικού και ένα στο οποίο αποτυπώνεται το ανάγλυφο (Σχήμα 8).

Σχήμα 8: *Λείο ελαστικό (αριστερά), ανάγλυφο ελαστικό (δεξιά).*

Το πρώτο βήμα είναι η δημιουργία της γεωμετρίας η οποία θα χρησιμοποιηθεί από τον πλεγματοποιητή. Η γεωμετρία αυτή δημιουργείται με βάση ένα σύνολο σημείων που προκύπτει από τριδιάστατη σάρωση της επιφάνειας ενός πραγματικού ελαστικού (Σχήμα 9). Με τη χρήση λογισμικού CAD, δημιουργείται η λεπτομερής επιφάνεια η οποία χρησιμοποιείται από τον πλεγματοποιητή (Σχήμα 10).

Σχήμα 9: *Αποτέλεσμα τρι-διάστατης σάρωσης του ανάγλυφου ελαστικού.*

Σχήμα 10: *Επιφάνεια προς πλεγματοποίηση.*

Για τη μοντελοποίηση της περιστροφής του ανάγλυφου ελαστικού, χρησιμοποιείται η μέθοδος πολλαπλών συστημάτων αναφοράς (MRF) για το χωρίο στα εσωτερικά των εσοχών του ανάγλυφου ελαστικού.

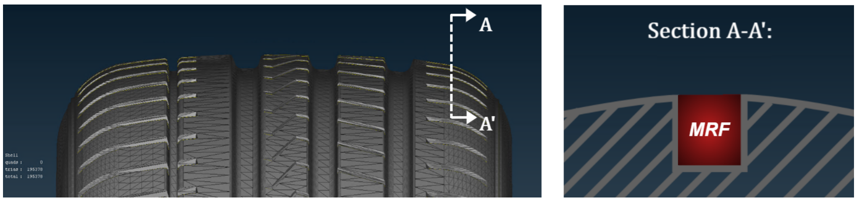

Σχήμα 11: *Χωρίο στο οποίο επιβάλλεται η συνθήκη MRF.*

Για τη διαφοροποίηση του χωρίου αυτού δημιουργούνται οι κλειστές επιφάνειες που φαίνονται στα αριστερά του Σχήματος 12 . Το αποτέλεσμα είναι η διαφοροποίηση των χωρίων στο στάδιο της πλεγματοποίησης και η επιβολή της συνθήκης MRF τοπικά στο χωρίο που αποτυπώνεται στο Σχήμα 11.

Μέσω της διαδικασίας αυτής, δημιουργείται το πλέγμα που περιγράφει το ανάγλυφο ελαστικό του Σχήματος 8 (δεξιά), καθώς και το πλέγμα που περιγράφει το λείο ελαστικό

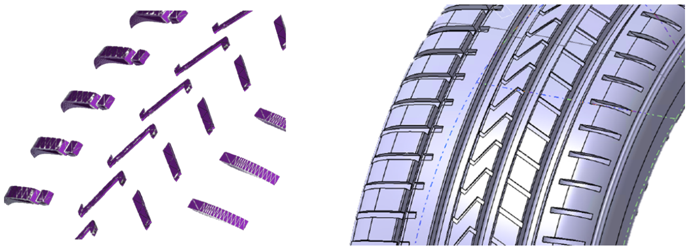

Σχήμα 12: *Δημιουργία επιφανειών για την διαφοροποίηση του εσωτερικού όγκου των διαμορφώσεων του ανάγλυφου ελαστικού (αριστερά), επιφάνεια ανάγλυφου ελαστικού (δεξιά).*

του Σχήματος 8 (αριστερά), με σκοπό τη σύγκρισή των αεροδυναμικών χαρακτηριστικών του λείου και του ανάγλυφου πλέγματος. Το υπολογιστικό χωρίο, αποτελείται από έναν μεμονωμένο τροχό (Σχήμα 13).

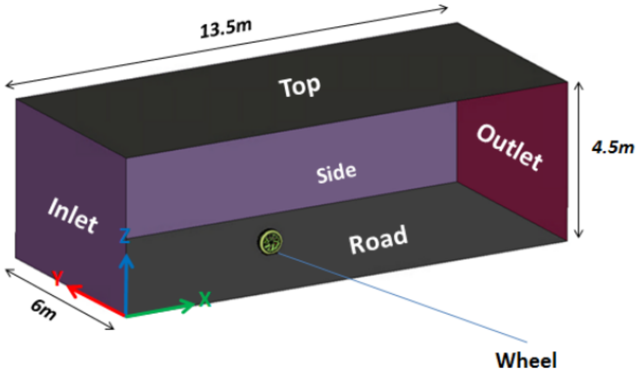

Σχήμα 13: *Υπολογιστικό χωρίο για την μοντελοποίηση μεμονομένου τροχού.*

Συνολικά πραγματοποιούνται τρεις μοντελοποιήσεις για τη διερεύνηση της επίδρασης του αναγλύφου των ελαστικών στην αεροδυναμική του τροχού. Η πρώτη αφορά το λείο ελαστικό στο οποίο εφαρμόζεται η συνθήκη εφαπτομενικής ταχύτητας στην επιφάνεια του ελαστικού. Η δεύτερη αφορά ένα ανάγλυφο ελαστικό στο οποίο εφαρμόζεται η συνθήκη εφαπτομενικής ταχύτητας στην επιφάνεια του ελαστικού. Η τρίτη μοντελοποίηση αφορά το ανάγλυφο ελαστικό, με τη χρήση της συνθήκης πολλαπλών συστημάτων αναφοράς (MRF) για το εσωτερικό των διαμορφώσεων του ελαστικου, ώστε να μοντελοποιηθεί η περιστροφή του.

Αποτελέσματα

Μοντελοποίηση Πλήρους Αυτοκινήτου.

Έγινε εφαρμογή της μεθόδου ολισθαίνοντος πλέγματος [Sliding Mesh (SM)] για την προσομοίωση της περιστροφής των τροχών, με στόχο την πρόλεξη πεδίου μη-μόνιμης ροής γύρω από επιβατικό όχημα με περιστρεφόμενους τροχούς. Χρησιμοποιήθηκε το μοντέλο Spalart-Allmaras με συναρτήσεις τοίχου. Το πεδίο ροής συγκρίνεται με αυτό όπου χρησιμοποιήθηκε η μέθοδος εφαπτομενικής ταχύτητας για την προσομοίωση της περιστροφής των τροχών [Tangential Velocity (TV)].

Τα μεγέθη της ροής αποτυπώνονται σε δύο επίπεδα, η θέση των οποίων παρουσιάζεται στα Σχήματα 14 & 15.

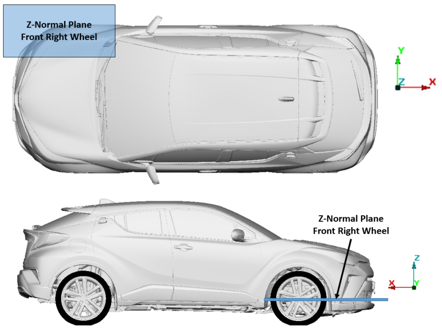

Σχήμα 14: *Θέση του κάθετου στον Z-άξονα επιπέδου.*

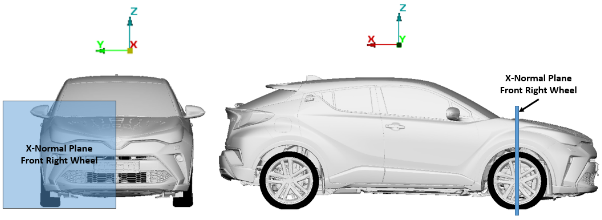

Σχήμα 15: *Θέση του κάθετου στον X-άξονα επιπέδου.*

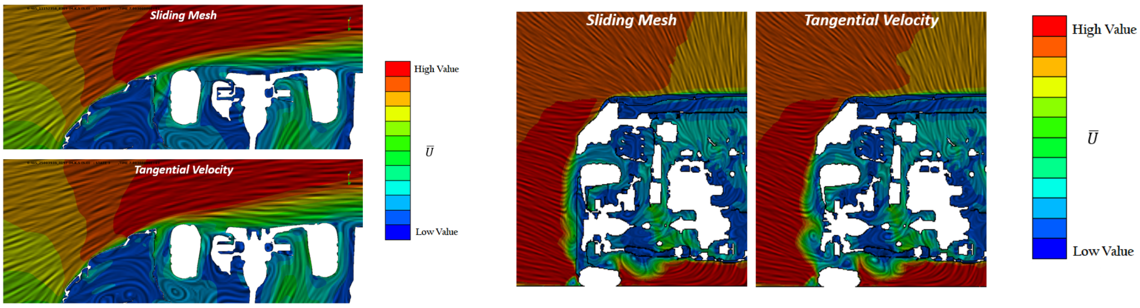

Σχήμα 16: *LIC οπτικοποίηση του πεδίου ροής με χρώμα που υποδυκνεύει το μέτρο της ταχύτητας της ροής.*

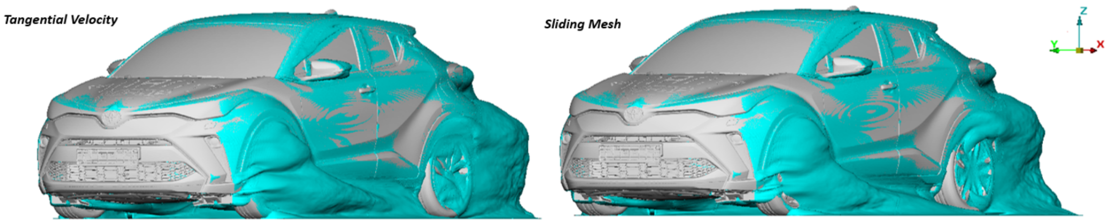

Σχήμα 17: *Επιφάνεια σταθερού συντελεστή ολικής πίεσης Cp_t.*

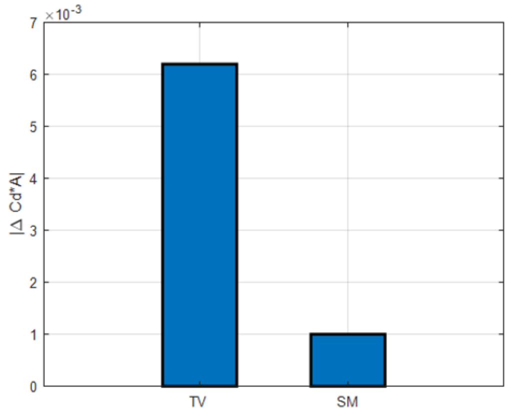

Σχήμα 18

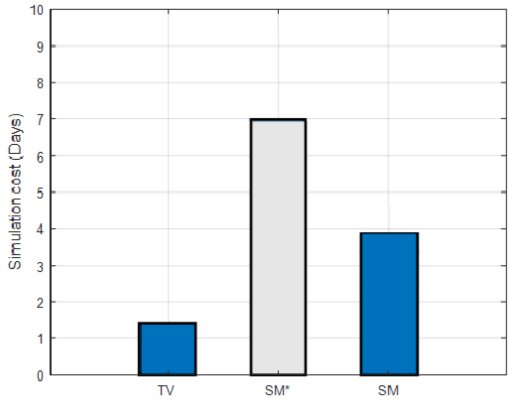

Σχήμα 19

Σχήμα 18: Απόλυτη απόκλιση από την πειραματική τιμή του αδιαστατοποιημένου συντελεστή αντίστασης (C_d) (TV: Tangential Velocity, SM: Sliding Mesh).

Σχήμα 19: Σύγκριση υπολογιστικού κόστους (TV: Tangential Velocity, SM: Sliding Mesh με την προτεινόμενη τεχνική πλεγματοποίησης, χρήση των μεθόδων A & B για την γένεση του πλέγματος, SM*:[4], όπου η μέθοδος A χρησιμοποιήθηκε για την γένεση του πλέγματος).

Μοντελοποίηση Μεμονωμένου Τροχού.

Έγινε εφαρμογή της μεθόδου πολλαπλών συστημάτων αναφοράς (MRF) για την διερεύνηση της επίδρασης των ανάγλυφων ελαστικών στην αεροδυναμική του μεμονωμένου τροχού. Τα αποτελέσματα συγκρίνονται με τις μοντελοποιήσεις του λείου, και του ανάγλυφου ελαστικού στα οποία γίνεται χρήση της τεχνικής εφαπτομενικής ταχύτητας ($RWBC$) για την προσομοίωση της περιστροφής τους. Σε όλες τις μοντελοποιήσεις, η περιστροφή των ζαντών μοντελοποιήθηκε με την τεχνική εφαπτομενικής ταχύτητας. Τα μεγέθη της ροής αποτυπώνονται στο επίπεδο του Σχήματος 20.

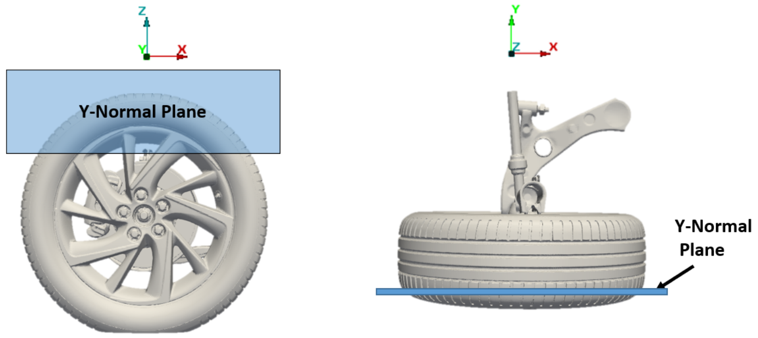

Σχήμα 20: *Θέση του επιπέδου κάθετου στον Υ-άξονα.*

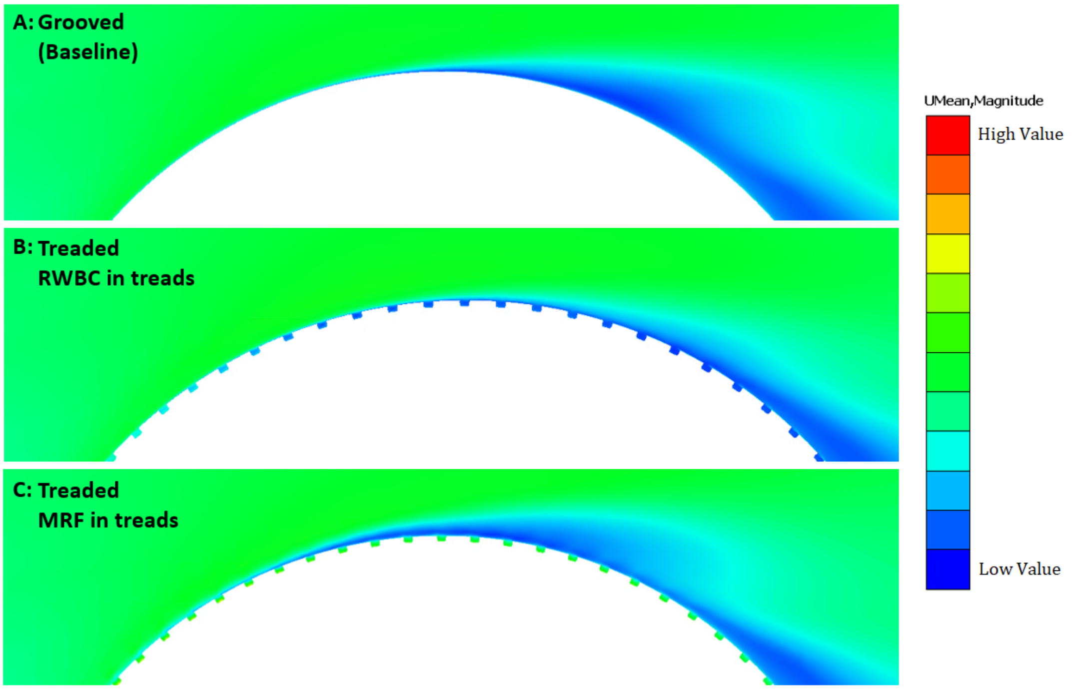

Σχήμα 21: *Πεδίο του μέτρου της ταχύτητας στο Υ-κάθετο επίπεδο. (A: λείο ελαστικό, B: Ανάγλυφο Ελαστικό με συνθήκη εφαπτομενικής ταχύτητας, Γ: Ανάγλυφο ελαστικό με συνθήκη MRF)*

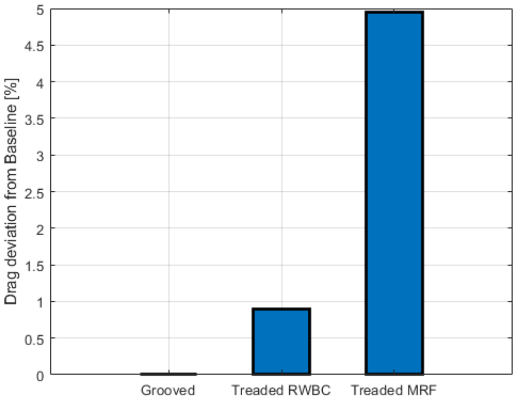

Σχήμα 22

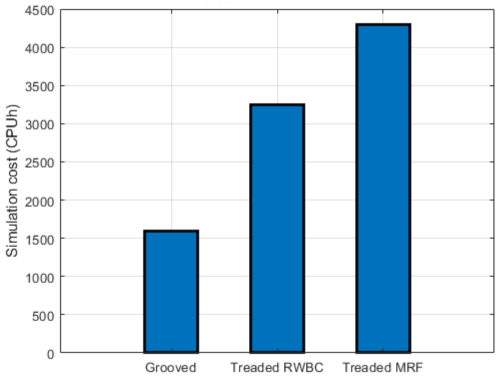

Σχήμα 23

Σχήμα 22: Απόλυτη απόκλιση από την τιμή για το λείο ελαστικό, του αδιαστατοποιημένου συντελεστή αντίστασης (C_d).

Σχήμα 23: Σύγκριση υπολογιστικού κόστους.

Συμπεράσματα

Σε αυτήν τη διπλωματική εργασία, εφαρμόσθηκε μία τεχνική δύο βημάτων για τη γένεση πλεγμάτων συμβατών με τη μέθοδο ολισθαίνοντος πλέγματος, με σκοπό τη μείωση του υπολογιστικού κόστους της αντίστοιχης μοντελοποίησης. Η ακρίβεια της μεθόδου στην δυνατότητα πρόλεξης των αεροδυναμικών χαρακτηριστικών ενός επιβατικού αυτοκινήτου επιβεβαιώθηκε μέσω της σύγκρισης με πειραματικά δεδομένα. Η προτεινόμενη τεχνική γένεσης υπολογιστικού πλέγματος, είχε ως αποτέλεσμα τη μείωση του υπολογιστικού κόστους της μοντελοποίησης σχεδόν στο μισό, συγκριτικά με την τεχνική πλεγματοποίησης που παρουσιάζεται στο [4], χωρίς αντίκτυπο στην ακρίβεια των αποτελεσμάτων.

Επιπλέον, έγινε διερεύνηση της επίδρασης των ανάγλυφων ελαστικών στην αεροδυναμική απόδοση μεμονομένου τροχού. Συγκεκριμένα, αναπτύχθηκε τεχνική γένεσης πλέγματος με στόχο την αποτύπωση των αναγλύφων του ελαστικού στο πλέγμα, και τον απαραίτητο διαχωρισμό των χωρίων για την εφαρμογή της μεθόδου πολλαπλών συστημάτων αναφοράς (MRF). Η αεροδυναμική αντίσταση παρουσιάστηκε αυξημένη για τη μοντελοποίηση του ανάγλυφου ελαστικού με τη χρήση της μεθόδου MRF στο εσωτερικό των διαμορφόσεων του ελαστικου. Παρόλα αυτά, το υπολογιστικό κόστος αυξήθηκε κατακόρυφα λόγω του αυξημένου αριθμού κελιών στο αντίστοιχο υπολογιστικό πλέγμα.

Bibliography

[1] European Environment Agency (EEA). “Greenhouse Gas Emissions From Transport”.

URL:

`https://www.eea.europa.eu/data-and-maps/indicators/transportemissions-of-greenhouse-gases/transport-emissions-of-greenhouse-gases-`

[2] WLTP - Worldwide Harmonized Vehicle Test Procedure

URL:

`https://nl.toyota.be/wltp`

[3] Uriegas, Andrés Contreras. CFD Investigation on Sliding Mesh as a Method to Model Wheel Rotation-Implementation and Analysis on Different Rims, MS thesis, 2018.

[4] A. Papakonstantinou, ”Investigation on Meshing Techniques for the CFD Modelling of Rotating Wheels in Cars”, MSc Thesis, NTUA, 021

[5] Hobeika, Teddy Sebben, Simone. (2018). Tyre Pattern Features and Their Effects on Passenger Vehicle Drag. SAE International Journal of Passenger Cars - Mechanical Systems. 11. 10.4271/2018-01-0710.

[6] S. Orszag, (1970). Analytical theories of turbulence. Journal of Fluid Mechanics, 41(2), 363-386. DOI:10.1017/S0022112070000642

[7] J. H. Ferziger, M. Perić, R. L. Street, Computational Methods for Fluid Dynamics (2020) DOI: 10.1007/978-3-319-99693-6

[8] O. Reynolds, (1895). ”On the Dynamical Theory of Incompressible Viscous Fluids and the Determination of the Criterion”. Philosophical Transactions of the Royal Society of London A. 186: 123–164

[9] P. R. Spalart, S. R. Allmaras, A One-Equation Turbulence Model for Aerodynamic Flows, 30th Aerospace Sciences Meeting and Excibit, Reno, NV, U.S.A. 1992.

[10] D. B. Spalding, A Single Formula for the Law of the Wall", Journal of Applied Mechanics, vol. 28, issue 3, 1961.

[11] Spalding Wall Function OpenFOAM implementation

URL: `https://www.openfoam.com/documentation/guides/latest/doc/guide-bcs-wall-turbulence-nutUSpaldingWallFunction`

[12] P. R. Spalart, S. Deck, M. L. Shur, K. D. Squires, M. Kh. Strelets, and A. Travin: A new version of detached-eddy simulation, resistant to ambiguous grid densities. In Theoretical and Computational Fluid Dynamics Journal, 20(3):181, May 2006.

[13] Ph. Spalart,WH Jou, M. Strelets, and S. Allmaras: Comments on the feasibility of les for wings, and on a hybrid rans/les approach. In International Conference on DNS/LES, Aug. 4-8, 1997, Ruston, Louisiana., 1997.

[14] Dymanic Mesh Motion Solver URL: `https://openfoamwiki.net/index.php/DynamicMeshDict`

[15] M. Beaudoin, H. Jasak, Development of a generalized grid interface for turbomachinery simulations with OpenFOAM, in: Open Source CFD International Conference, Berlin, 2008.

[16] OpenFOAM v6 User Guide: 4.4 Numerical schemes URL: `https://cfd.direct/openfoam/user-guide/v6-fvschemes/`

[17] P. Farrell, J. Maddison, Conservative interpolation between volume meshes by local Galerkin projection, Comput. Methods Appl. Mech. Eng. 200 (2011) 89-100.

[18] P. Farrell, M. Piggott, C. Pain, G. Gorman, C. Wilson, Conservative interpolation between unstructured meshes via supermesh construction, Comput. Methods Appl. Mech. Eng. 198 (2009) 26322642

[19] OpenFOAM v6 User Guide: 5.4 Mesh generation with snappyHexMesh

URL:

`https://cfd.direct/openfoam/user-guide/v6-snappyhexmesh/`

[20] OpenFOAM user Guide: pimpleFoam

URL:

`https://www.openfoam.com/documentation/guides/latest/doc/guide-applications-solvers-incompressible-pimpleFoam.html`

[21] S2A, Wind Tunnels: Souffleries aeroacoustiques automobiles

URL:

`https://www.soufflerie2a.com/en/moyens_soufflerie/soufflerie-echelle-11-561.html`

[22] OpenFOAM user Guide: SimpleFoam.

URL:

`https://openfoamwiki.net/index.php/SimpleFoam`

[23] A. Montorfano, F. Piscaglia, A. Onorati An Extension of the Dynamic Mesh Handling with Topological Changes for Les of ICE in OpenFOAM Paper presented at: SAE 2015 World Congress and Exhibition, Detroit, MI, USA, 21-23 April 2015, p. 1-15, 2015-01-0384 doi:10.4271/2015-01-0384

[24] SnappyHexMesh user Guide.

URL:

`https://openfoam.org/release/2-2-0/snappyhexmesh-features-layers-baffles/`

[25] "Computational Fluid Mechanics and Heat Transfer", McGraw-Hill, 1984, Anderson, Tannehill, Pletcher.

[26] Spalart-Allmaras Delayed Detached Eddy Simulation (DDES) in OpenFOAM:

URL:

`https://www.openfoam.com/documentation/guides/latest/doc/guide-turbulence-des-spalart-allmaras-ddes.html`

[27] Eymard, R. Gallouët, T. R., Herbin, R. (2000) The finite volume method Handbook of Numerical Analysis, Vol. VII, 2000, p. 713–1020. Editors: P.G. Ciarlet and J.L. Lions.

[28] The PIMPLE Algorithm - OpenFOAM:

URL:

`https://openfoamwiki.net/index.php/OpenFOAM_guide/The_PIMPLE_algorithm_in_OpenFOAM`

[29] Reiss, Jan & Haag, Lukas Indinger, Thomas.(2019). CFD investigation on fully detailed and deformed car tires. International Journal of Automotive Engineering. 10 324-331. 10.20485/jsaeijae.10.4-324

[30] Zhou, H., Jiang, Z., Wang, G. et al. Aerodynamic Characteristics of Isolated Loaded Tires with Different Tread Patterns: Experiment and Simulation. Chin. J. Mech. Eng. 34, 6 (2021). https://doi.org/10.1186/s10033-020-00528-1

[31] ANSA pre-processor - BETA CAE Systems
URL:
`https://www.beta-cae.com/ansa.htm`

[32] OMNIS/Hexpress — NUMECA International
URL:
`https://www.numeca.com/product/omnis-hexpress`

[33] Design Engineering — CATIA - Dassault
URL:
`https://www.3ds.com/products-services/catia/`